BIOMIMETIC SURFACE ENGINEERING FOR BIOFOULING CONTROL

ANDRÉ ECCEL VELLWOCK

PhD

The Hong Kong Polytechnic University

2022

The Hong Kong Polytechnic University

Department of Mechanical Engineering

Biomimetic Surface Engineering for Biofouling Control

André Eccel Vellwock

A thesis submitted in partial fulfillment of the requirements for the degree of

Doctor of Philosophy

July 2022

Certificate of originality

I hereby declare that this thesis is my own work and that, to the best of my knowledge and belief, it reproduces no material previously published or written, nor material that has been accepted for the award of any other degree or diploma, except where due acknowledgment has been made in the text.

_____ (Signed)

André Eccel Vellwock (Name of student)

Dedicated to my parents that were always by my side in this path

Dedicado aos meus pais, que sempre estiveram ao meu lado nesta trajetória

Abstract

Aquatic organisms naturally attach to surfaces to replicate and colonize. This is known as biofouling. It is essential for the ecosystem, but when it proliferates uncontrollably on a surface that needs to be absent of encrustations, it is a big problem. The naval industry, such as in boat hulls, controls biofouling through biocidal paints, which have been demonstrated not to be an environmentally friendly solution. Biofouling control through greener methods is a human need, and few ways have been suggested in the last decades. This thesis focuses on understanding the factors contributing to biofouling and developing environmentally friendly methods such as surface engineering.

Chapter 01 consists of an introduction to the field, such as current biofouling techniques, manufacturing methods for fabrication of biomimetic surfaces, methodologies to assess fouling, literature's proposed fouling theories, and so on.

In Chapter 2, a meta-analysis was performed to understand the factors that affect the adhesion of organisms. Considering ten factors such as fouler species, water flow rate, and surface morphology, a data-driven approach was proposed and validated experimentally, showing a practical method for predicting the adhesion efficiency of fouling organisms. The outcome greatly facilitates the design of antifouling surfaces and materials.

Many environmental-friendly solutions (i.e., surface topography alteration and coating) against fouling modify the base material's optical properties. In Chapter 3, a surface with nanowrinkles, inspired by the zebrafish (*D. rerio*) corneal surface, is fabricated. By varying the nanowrinkle's dimensions and through experimental and numerical

analyses, the influence of wrinkles on the material's transparency is explored. Moreover, their antifouling performance is evaluated through bacterial assays and field tests, highlighting an optimal dimension of the nanowrinkles. This work provided a direct approach to reconciling antifouling performance and optical properties on wrinkled surfaces.

The influence of the surface morphology and properties on the adhesion of foulers is a topic of constant debate. Research shows that a well-designed surface can reduce fouling drastically compared to a flat counterpart. To be effective, the surface features have to the sized similar to the fouling organisms such as marine bacteria, sized around one micrometer, and barnacles, sized around hundreds of micrometers. Antifouling is based on reducing the fouler contact force to the substrate. Fabrication methods to obtain large surfaces with micrometer-sized features are extremely costly, have complex processes, and are often made of fragile materials. Chapter 4 describes a facile fabrication method to obtain metallic-based, large-scaled surfaces covered by micrometer-sized controllable features. It is based on adding a metallic mesh onto a substrate and coating it with paint. The addition of natural antifoulant products to the paint composition is discussed. The best mesh dimension is proposed after field and laboratory biofouling analysis.

Through this thesis, several topics related to biofouling were studied. These results are of significant value to designing and fabricating antifouling surfaces and understanding of factors influencing organisms' attachment.

Publications arising from the thesis

A.E. Vellwock, P. Su, Z. Zhang, D. Feng, H. Yao, 2022. Reconciling the conflict between optical transparency and fouling resistance with a nanowrinkled surface inspired by zebrafish's cornea, ACS Applied Materials & Interfaces 14(6), 7671-7625.

A.E. Vellwock, H. Yao, 2021. Biomimetic and bioinspired surface topographies as a green strategy for combating biofouling: A review, Bioinspiration & Biomimetics 16, 0411003.

A.E. Vellwock, J. Fu, Y. Meng, V. Thiyagarajan, H. Yao, 2019. A data-driven approach to predicting the attachment density of biofouling organisms, Biofouling 35(8), 832-839.

A.E. Vellwock, Z. Zhang, P. Su, Y. Gao, Y. Meng, V. Thiyagarajan, D. Feng, H. Yao. Towards large-scaled cost-effective metallic antifouling solutions for the naval industry. In preparation.

H. Yao, **A.E. Vellwock**. Anti-biofouling film, preparation method and use thereof. Chinese Patent. Filed in June, 2021.

Conference presentation

A.E. Vellwock. A data-driven approach to predicting the attachment density of biofouling organisms. Machine Learning in Science and Engineering, 2020 (Virtual).

Acknowledgments

The last years were full of great and not-so-great moments, but the meaningful memories will be remembered forever. Dozens of people who have been involved and were essential to this project completion should be acknowledged.

I would like to deeply thank Dr. Haimin YAO, my chief supervisor, for his patience, guidance, insightful opinions and advices during this doctoral period. Our frequent and routine talks and discussions were invaluable for keeping my research on track. His personality provided me a paradigm for guiding my research work and enlightened the path of my research journey ahead. I am grateful and cherish the time spent in these years under his supervision.

Meanwhile, I would like to express my gratitude to my parents' lifelong support. Roberto Vellwock Neto and Sandra Eccel are the people that have forever and always been by my side, supporting me emotionally and financially through my educational years. Despite knowing that my choice to follow an international academic career creates a physical separation between us, their everlasting approval is a blessing. Brazil is on the other side of the globe, far from Hong Kong. However, our constant online talks are filled with joy and advice. This thesis is also theirs.

It has been an unforgettable experience to collaborate with my groupmates Dr. Yang GAO, Dr. Zhenbin GUO, Dr. Juntan YANG, Mr. Anran WEI, Dr. Ji LIN, Mr. Zijing ZHANG, Ms. Yujie XIE, Dr. Jimin FU, Ms. Sally XUAN, Mr. Like JIANG, Mr. Peng OUYANG, and Dr. Xuchao WANG. Moreover, the collaborations with Dr. Yuan MENG, Dr. Vengatesen THIYAGARAJAN, Dr. Pei SU, and Prof. Danqing FENG were important to our biofouling tests.

I am thankful for the support from the Hong Kong Wetland Park for providing mangrove leaves and the Hebe Haven Yacht Club for allowing us to perform the field tests.

I also thank the administrative staff in the Department of Mechanical Engineering of the Hong Kong Polytechnic University (PolyU), particularly Ms. Lily TAM and Mrs. Michelle LAI, and the technical staff, particularly Dr. Terence WONG, Dr. Hardy LUI, Ms. Pendy HO, and Ms. Wing Man HO.

Special thanks to my wife, Gao Shu, a person that shines happiness and is never afraid to tackle any obstacle. Your perseverance, love, and lots of patience pushed me forward during these years. Thank you so much. Moreover, thanks also go to my parents-in-law for all the support since they discovered we would be living in Hong Kong.

I acknowledge the financial support from the Research Grants Council of Hong Kong Special Administration Region and the Hong Kong Polytechnic University.

Lastly, I would like to thank all the people who have helped me with this thesis.

Table of contents

List of figures

List of tables

Chapter 1 Introduction

1.1 Biofouling

Biofouling refers to the attachment and growth of unwanted organisms on surfaces. Its existence increases the necessity of maintaining and cleaning submerged surfaces, such as boat hulls, floating buoys, and underwater cables. Moreover, the extra surface roughness raises the hull drag force, thus the expenses with fuel [1]. It is estimated that biofouling causes an additional cost of 1-6 million US dollars per year per mid-sized ship, and the yearly impact in the US Navy alone is between 180-540 million US dollars [2]. Considering that the US Navy fleet amounts to less than 0.5% of the world's commercial ships, the world's yearly expenses due to fouling are in the billions of US dollars range.

As a progressive process consisting of multiple steps, biofouling of a clean solid surface immersed in a fouling environment (e.g., ocean) starts from the adsorption of the dissolved organic matters such as proteins, carbohydrates, glycoproteins, and other macromolecules, resulting in a conditioning film (Figure 1.1a). The formation of the film, especially the sorption of protein, strongly depends on the environment's pH and ionic strength [3, 4]. Then, bacteria present in the environment attempt to attach to the surface. At that moment, two forces dominate the interaction between the bacteria and substrate. Van der Waals force attracts the bacteria towards the surface, while the electrostatic double-layer interaction is repulsing. Both forces depend on the surface physicochemical properties of the bacteria and substrate [5, 6]. Their net force varies with the separation between the bacteria and the substrate and is often modeled by the colloidal Derjaguin–Landau–Verwey–Overbeek (DVLO) theory (Figure 1.2) [5]. At

this moment, the bacteria/substrate adhesion is weak and remains reversible if an external disturbance is available (Figure 1.1b). It becomes irreversible after the bacteria release lipopolysaccharides (LPS) molecules that anchor the bacteria firmly to the substrate surface (Figure 1.1c). This biological event happens a few seconds after the immersion. Upon the anchorage, the bacteria start to self-divide and proliferate, causing rapid growth and colony formation. They begin to secrete extracellular polymeric substances (EPS) on top of the LPS, ensuring the bacteria colony's adhesion to the surface and internal cohesion (Figure 1.1d). This step is completed a few minutes after the immersion. EPS, per se, is composed of simple homo- and heteropolysaccharides [7]. Due to its sorption properties, it confines colloidal nutrients previously present in the medium, promoting biofilm growth to a greater extent [8]. For biofouling in biomedical settings, the attachment process ceases after biofilm formation. For marine biofouling, the formed biofilm alters the surface's characteristics and provides a basis for the subsequent secondary colonization by the fouling organisms (e.g., diatoms, algae spores, and larvae of invertebrates) (Figure 1.1e). This step typically happens a few days after the immersion. Consequently, the attachment of the microfoulers creates an environment that aids the settlements and aggregation of the macroscopic foulers (e.g., oysters, barnacles, seaweed, tubeworms), leading to the thriving of the local ecosystem (Figure 1.1f). This step typically happens a few weeks to months after the immersion.

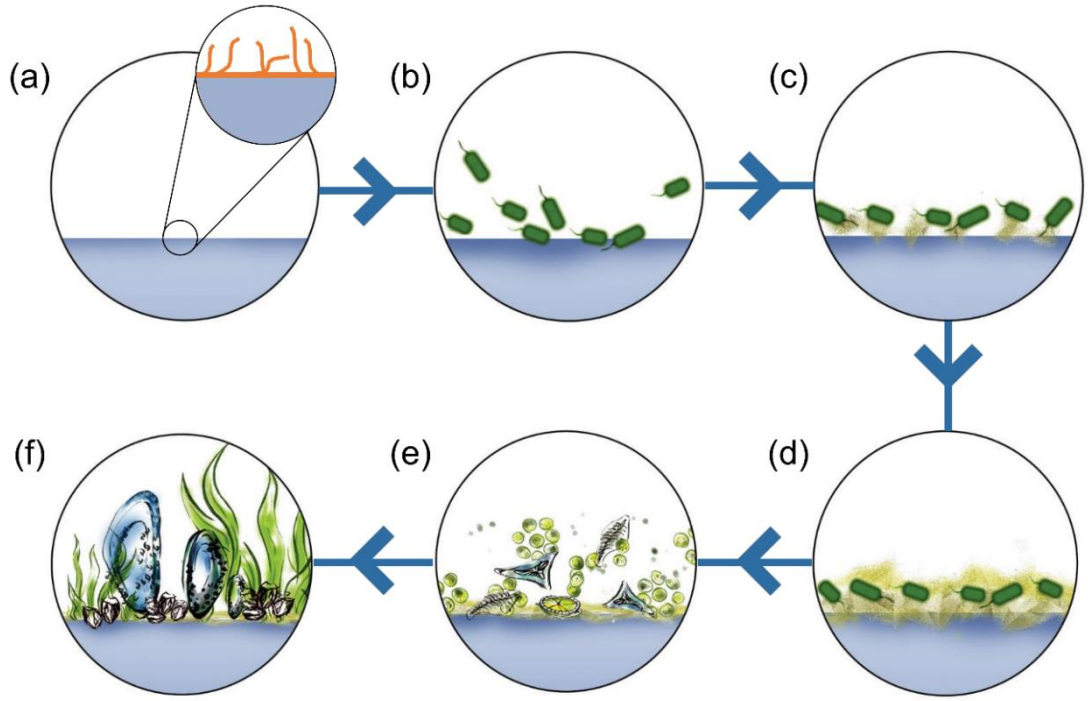

Figure 1.1 Schematic illustration of the biofouling process starting from forming a conditioning film to the macrofoulers' attachment, growth, and aggregation. (a) The surface is submerged, and a conditioning film is formed. (b) Bacteria attempt the surface. (c) The release of LPS enables the irreversible settlement of bacteria on the substrate. (d) Biofilm forms and grows. (e) Settlement of microfoulers (e.g., diatoms, algae spores) and (f) macrofoulers (e.g., oysters, barnacles, seaweed, tubeworms). Time frames: (a, b, c) seconds, (d) minutes, (e) days, (f) weeks to months.

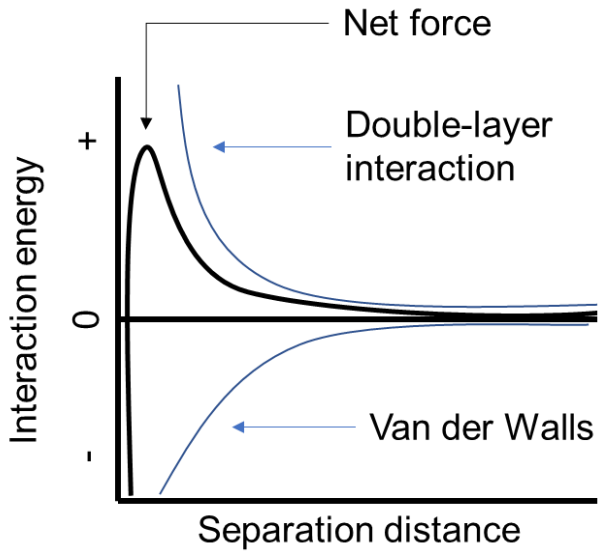

Figure 1.2. Schematic for the DVLO theory and the influence of the separation distance to the bacteria/substrate distance [5].

A developed biofouling colony, like the ones located on the ship hulls, contains multiple fouling species, including seaweed, barnacles, tubeworms, and so on. Figure 1.3 illustrates some typical fouling species. Ulvaceae is a common family of seaweeds. Their settlement occurs during their microscopic zoospore form, allowing them to thrive on a macroscopic scale (Figure 1.3a). Barnacles have a complex metamorphosis cycle. Figure 1.3b shows nauplii, one stage before the cyprid form that later attempts to adhere to substrates. After development, adult barnacles release a biological glue to achieve strong attachment with the substrates and then develop calcareous shells. Tubeworm is another fouler commonly present in the ocean. Its reproduction starts with the fecundation of eggs, followed by the development of larvae. After their attachment to the substrates, the adult animals become tube-shelled worms (Figure 1.3c).

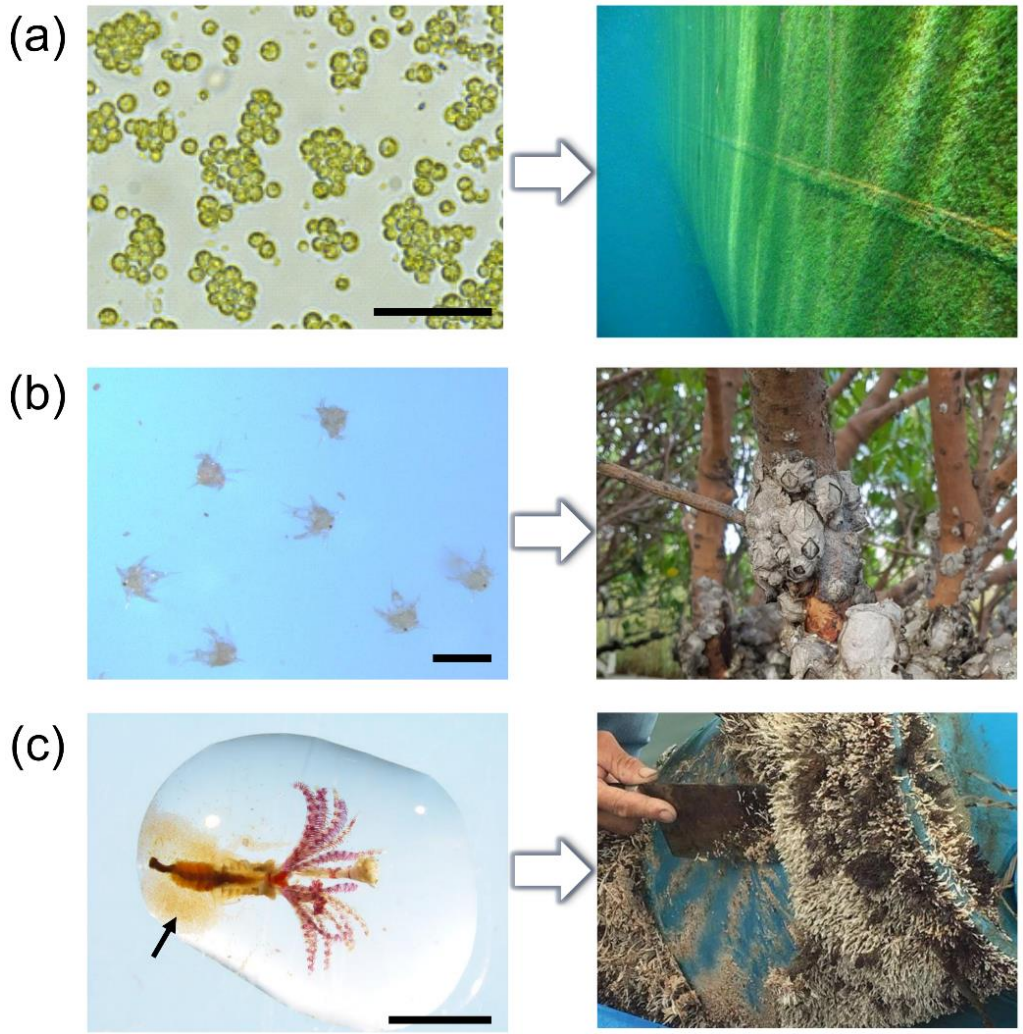

Figure 1.3. Typical biofouling organisms: (a) green algae zoospores and mature colony, (b) barnacles nauplii and developed organisms attached to a mangrove tree trunk, (c) a tubeworm egg and adults. Scale bars: (a) 50 µm, (b) 300 µm, (c) 500 µm.

1.2 Conventional techniques for biofouling control

Traditionally, chemical biocides were widely applied as the standard approach to controlling marine biofouling (Figure 1.4). Compounds such as tributyltin oxide ($C_{24}H_{54}OSn_2$) and tributyltin fluoride ($C_{12}H_{27}FSn$) are mixed with polymeric binders and applied to the hull of ships. However, through years of study, researchers found that tributyltin (TBT) is harmful to aquatic ecosystems across the globe, from the artisanal fisheries in Fiji [9], European coastline [10, 11], Chinese waterways [12], to

the isolated waters in Antarctica [13]. The impairments include physical alterations in living animals such as mollusks [14, 15] and fishes [16, 17]. In 1998, the use of TBT in antifouling paints was banned by the International Maritime Organization, prompting the need to develop non-toxic anti-fouling techniques [18].

Figure 1.4. Application of antifouling paint to a boat hull.

To develop green alternates of the toxic biocides, researchers first focused on the antifoulants present in natural materials [19]. The extracts from the mangrove species (*Excoecaria agallocha*, *Kandelia obovata*, *Sonneratia apetala*, *Avicennia marina*, *Bruguiera gymnorhiza*) were found to possess anti-fouling capability against marine bacteria, microalgae, mussel *Perna indica*, and barnacles *Balanus Amphitrite* and *Balanus albicostatus* [20, 21]. Moreover, these natural compounds could fully degrade within months, implying their non-toxic characteristics [20]. A formulation of the extractions from the sponge *Haliclona caerulea* and algae *Sargassum horridum* can reduce 32% fouling compared to the control during *in vitro* and field tests [22]. Commercial paints containing active compounds extracted from the bacteria strains of the seaweed *Fucus serratus* and the nudibranch *Archidoris pseudoargus* showed enhanced performance in reducing the growth of marine bacteria [23].

Besides, non-chemical anti-fouling techniques have been developed as well. For example, applying an electrical potential to the ship hull reduced marine bacteria adhesion [24]. The same method was shown to create gas bubbles on the hull surface, preventing biofilm formation and suppressing fouling organisms' settlement [25, 26]. However, this method is not scalable as it demands a large amount of energy and intensifies the corrosion of the ship hull due to the electrolysis effect [27]. An alternative approach was to apply dynamic vibration to detach the attached organisms [28, 29]. This method also suffers from a deficiency of extensive power consumption, especially for commercial ship hulls with gigantic fouled surfaces [27].

To learn the non-chemical anti-fouling techniques from nature, recent studies have focused on the delicate topographies of a variety of naturally occurring surfaces and the development of their replicates in either biomimetic (BM) or bioinspired (BI) way. A biomimetic replica copies exactly the natural material's characteristics, while a bioinspired replica only follows the characteristic features of the paradigm. The development of BM/BI antifouling surfaces relies on diverse manufacturing techniques, which are elaborated on in the next session.

1.3 Manufacturing methods for BM/BI surfaces

The antifouling surface topographies contain features at the micro- to nanoscales, which are beyond the scope of the traditional manufacturing approaches such as machining and milling. The duplication of the naturally occurring topographies relies on appropriate indirect manufacturing processes that can be divided into four categories based on their underlying principles: molding, lithography, surface

corrugation, and chemical etching (Figure 1.5).

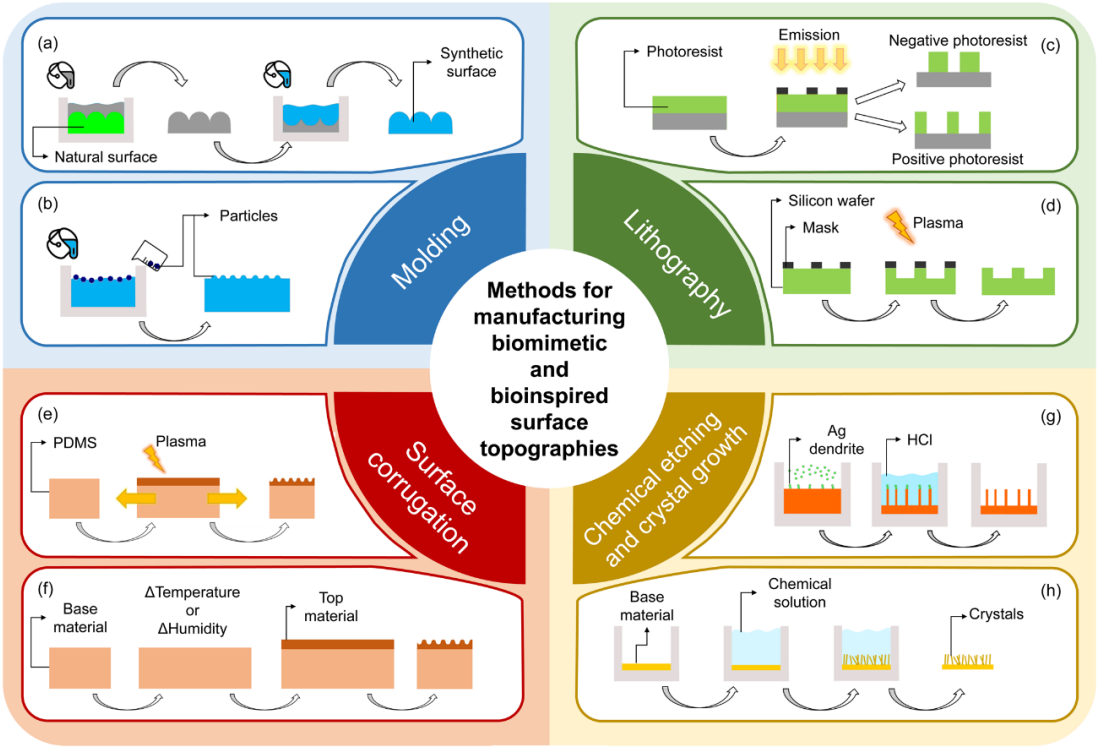

Figure 1.5. Methods for manufacturing BM/BI surface topographies can be divided into four categories: molding (a & b), lithography (c & d), surface corrugation (e & f), and chemical etching and crystal growth (g & h). (a) A two-step molding process to duplicate the topography of a naturally-occurring surface; (b) A molding process with nano- and micro-particles to produce BI nano and micro surface topographies; (c) photolithography and (d) plasma lithography processes to produce BI surface structures; surface corrugation of bi-materials caused by (e) mechanical pre-strain or (f) temperature/humidity-induced strain misfit to produce wrinkled surfaces; (g) metal-assisted chemical etching and (h) crystal growth to produce nanostructures on surfaces.

1.3.1 Molding

Molding is the most prevalent method to fabricate biomimetic surfaces, whose basic steps are illustrated in Figure 1.5a. To ensure precise duplication of the delicate surface topography in nature, the natural topography should be cleaned thoroughly with a buffer solution (e.g., phosphate-buffered saline or cacodylate buffer), distilled water, or acetone. Subsequently, the surface may be fixed with glutaraldehyde or

formaldehyde. After drying in the air, the surfaces are ready for use. If the material has high water content, freeze-drying [30], critical point drying [31], or submerging on ethanol series [32] should be applied to remove water molecules extensively. This process might alter the topography, and examination of the surface through imaging technologies (e.g., scanning electron microscopy, atomic force microscopy) is needed. Next, a selected polymeric resin is cast onto the natural surface for duplication. The commonly used polymeric resins include polydimethylsiloxane (PDMS) [33], epoxy resin [34, 35], and polymethyl methacrylate (PMMA) dissolved in acetone. After demolding the cured resin, a negative mold is acquired. Then, the second molding process is carried out using the obtained negative mold as the template. For easy demolding, ultrasonication or deposition of molecules on the surface of the negative mold (e.g., deposition of trichlorosilane) might be applied. After demolding the cured resin, the final biomimetic surface is obtained. The molding method is operationally facile but fails to duplicate topographical features less than 1 μm [35]. This deficiency can be attributed to the unavoidable air bubbles in the viscous polymeric molding materials even though the degassing process is applied. Maintaining the integrity of the fragile and tiny structural features (e.g., nanopillars) during the demolding process is another challenge of the molding method.

Molding can also be a direct manufacturing technique to fabricate BI topographies. For instance, Clasen and Kesel (2019) embedded microparticles (i.e., microspheres) into a base material [36]. After solidification, a surface with sparse micro-domes or partially exposed microparticles is created (Figure 1.5b). The size of the particles determines the spatial resolution of this method. If nanoparticles are applied, nanoscaled topographies can be obtained [37, 38]. This method suffers from two

deficiencies. The available particle geometries are limited, including spheres, rods, stars, and prisms. The positioning and orientation of the particles are uncontrollable.

1.3.2 Lithography-based methods

Photolithography was initially developed in the micro-electromechanical field [39]. It applies light, such as ultraviolet light or laser, combined with a photomask to create micro and nanopatterns on photoresist films (Figure 1.5c). There are two types of photoresists: positive and negative. A positive photoresist becomes soluble to the photoresist developer if exposed to light and the unexposed portion remains insoluble to the photoresist developer. In contrast, a negative photoresist turns insoluble to the photoresist developer when exposed to light, and the unexposed portion remains soluble. Photolithography was reported to achieve features as small as 170 nm [40]. Nevertheless, the high cost is the primary limitation of this method, mainly because of the expensive photomasks and equipment. To reduce the cost, maskless photolithography technology has been developed [41], in which the focus of the light beam is directed in a controllable way to expose a portion of the photoresist in a prescribed geometry. Different mechanisms have been applied to direct the light beam. For example, zone-plate array lithography introduces an array of diffractive lenses with controlled light intensity, while scanning-electron beam lithography creates the pattern design using a beam deflection system [42]. No photoresist is required for meshless photolithography. Features less than 100 nm can be achieved but highly depend on the setup [43]. Like the photolithography process, reactive-ion (plasma) lithography (Figure 1.5d), in combination with a patterned mask, was also applied to

fabricate bioinspired micro and nanostructures [44].

1.3.3 Surface corrugation

The manufacturing methods described above suffer from a common deficiency. They cannot be scaled up to fabricate a sizeable antifouling surface, which significantly limits their application in practice. The fabrication of surfaces with controllable wrinkles has been proposed to solve this issue [45-48]. A generic fabrication route is shown in Figure 3e. First, a polymeric material, often PDMS film, is pre-stretched and then subjected to irradiation such as oxygen plasma or UV light. Such treatment transforms the topmost layer of PDMS into a silica-like material with higher stiffness [49]. When released from the pre-strain, the newly formed bilayer structure generates a wrinkled surface due to the mechanical instability of the stiffer top layer under compression. The feature dimensions of the resulting wrinkles such as wavelength and amplitude depend on the irradiation time and power, and pre-strain level. In addition to releasing the pre-strain, the compression applied on the stiffer top layer can be achieved alternatively by variation of temperature [50], humidity [51, 52], or chemical reaction [53] (Figure 1.5f).

1.3.4 Chemical etching and crystal growth

Chemical etching and crystal growth are often applied to fabricate BI surface topographies, especially those at the nanoscale. For example, nano-spikes with a high aspect ratio were manufactured with the metal-assisted chemical etching method Figure 1.5g) [54]. First, silver dendrites are grown on a silicon wafer. Then, the silicon

wafer is submerged in hydrochloric acid for etching. Due to the protection of the discrete nanosized silver dendrites, etching of the silicon happens only in the areas without dendrites, resulting in nano-spikes with a height determined by the etching time. Finally, the protective silver dendrites are removed from the top of the silicon nano-spikes by ammonium hydroxide and hydrogen peroxide.

Antifouling nanostructures have also been fabricated by crystal growth (Figure 1.5h). For example, $NiCo_2O_4$ nanoflakes on graphite paper have been grown and demonstrated high resistance to tubeworm larvae settlement [55]. By altering the synthesis's additives, this method can be used to fabricate $NiCo_2O_4$ nanorods and even hierarchical nanostructures [56]. Extension of this method to the other conductive substrates has also been demonstrated feasible [57].

Recently, additive manufacturing has been thriving quickly for its capability to produce structures with intricate topographies and features as small as sub-micron scale [58, 59]. However, the cost of this technology remains high, especially for producing a surface with designed topographies at a micrometer scale or even smaller. It is, therefore, not a practical approach for the mass production of antifouling surfaces [60].

1.4 Biofouling assessment methods

The antifouling performance of the BM and BI surface topographies is usually evaluated by settlement bioassay, aiming to examine the fouling extent by the selected fouler(s). Settlement bioassay can be performed in the laboratory or the field, depending on the objectives of the test. The laboratory test procedure starts by

submerging the test surfaces into filtered seawater containing a certain amount of living foulers. Typically, a single fouler species is applied to avoid possible inter-species interference [61]. The primary advantage of laboratory tests is the controllability of the experimental variables, such as temperature, light irradiation, and so on. Field tests are generally carried out near piers or seashores, which allow an on-site observation of how the biofoulers in the local ecosystem interact with the tested surfaces. Moreover, the interaction between multiple species can be examined in the field tests, which is an essential advantage over the laboratory counterparts [61, 62]. However, it cannot be used to evaluate the effects of experimental variables because the weather and the local environment are uncontrollable, making it difficult to compare the results from different researchers quantitatively. An ideal assessment of a surface's antifouling performance should include laboratory and field tests [62]. While laboratory tests are performed to assess antifouling performance against individual biofoulers, the field tests are carried out to confirm the antifouling performance under a more complex and realistic environment.

The quantitative assessment of the fouling extent of a surface after the test relies on a variety of microscopy technologies. As marine bacteria range from hundreds of nanometers to a few micrometers [63], optical microscopes may have difficulties visualizing some microorganisms [64]. For a higher spatial resolution, fluorescent microscopy can be applied [65]. A prior sample staining is required if the microorganisms do not have a chlorophyll-based natural fluorescence [66]. Quantification of the fouling extent can be done in two ways. The most straightforward but more time-consuming way is to count the bacteria density. Software such as *ImageJ* [67] can be applied to enhance efficiency. In this sense, fluorescent microscopy

is more appropriate as it offers high contrast of color between the bacteria and the substrate. If there is a need to observe specific features of the foulers/substrate interaction, Scanning Electron Microscopy (SEM) can be applied as it can achieve a resolution as high as a few nanometers [68].

For biofilm, counting the number of individual microbes is extremely difficult and time-consuming [69]. Indirect methods to quantify the amount of biofilm are applied. The standard approach is to place the tested surface with attached biofilm in a container with filtered sterile seawater and then sonicate it to have the biofilm detached from the substrate and dissolved into the seawater. By measuring the optical properties (e.g., transmittance) of the liquid containing the dissolved biomass, the biofilm amount can be determined quantitatively as the reduction of light transmitted through the liquid correlates well with the amount of biofilm [70]. Alternatively, the fouling extent can also be assessed by measuring the pH of the solution as some bacteria produce acids while proliferating; therefore, lower pH implies higher bacterial fouling [71]. This method is cost-effective but cannot be used to investigate the position and distribution of foulers on the surface, which is essential for designing a structured surface to prevent biofouling. A more precise assessment of biofouling can be achieved by using quartz crystal microbalance (QCM) [72-75], which measures the shift of the resonant frequency of an oscillating quartz sensor caused by the attached foulants. The fouling density is determined through the Sauerbrey relation [76] and the extended Voigt-Kelvin viscoelastic model [77]. This approach features high resolution (ng/cm^2) and real-time and has been applied to foulants, including bacteria [72, 73], diatoms [74, 75, 78], and algae [74, 79].

Macrofoulers, in their initial larval stage, vary in dimension from tenths to hundreds

of micrometers, which makes it possible to apply optical microscopy to quantify the areal density of the foulers attached to the tested surfaces. However, when multiple species of foulers attach to a surface simultaneously in a field test, the quantification must be rethought. One solution is photographing a partially fouled surface and employing image processing techniques to assess the fouling coverage fraction. Another approach is to examine the weight variation of the sample before and after the settlement assay and use it to signify the fouling extent. However, these two methods sometimes will give contradictory results. For example, surface A has extensive coverage of microfoulers, but macrofoulers are absent. In contrast, surface B does not have any visible microfoulers but is covered with a few large barnacles. Assessment based on weight variation shows that surface A performs better in preventing biofouling since macro biofoulers tend to be heavier. However, if the areal fouling coverage is adopted as the measurement of antifouling performance, surface B performs better. It is suggested to adopt the weight variation method only if all the samples have 100% biofouling coverage.

After the settlement assay, the antifouling performances of various structured surfaces, including the smooth control one, are compared. Statistical significance tests are usually conducted to verify whether the available difference is not likely to occur by chance but is attributed to a specific cause. The significance of the difference is measured as $1 - p$, where p refers to the probability of having no difference. If $p < 0.05$, the significance is $> 95\%$, implying that the associated topography has $> 95\%$ probability of having a difference in antifouling performance.

1.5 Natural antifouling surfaces and their synthetic replicas

To learn non-chemical anti-fouling strategies from nature, researchers have explored the surface topographies of a variety of marine organisms, including seaweeds [33, 34], mangrove leaves [55], seeds [36], mussels [35, 80, 81], shark skin [82] and egg case [35], crabs [35, 83], and brittle stars [35], and so on. These studies not only revealed the diverse surface topographies in nature with antifouling functionality but also synthesized biomimetic or bioinspired (BM/BI) replicas with comparable antifouling efficacy. In the following, these naturally occurring surface topographies and their BM/BI duplications are introduced. According to their origins of inspiration, these synthetic surface topographies are classified into two groups: plant-originated and animal-originated.

1.5.1 Plant-originated antifouling surface topographies

Mangroves are trees living in the intertidal zone. They are particularly inspiring for antifouling studies because of their fouling-free leaves despite being frequently submerged in seawater. The leaves of the mangrove *Sonneratia apetala* exhibit a ridge-like surface topography with a height of 5 μm and an inter-ridge spacing of 5 μm (Figure 1.6a). These microscopic ridges exhibit no preferential alignment and orientation. A PDMS replica of the mangrove leave (Figure 1.6b) showed much higher resistance against the attachment of tubeworm *Hydroides elegans* than a smooth PDMS surface without any topography [55].

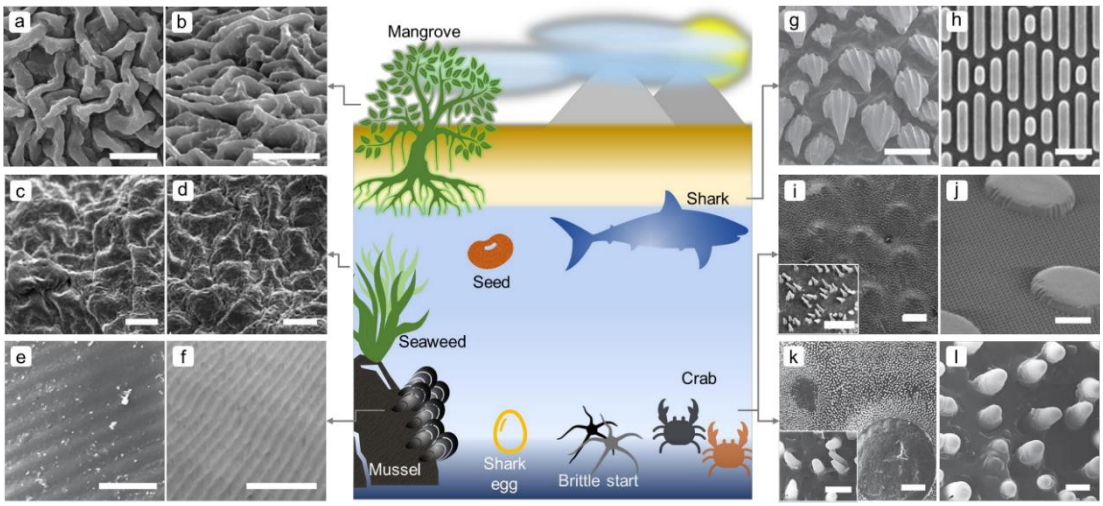

Figure 1.6. Typical marine organisms with textured surfaces capable of preventing biofouling. (a, c, e, g, I, k) are the natural surfaces and (b, d, f, h, j, l) are the corresponding synthetic replicas. (a, b) mangrove leaves, (c, d) seaweeds, (e, f) mussels, (g, h) shark skin, (I, j) crab *M. hardwickii*, (k, l) crab *C. pagurus*. Scale bars: (g, i) 500 µm, (j) 50 µm, (a, b, c, d, h, k, inset of i) 10 µm, (e, f, l, inset of k) 5 µm.

Seaweeds are multicellular algae that can grow to meters long. Their "leaves" called blades are mostly free of biofouling, implying the existence of possible antifouling topographies. Species of *Saccharina latissima* (Sugar kelp), *Fucus guiryi* (Guiry's wrack), and *Laminaria japonica* have been studied [33, 34]. It was found that the surface of *S. latissima* blades exhibits irregularly distributed ridges with a mean feature-length of 9.9 µm (Figure 1.6c), while *F. guiryi* possesses spicules with a length of 3.3 µm. The molded polymeric replicas of *S. latissima* and *F. guiryi* showed a decrease in biofilm growth compared to a flat control in a 7-day field test [33]. *L. japonica* has a surface covered by dimples with a low aspect ratio (height/diameter). Its PDMS replica made by a sequential molding method showed the capability of reducing the fouling of diatoms (*Nitzschia closterium*).

Drifting seeds are plant seeds that spread by taking advantage of ocean currents. Field tests were carried out to study the antifouling performance of the drifting seeds of 43

species originating from different locations of the world. Despite the prevalence of barnacles at the test location, after 12 weeks, 6 out of 43 studied seeds' species were found free of barnacle fouling [36]. Four (*Erythrina berteroana*, *Ipomoea alba*, *Sapindus Saponaria*, *Coccothrinax borhidiana*) exhibit surface microstructures with irregular features smaller than 5 μm in size. Two (*Acoelorrhaphe wrightii* and *Licuala spinosa*) present regular honeycomb structures (width of 15.2-19.0 μm, and length of 21.7-28.0 μm). All these six antifouling surfaces have a mean roughness (R_a) from 0.36 μm to 2.09 μm. Inspired by these results, BI surfaces made of silicon impregnated with hollow nanoparticles were fabricated. After a 12-week field test, the BI surfaces exhibited relative ease of cleaning, implying lower adhesion between the attached barnacles and the substrate [36].

1.5.2 Animal-originated antifouling topographies

Mussels play a dual role in the biofouling game: they are foulers but also subjected to fouling by other smaller species such as barnacles. Biomimetic surfaces made from the shells of the blue mussel *Mytilus edulis* (Figure 1.6e) showed a capacity to prevent the attachment of the barnacle *Balanus improvisus* for a short term during a field test [35]. A polyimide surface inspired by the shell of the mussels *Mytilus galloprovincialis* (Figure 1.6f) presented less fouling during a test involving two diatom species (*Amphora sp*. and *Navicula jeffreyi*). A study considering mussels from different countries showed that the BM surfaces of mussels *Perna perna* (Brazil) and *M. edulis* (UK) were able to reduce the attachment of larval barnacle *Semibalanus balanoides* in a field test [81].

Among all the naturally occurring surfaces with antifouling potential, shark skin may be the most popular one that has attracted intensive studies on it. Inspired by the shark skin, a commercial antifouling surface, also called Sharklet, was developed [82]. Its architected surface with platelet patterns made of PDMS through photolithography was found to reduce the settlement of zoospores by 86% as compared to a smooth counterpart (Figure 1.6h). Furthermore, different regions on the *Scyliorhinus canicula* (small-spotted catshark) skin showed distinct resistance to biofouling [84]. BM molded replicas showed that the caudal and second dorsal regions exhibit a slightly better antifouling capability during a two-week-long field test, with around 4% less adhered foulant mass than that on the shark head BM surface. In addition to the shark skin, the surface of the eggshell of shark *S. canicula* was also studied and showed temporary anti-fouling competence [35].

Crabs are animals inhabiting most of the time underwater, and they have evolved multiple strategies to reduce the attachment of biofoulers, including grooming [85], sand burying, and molting [86]. More interestingly, the carapaces of the two species were found to have surface structures at multiple scales. For example, the carapace of *Myomenippe hardwickii* (Mangrove stone crab) is covered with flat short circular tubercles (5 μm high and 25-170 μm in diameter) surrounded by microscopic spines (0.6-1.2 μm in diameter, 3-13 μm long) (Figure 1.6i). Its bioinspired replica (Figure 1.6j) was reported to reduce the fouling of the diatom *Amphora sp* and the barnacle *Balanus amphitrite* [83]. Similarly, Brown crab *Cancer pagurus* show elevated cylinders with 200 μm in diameter surrounded by spines (2-2.5 μm in length) (Figure 1.6k). A biomimetic surface of the Brown crab (Figure 1.6l) showed statistically significant resistance to the settlement by the mussel *M. edulis* [35]. In another study,

a porous surface inspired by the carapace of Brown crab decreased diatoms attachment [87]. Brittle stars inhabit the sea floors. One of its species (*Ophiura texturata*) possesses a surface covered by micro projections of 10 μm in diameter. Their biomimetic replica was demonstrated to reduce the attachment of the ciliate *Zoothamnium commune*, the mussel *M. edulis*, and the barnacle *B. improvisus* [35].

1.6 Feature sizes of the antifouling topographies versus the sizes of the prevented foulers

Ashby plot is a type of graphical representation initially developed to visualize the ranges of selected material properties (e.g., modulus, toughness) of different material categories (e.g., metals, polymers, ceramics) to facilitate material selection. To visualize the dimension range of the antifouling topographies compared to that of the prevented biofoulers, here we develop Ashby plot-like diagrams per the reported data as summarized in Figure 1.7a. Figure 1.7b and Figure 1.7c plot the feature spacing (λ) and feature height (h) of the effective BM/BI anti-fouling topographies versus the dimension (ϕ) of the corresponding prevented biofoulers, including barnacles, mussels, tubeworms, ciliates, *Ulva* spores, and diatoms. From Figure 1.7b and Figure 1.7c, it can be seen that most results are located above the lines defined by ϕ/λ=1 and ϕ/h=1, implying that excellent antifouling performance is expected when the feature dimensions of the topographies (spacing and height) are less than the dimension of the biofoulers.

(a)

Index	Species		Topography (BI/BM)	Diatoms d1	d2	d3	d4	d5	Seaweed s	Ciliates c1	c2	Tubeworm t	Polychaete p	Mussel m	Barnacles b1	b2	b3	Source
A	Mussels	mu1	Parallel ridges (BI)	0	X	0	0											Scardino *et al* (2005)
B				0	X	✓	✓											
C		mu2	Projections (BI)	0	0	0	0											
D		mu3	Parallel ridges (BM)							0	0		0	0	✓			Bers *et al* (2004)
E		mu4															✓	Bers *et al* (2006)
F		mu5															0	
G		mu6															✓	
H		mu7															0	
I	Seaweeds	sw	Projections (BI)					✓										Zhao *et al* (2020)
J	Mangrove	ma	Random ridges (BM)									✓						Fu *et al* (2018)
K	Seeds	sd	Projections (BI)												✓	✓		Ciasen and Kesel (2019)
L															✓	✓		
M	Shark	sh1	Parallel ridges non-uniform (BI)						✓									Carman *et al* (2006)
N		sh2	Parallel ridges (BM)							0	0		0	X	0			Bers *et al* (2004)
O	Brittle star	bs	Projections (BM)							✓	0		0	✓	✓			Bers *et al* (2004)
P	Crabs	cr1	Projections (BI)				✓									✓		Brzozowska *et al* (2014)
Q							✓									✓		
R		cr2	Projections (BM)							X	0		0	✓				Bers *et al* (2004)
S										X	0		0	✓				

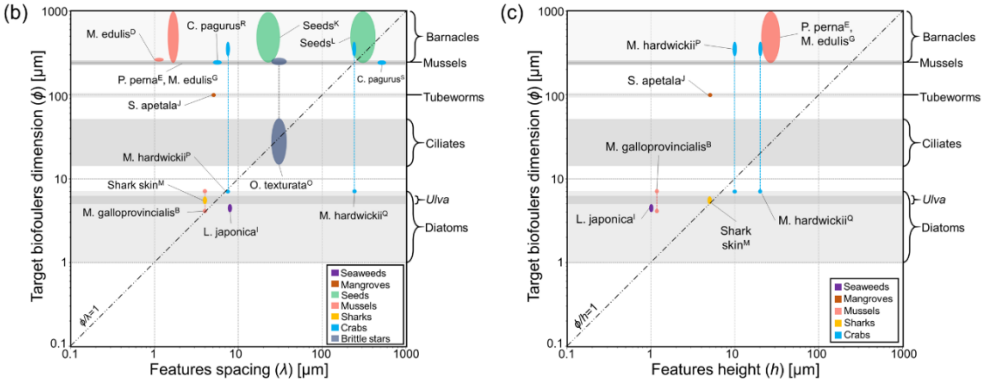

Figure 1.7. (a) Effects of the synthetic surface topographies, either bioinspired (BI) or biomimetic (BM), originated from different marine organisms on the settlements of varying tested biofoulers. Topographies proved to resist the settlement of the tested foulers are denoted by the symbol "✓"; topographies proved to facilitate the settlement of the tested fouler are denoted by the symbol "X"; topographies showing no apparent effect on the settlement of the tested fouler are denoted by the symbol "0". Here, the thresholds for determining the resisting or facilitating effects are selected as +20% or −20% variations in the fouling density after seven days. Biofoulers are divided into categories. Diatoms: d1-*F.carpentarie*, d2-*N. paleacea*, d3-*N. jeffreyi*, d4-*Amphora sp*, d5-*N. closterium*. Seaweed: s-*Ulva sp*. Ciliates: c1-*Z. commune*, c2-*Vorticella sp*. Tubeworms: t-*H. elegans*. Polychaetes: p-*Polydora sp*. Mussels: m-M. edulis. Barnacles: *B. improvisus*, *B. Amphitrite*, b3-*S. balanoides*. Similar, natural surfaces are segregated by categories. Mussels: mu1-*M. galloprovincialis*, mu2-*T. plicata*, mu3-*M. edulis*, mu4-*P. perna*, mu5-*M. edulis* (Russia), mu6-*M. edulis* (UK), mu7-*M. edulis* (Germany). Seaweeds: sw-*L. japonica*. Mangroves: ma-*S. apetala*. sd-Drifting seeds. Sharks: sh1-skin, sh2-*S. canicula* eggcase. Brittle stars: bs-*O. texturata*. Crabs: cr1-*M. hardwickii*, cr2-*C. pagurus*. (b, c) Ashby plots of the dimensions of the effective antifouling topographies versus the dimension of the prevented biofoulers (ϕ). Grey bands indicate the size ranges of typical fouling organisms. Not all the cases in (a) are plotted due to the absence of detailed surface information for some cases. If the data is not directly available, reasonable estimations were made from the microscopy figures in the literature.

For example, the surface topographies of mussels and seaweeds, with feature spacing of 1-8 μm and height of 1-36 μm, can effectively prevent the attachment of

microfoulers such as diatoms, green algae spores, and barnacles at a microscopic length scale. The BM surface of the mangrove *S. apetala* featuring a ridge-like topography with lateral spacing and height of around 5 μm can prevent the fouling of tubeworms with a width of ~100 μm. More interestingly, the surface of some crab species like *M. hardwickii* can prevent the attachment of biofoulers at multiple length scales [83]. This feature may be attributed to its two-tier morphologies. A surface inspired by *M. hardwickii* carapace, with cylindrical features (diameter of 20 μm, spacing of 250 μm) surrounded by micro-spines (length of 10 μm, spacing of 7.5 μm) prevented the attachment of both diatoms and barnacles [83]. It is believed that the micro-spines are applied to tackle the microfoulers such as diatoms, and the large cylindrical projections aim to reduce macrofoulers such as barnacles. Therefore, surface topographies with a hierarchical structure should be taken into account to prevent the attachment of multiple biofoulers.

1.7 Theories on the antifouling capability of surface topographies

Biofouling is a complex process involving chemical, physical and mechanical interactions between the biofouler and the target surface for attachment. An in-depth understanding of this process in theory undoubtedly facilitates the development of antifouling strategies. However, most theories on the effects of surface topography are empirical. Theories with physics basis and prediction competence remain deficient. In the following, the prevailing theories developed to account for the effect of surface topography on the settlement of biofoulers are introduced with a focus on marine biofouling.

1.7.1 Attachment point theory

"Attachment Point Theory" [88, 89] was proposed to explain the attachment preference of biofoulers observed in experiments. The theory suggests that biofoulers prefer to settle on such sites that offer them more points of contact, nominated attachment points. Figure 1.8a schematically illustrates three sites available for the attachment of a fouler. On site A, which is smooth and flat, a potential fouler can achieve only one attachment point; on site B, which is a recessed pit with a size slightly smaller than the fouler, a potential fouler can achieve two attachment points; on site C, which is a recessed pit with a size slightly larger than the fouler, three attachment points are available. Based on the attachment point theory, site C is the favorite location for the biofoulers' attachment.

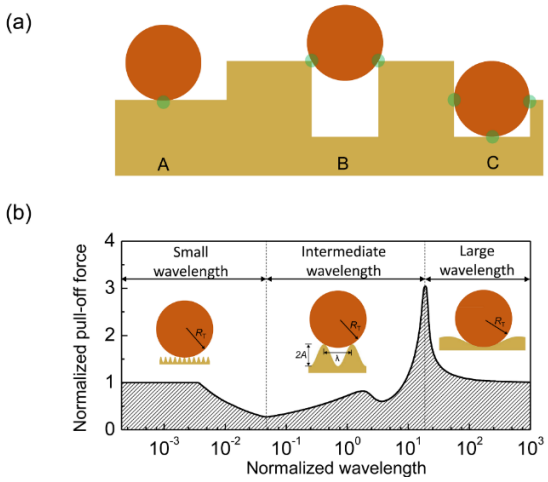

Figure 1.8. (a) Schematic illustration of three scenarios of one (A), two (B), and three (C) attachment points, respectively. (b) Theoretical estimation of the pull-off force variation between a biofouler and a wavy substrate as a function of the wavelength. Here, the pull-off force is normalized by the value between the biofouler and flat surface, and the wavelength is normalized by the radius of the biofouler [55]. The ratio between amplitude (A) and wavelength (λ) is taken as 0.5.

This theory has been often used to explain the nonuniform attachment of fouling organisms on a micropatterned surface successfully [88]. However, the deficiency of this theory is also apparent. For example, the concept of attachment point is elusive. The biofoulers are deformable rather than rigid, the contact between the biofoulers and substrate takes place through an area rather than a point. Moreover, this theory is unable to give quantitative prediction and estimation of the effect of the topography on the settlement of biofoulers.

1.7.2 Engineered Roughness Index (ERI)

To quantify the effect of engineered surface topography on the attachment of biofouler, It has been proposed a parameter called Engineered Roughness Index (ERI) to characterize the topographical features of the synthetic patterned surfaces [90]. The first version of the ERI is defined as

$$\mathrm{ERI} = \frac{r \cdot d_{\mathrm{f}}}{f_{\mathrm{d}}} \tag{1.1}$$

The ERI contains three non-dimensional numbers. *r*, known as Wenzel's roughness factor [91], stands for the ratio of the actual area of a rough surface to the projected planar surface area. d_f is the degree of freedom for the allowable movement of biofoulers on patterned surfaces. For groove-like pattern, d_f is equal to 1 and for pillar array-like pattern, d_f is equal to 2. f_d represents the ratio of the depressed surface area between protruded features and the projected planar surface area. The fouling density of *Ulva* spores on engineered surfaces was found to depend on the ERI of the surface in a negative linear manner [90].

To account for the distinct resistance to biofouling as exhibited by the pattered surfaces mimicking the shark skin, a modified version of ERI was proposed [92]

$$\mathrm{ERI}_{\mathrm{mod}} = \frac{r \cdot n}{f_d} \tag{1.2}$$

where the degree of freedom (d_f) in the original ERI is replaced by the variable n, the number of distinct features in the design (if the surface is flat, n is 0). Regression analysis based on the multiple experimental data [90, 93] indicated that $\mathrm{ERI}_{\mathrm{mod}}$ is more suitable than the ERI in describing the effect of surface topography on attachment density. Similar to ERI, $\mathrm{ERI}_{\mathrm{mod}}$ was found negatively related to the fouling density: the higher the $\mathrm{ERI}_{\mathrm{mod}}$ the lower the fouling density. Nevertheless, both ERI and $\mathrm{ERI}_{\mathrm{mod}}$ are proportional to Wenzel's roughness factor (r), which implies a potential dilemma in theory. The Wenzel's roughness factor can be written as $r = \frac{\cos\theta_W}{\cos\theta_e} > 0$ [91], where θ_e is the contact angle on a perfectly smooth surface of a material and θ_w is the apparent contact angle on a patterned surface of the same material. For hydrophilic materials (i.e., $\cos\theta_e > 0$), increasing r would lead to smaller θ_W and therefore higher hydrophilicity; in contrast, for hydrophobic materials (i.e., $\cos\theta_e < 0$), increasing r would lead to larger θ_W and therefore high hydrophobicity [94]. Such opposite effects caused by the roughness factor r imply that higher r may not necessarily lead to higher antifouling performance, depending on the intrinsic wettability of the material characterized by θ_e. Clearly, both ERI and $\mathrm{ERI}_{\mathrm{mod}}$ do not consider this factor.

1.7.3 Contact mechanics-based theory

To account for the excellent performance of the mangrove leaves in resisting the settlement by the tubeworms, A contact mechanics-based model to estimate the adhesion force has been proposed, characterized by the pull-off force between a biofouler and a wavy substrate with sinusoidal topography [55]. It was found that two feature sizes of the sinusoidal topography (i.e., amplitude A and wavelength λ) relative to the size of the potential biofouler play a pivotal role in determining the bonding force between them. To exert the best efficacy of the topographical cues of a surface in reducing the adhesion of the biofoulers, the wavelength should be appropriately designed. Overlarge or undersized wavelength would lead to higher adhesion between the fouler and substrate (Figure 1.8b). Moreover, the amplitude should be large enough to avoid the occurrence of intimate contact (Wenzel-mode contact) between the biofouler and the substrate.

Chapter 2 Predicting biofoulers attachment density with a data-driven approach

2.1 Introduction

The attachment of biofouling organisms on solid surfaces is a complex biochemical process affected not only by environmental variables such as temperature, salinity, pH value, flow rate, and nutrition abundance but also by the structural and physical features of the solid to be attached, such as its surface morphology and stiffness. Understanding the dependence of biofouling attachment on these influencing factors will be of great value to the effective control of biofouling. So far, extensive studies have been carried out to investigate the attachment behavior of diverse biofouling species under different controlled conditions. Water flow rate directly affects the attachment of biofoulers [95]. Moreover, such influence exhibits species dependence. For example, at flow rates higher than 50 cm s^{-1}, the cryptic *Bugula neritina* can still attach to the studied surface, while *Hydroides elegans* cannot. High flow rate not only reduces the engaging time of a larva for settlement on a surface but also increases the resultant drag force and affects biofilms' growth. Moreover, it has been shown that 94% of 141 fouler species are phototactic, meaning their attachment changes based on the local irradiance level [96]. Nevertheless, it was demonstrated that fouling organisms tend to avoid direct contact with sunlight, resulting in a non-linear distribution through the seawater depth. For example, the larvae attachment density of the ascidian *Ciona intestinalis* is higher at depths between 4.5 m to 8.5 m [97]. Further, the upsurge of foulers around decks and anchored boats can be attributed to the sufficient provision of nutrients around coastal areas due to organic matter decomposition (micro-

organisms or detritus) [98]. In laboratory experiment conditions, nutrition abundance relies on the amount of feeding, the population of foulers, and the volume of the water tank.

In addition to the environmental factors, the larvae and surface attributes influence the attachment density of organisms. For example, it has been shown that the characteristic size of larvae is essential to their attachment location choice [99]. Similar results were found by others [88, 90]. Recently, a theory that explains the attachment of foulers through contact mechanics has been developed, validating the significance of larvae and surface features dimensions [55]. The latter also implied that not only the surface morphology but also its elastic properties are important. Indeed, through analyzing the settlement of the barnacle *Balanus amphitrite* on PDMS surfaces with different elastic properties, it has been found that lower attachment densities on surfaces with reduced elastic moduli [100]. In addition, it has been shown that the tubeworm *Ficus enigmaticus* has a quasi-linear increase in the attachment density of larvae, with the testing time ranging from 24 h to 96 h [101].

Despite these findings and achievements, it is still extremely challenging to draw a general conclusion of how different influencing factors affect the attachment efficiency of fouling organisms, because the results obtained are species-dependent and scattering. It is still unclear if there is a universal rule governing the attachment efficiency of biofouling organisms. In view of these problems, here we propose a data-driven method in an attempt to correlate the attachment density, a quantity characterizing the efficiency of attachment, and multiple influencing factors. Meta-analysis is carried out based on the published results of multiple studies on different species irrespective of their specific attachment mechanisms [102]. Our goal is to find

a general quantitative description of the attachment density as a function of multiple influencing factors.

2.2 Materials and methods

2.2.1 Regression analysis

Consider a summation of $\sum_{m=1}^{N} \delta\left(\frac{e_m}{s}\right)$, where e_m stands for the residual given by

$$e_m = \widetilde{\Pi}_{1,m} - \hat{\widetilde{\Pi}}_{1,m} = \widetilde{\Pi}_{1,m} - \left(k_1 + \sum_{\mathrm{i}=2}^{7} k_i \cdot \widetilde{\Pi}_{i,m} + \sum_{\mathrm{i}=2,\mathrm{j}=2}^{7,7} k_{ij} \cdot \widetilde{\Pi}_{i,m} \cdot \widetilde{\Pi}_{j,m} \right)$$

and $s = \frac{\mathrm{median}|e_m - \mathrm{median}|e_m||}{0.6745}$. Here, function $\delta(\cdot)$ stands for the likelihood function of the distribution of the residuals. Following Huber's method [103], we take

$$\delta(z) = \begin{cases} z^2, & |z| < c \\ |2z|c - c^2, & |z| \geq c \end{cases} \quad \text{with } c = 1.345$$

By minimizing the summation $\sum_{m=1}^{N} \delta\left(\frac{e_m}{s}\right)$, the coefficients k_i (i = 1, ⋯,7) and k_{ij} (i = 2, ⋯,7; j = i, ⋯,7) can be determined by solving the following derivative equations

$$\frac{\partial\left[\sum_{m=1}^{N} \delta\left(\frac{e_m}{s}\right)\right]}{\partial k_{\mathrm{i}}} = 0, \ (i = 1, \cdots, 7)$$

$$\frac{\partial\left[\sum_{m=1}^{N} \delta\left(\frac{e_m}{s}\right)\right]}{\partial k_{ij}} = 0, \ (i = 2, \cdots, 7; j = i, \cdots, 7)$$

Above algorithm has been incorporated into the NCSS statistical software, by which we carried out the regression based on the published data in the literature mentioned above.

2.2.2 Data selection and assumptions

The 215 datasets applied in this paper are from 12 published papers [55, 80, 83, 88, 90, 95, 99-101, 104-106] and it is available online [102]. However, the values of some influencing variables may have not been explicitly indicated in some studies. Under such circumstance, inference should be carried out to estimate the value of that variable. In our study, the following inferences have been made:

- In J. Fu, H. Zhang [55] the irradiance was not indicated. However, as it was a research carried out in our lab, we estimated the irradiance on the surface by inquiring the lamp potency and its distance to the experiment. As a representative laboratory condition, such value of irradiance was also adopted for the studies of A.M. Brzozowska, F.J. Parra-Velandia [83], N. Ahmed, T. Murosaki [100], R. Gabilondo, H. Graham [101], M.J. Vucko, A.J. Poole [105].
- In P. Qian, D. Rittschof [95], the volume of tank was estimated as 4000 mL, equal to the "head tank" described in the paper.
- The features' geometries in the studies by J.F. Schumacher, M.L. Carman [90], J.F. Schumacher, N. Aldred [104] have distinct features along different axes. Howbeit, we took the lateral period as λ.

Moreover, the stiffness of substrate in each attachment test was estimated, as shown in Table 2.1.

Table 2.1. Estimation of each material elastic modulus, according to references.

Material	Elastic modulus [MPa]	Reference	Applied to data from
PDMS	2	Z. Wang, A.A. Volinsky [107]	J. Fu, H. Zhang [55], M.E. Callow, A.R. Jennings [88], J.F. Schumacher, M.L. Carman [90], R. Gabilondo, H. Graham [101], J.F. Schumacher, N. Aldred [104], M.J. Vucko, A.J. Poole [105]
Glass	70000	W.D. Callister [108]	J. Fu, H. Zhang [55], A.M. Brzozowska, F.J. Parra-Velandia [83], P. Qian, D. Rittschof [95], R. Gabilondo, H. Graham [101]
Polyimide	2700	M. Davidson, Steve Bastian, and Finley Markley. [109]	A.J. Scardino, E. Harvey [80], A.J. Scardino, J. Guenther [99]
Polycarbonate	2100	E. Baur, T.A. Osswald [110]	A.J. Scardino, E. Harvey [80], A.J. Scardino, J. Guenther [99]
Polystyrene	3000	W.D. Callister [108]	N. Ahmed, T. Murosaki [100], R. Gabilondo, H. Graham [101]
Polyvinyl chloride*	8	G. Wypych [111]	P. Qian, D. Rittschof [95]
Polyethylene	200	E. Baur, T.A. Osswald [110]	P. Qian, D. Rittschof [95]
Polyurethane	7	L.W. McKeen [112]	P. Qian, D. Rittschof [95]
Polytetrafluoro ethylene	500	W.D. Callister [108]	P. Qian, D. Rittschof [95]

*All the PVCs stated in the paper were assumed to have the same elastic modulus.

2.2.3 Tubeworms' attachment tests

Tubeworms (*Hydroides elegans*) were collected from a fisherman's farm from Kei Ling Ha Lo Wai in Hong Kong (22°25'27.5"N, 114°16'39.5"E). The calcareous tubes were manually broken, and each worm was placed into 100 µL filtered seawater (0.22 µm mesh size) for eggs or sperms release. To promote fecundation, eggs and sperms

were transferred to a single container with filtered seawater. Fertilized eggs were kept at 20°C in a 12L:12D cycle of lighting and daily fed with *Isocrysis albana*. After 6 days, the tubeworm larvae were ready for the attachment test. Testing PDMS specimens were placed in Petri dishes containing 10 mL seawater and 50 tubeworm larvae. Artificial stimuli were applied (CsCl, 5mmol·L^{-1}) to induce settlement. Irradiance was calculated as 7.96 W·m^{-2}. After 48 h, the specimens were rinsed by seawater and the attached tubeworms were counted with the aid of an optical microscope.

2.2.4 Fabrication of PDMS specimens and nanoindentation tests

Four PDMS/hardener ratios were adopted: 1:20, 1:15, 1:10 and 1:5 to fabricate PDMS specimens of different stiffnesses. Nanoindentation tests (Hysitron TI900) were performed to measure the modulus of the fabricated PDMS specimens. Berkovich tip and a maximum load of 30 μN were applied.

2.3 Results and discussions

2.3.1 Buckingham π theorem

In engineering, applied mathematics, physics, and biology, Buckingham π theorem [113] is a widely-applied theorem for dimensional analysis. The theorem states that if there is a physically meaningful equation involving a certain number n of physical variables, then the original equation can be rewritten in terms of a set of $p = n - m$ dimensionless variables (or parameters) Π_i (i =1, ⋯, p), which are referred to as "Π

groups" and can be constructed from the original variables [113]. Here, m is the number of physical dimensions of the problem involved (*e.g.*, length, mass, time). The selection of the dimensionless parameters Π_i (i =1,⋯, p) is not unique. Buckingham π theorem provides a method to construct these dimensionless parameters from the given variables, even though the form of the original equation remains unknown. This feature makes the theorem quite applicable to the biofouling problem whose determinants and the physics involved has not been fully understood yet.

To identify the parameters affecting the attachment of fouling organisms, let us make a review of the settlement test that is commonly adopted to characterize the attachment efficiency of a biofouling species. Figure 2.1 shows a typical experimental setup for the settlement test, in which a testing plate is mounted on the bottom of a tank full of filtered seawater, simulating the marine environment. A given number of larvae of a specific fouling species are placed into the tank and nurtured with necessary food feeding and lighting. Sometimes, circulating seawater is introduced into the tank to simulate the effect of flow rate in the real marine environment. After a given time, the testing plate is removed from the tank, and the number of attached fouling organisms is counted. The attachment density (a), defined as the number of attached organisms per unit area, is used to characterize the attachment efficiency. Reducing attachment density is the common objective of most anti-biofouling endeavors. In this simplified experimental model, the conceivable parameters that affect the attachment density include the concentration of available larvae (ρ), experiment time (t), flow rate (Q), irradiance level of lighting (W), nutrition abundance in the seawater which is related to the tank volume (V). Recent studies indicated that the elastic modulus (E) and surface morphology of the material being attached also play an essential role in

determining attachment efficiency [55, 100]. For a solid surface with regular morphology, wavelength (λ) and asperity depth (h) are two crucial characteristic length scales that should be considered, especially in a relative sense to the characteristic size of the organism (D). Additionally, other parameters may also affect the attachment efficiency, such as pH value, salinity, and temperature. However, these factors are not considered in this study because they varied little in the biofouling tests done under laboratory conditions.

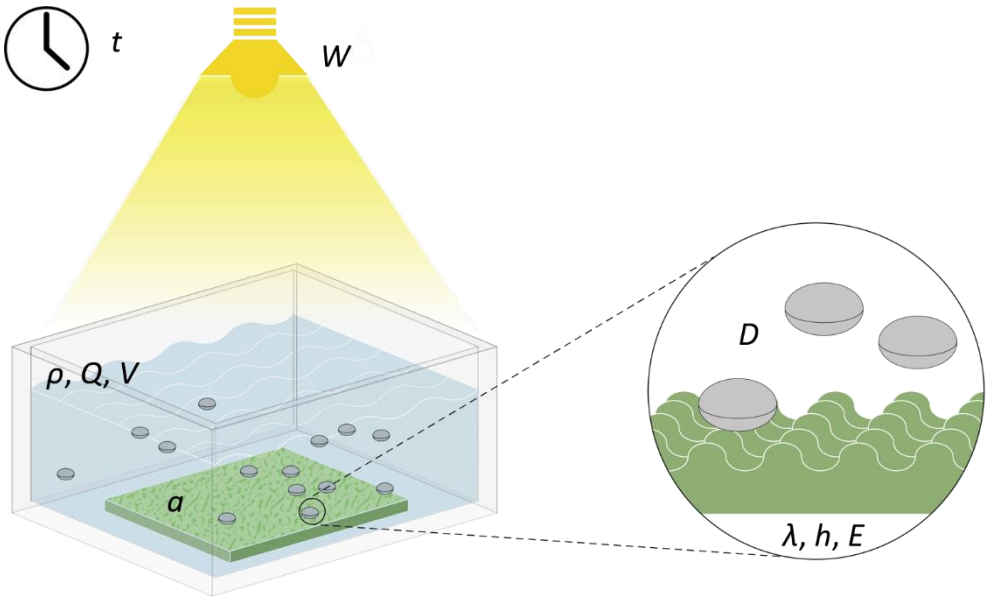

Figure 2.1. Schematics showing the setup of a laboratory settlement experiment.

The above description of the determining factors in a typical laboratory biofouling test allows us to proceed further with the Buckingham theorem. In our case, we have 10 variables and 3 dimensions, and according to the theorem, 7 dimensionless groups are established as follows:

$$\Pi_1 = a \cdot D^2, \Pi_2 = \frac{E \cdot D}{W \cdot t}, \Pi_3 = \frac{h}{D}, \Pi_4 = \rho \cdot D^3, \Pi_5 = \frac{\lambda}{D}, \Pi_6 = \frac{Q \cdot t}{D}, \Pi_7 = \frac{V}{D^3}$$

The values of many Π groups above are distributed in a wide range from zero to 10^6

(see Table 2.2); hence taking the natural logarithm of all terms is appropriate.

Table 2.2 Selected independent variables and their practical ranges: lower and upper limit.

Quantities	Unit	Lower limit	Upper limit
Available larvae concentration (ρ)	mL^{-1}	0.02	3×10^{6}
Organism size (D)	μm	2	321
Surface wavelength (λ)	μm	0	800
Asperity height (h)	μm	0	650
Surface elastic modulus (E)	MPa	1	70000
Seawater flow rate (Q)	$cm\cdot s^{-1}$	0	31.9
Seawater volume (V)	mL	0.1	4000
Time (t)	h	1	168
Light irradiance (W)	$W\cdot m^{-2}$	0	17.4

Additionally, to avoid the possible mathematical undefinition, a constant of unity is added to the terms that may take zero. Therefore, a new set of dimensionless groups are defined as follows:

$$\widetilde{\Pi}_1 = \ln(a \cdot D^2), \widetilde{\Pi}_2 = \ln\left(\frac{E \cdot D}{(1+W)\cdot t}\right), \widetilde{\Pi}_3 = \ln\left(\frac{1+h}{D}\right), \widetilde{\Pi}_4 = \ln(\rho \cdot D^3)$$

$$\widetilde{\Pi}_5 = \ln\left(\frac{1+\lambda}{D}\right), \widetilde{\Pi}_6 = \ln\left(\frac{(1+Q)\cdot t}{D}\right), \widetilde{\Pi}_7 = \ln\left(\frac{V}{D^3}\right)$$

In these groups, $\widetilde{\Pi}_1$, which is correlated to the attachment density, is regarded as a function of the other six groups or variables, namely,

$$\widetilde{\Pi}_1 = f(\widetilde{\Pi}_2, \widetilde{\Pi}_3, \widetilde{\Pi}_4, \widetilde{\Pi}_5, \widetilde{\Pi}_6, \widetilde{\Pi}_7) \qquad (2.1)$$

2.3.2 Regression analysis

Regression analysis is a technique used to seek the relationship between one or more independent variables and a dependent variable. In our case, we assume that the effect of each independent variable is additive. The predicted value of the dependent variable, $\widehat{\widetilde{\Pi}}_1$, thus can be approximated as a quadratic polynomial function of the independent variables $\widetilde{\Pi}_i$ (i=2, …, 7)

$$\widehat{\widetilde{\Pi}}_1 = k_1 + \sum_{i=2}^{7} k_{\mathrm{i}} \cdot \widetilde{\Pi}_{\mathrm{i}} + \sum_{i=2}^{7} \sum_{j=i}^{7} k_{\mathrm{ij}} \cdot \widetilde{\Pi}_{\mathrm{i}} \cdot \widetilde{\Pi}_{\mathrm{j}} \qquad (2.2)$$

where coefficients k_{i} (i = 1, ⋯,7) and k_{ij} (i, j = 2, ⋯,7) are to be determined via regression. Eq. (2.2) can be deemed as the second-order approximation of the function f in Eq. (2.1). The widely applied method to determine the coefficients in an assumed expression is ordinary least square (OLS), which tends to be sensitive to the data peculiarities such as outliers, multicollinearity and heteroscedasticity. For examples, in the OLS method all inputs are equally weighted and thus uniformly important. In our case, outliers are naturally present. Moreover, due to the inclusion of some variables, such as diameter D, in multiple Π groups, multicollinearity also exists. The existence of outliers and multicollinearity would generate abnormal data distribution. Under such circumstance, robust regression methods should be applied as they require less restrictive assumptions to calculate the regression coefficients [114, 115].

The values of all coefficients obtained from the above-mentioned robust regression are shown in Table 2.3 together with their corresponding p-values which indicate whether the correlation between the dependent variable $\widetilde{\Pi}_1$ and the corresponding independent variable is significant or not. Normally, 0.05 is adopted as the threshold for significance. If p-value is less than 0.05, the correlation between them is deemed

significant. For example, the p-values corresponding to k_2, k_4, k_7, k_{22}, k_{44}, and k_{77} are close to zero, implying that the substrate stiffness, larvae concentration (ρ) and the container volume (V) significantly determine the attachment density (a).

Table 2.3. Results of robust regression, showing the coefficients values and their respective p-values.

Coefficient	Regression value	p-value	Coefficient	Regression value	p-value
k_1	-2.01913	0.1077	k_{34}	-0.08266	0.0292
k_2	0.69742	0.0077	k_{35}	0.14724	0.0761
k_3	-0.18372	0.6190	k_{36}	0.00625	0.9658
k_4	4.17394	0.0000	k_{37}	-0.16189	0.0202
k_5	-0.10871	0.7273	k_{44}	-0.20887	0.0000
k_6	0.04582	0.9220	k_{45}	-0.01309	0.6593
k_7	3.91912	0.0000	k_{46}	-0.40882	0.0000
k_{22}	-0.0329	0.0019	k_{47}	-0.11437	0.0001
k_{23}	-0.03353	0.6946	k_{55}	-0.06935	0.1380
k_{24}	-0.0505	0.0141	k_{56}	-0.08815	0.3789
k_{25}	0.02279	0.7418	k_{57}	0.01828	0.7248
k_{26}	-0.0986	0.0113	k_{66}	-0.33666	0.0000
k_{27}	-0.0022	0.8964	k_{67}	-0.07759	0.1190
k_{33}	-0.08884	0.1378	k_{77}	0.04203	0.0090

Figure 2.2a shows the values of $\widetilde{\Pi}_1$ predicted by the regression expression in comparison with the experimental observations. It can be seen that most of the data points are distributed around the line of $y = x$ irrespective of the fouling species, implying the strong and universal prediction competence of the regression expression of Eq. (2.2). To further investigate the quality of the regression results, Figure 2.2b shows the distribution of the residuals between the predicted data and their

experimental counterparts. The highest frequency peak in the vicinity of zero indicates that most of the residuals are zero and the regression expression agrees well with the experimental results. The curve shows a Gaussian-like distribution. As stated before, our data possess outliers, which are evident here. By using a robust regression, we reduced the count of non-zero residuals and therefore reduced their impact. The distribution of the residuals in the spaces of each independent variable, $\widetilde{\Pi}_i (i = 2, \cdots, 7)$, and their products, $\widetilde{\Pi}_i \cdot \widetilde{\Pi}_j (i, j = 2, \cdots, 7)$, are plotted in Figure 2.3.

To further evaluate the quality of regression, we calculated the coefficient of determination (R^2), and the predicted residual error sum of squares (PRESS) R^2 (see Table 2.4). Both R^2 and PRESS R^2 are close to 1.0, implying the high quality of our regression.

After predicting $\widetilde{\Pi}_1$, the attachment density can be easily calculated through

$$a = \exp(\widetilde{\Pi}_1)/D^2$$

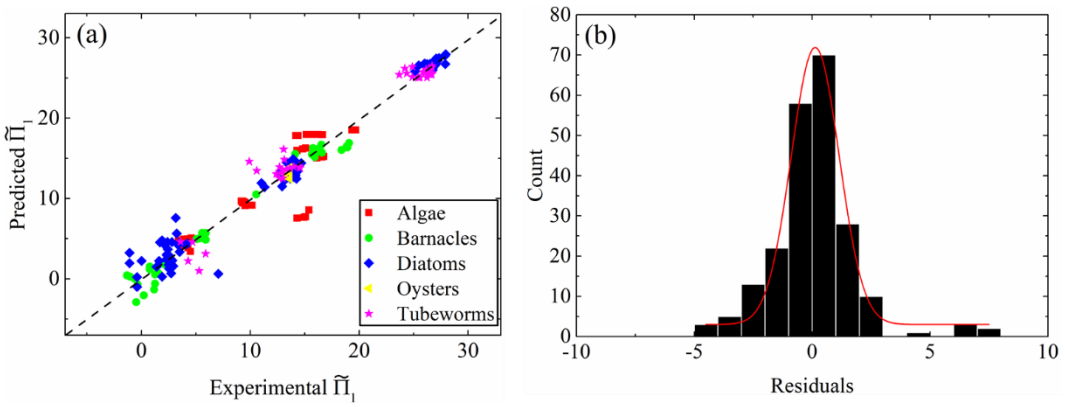

Figure 2.2. Meta-analysis results. (a) Predicted $\widetilde{\Pi}_1$ versus experimental $\widetilde{\Pi}_1$ highlighting the great linear correlation independent of the biofouler species. (b) Histogram of the residuals of $e_m = \widetilde{\Pi}_{1,m} - \widehat{\widetilde{\Pi}}_{1,m}$ and the corresponding fitting curve for a Gaussian distribution (mean μ =0.12, standard deviation σ = 1.02).

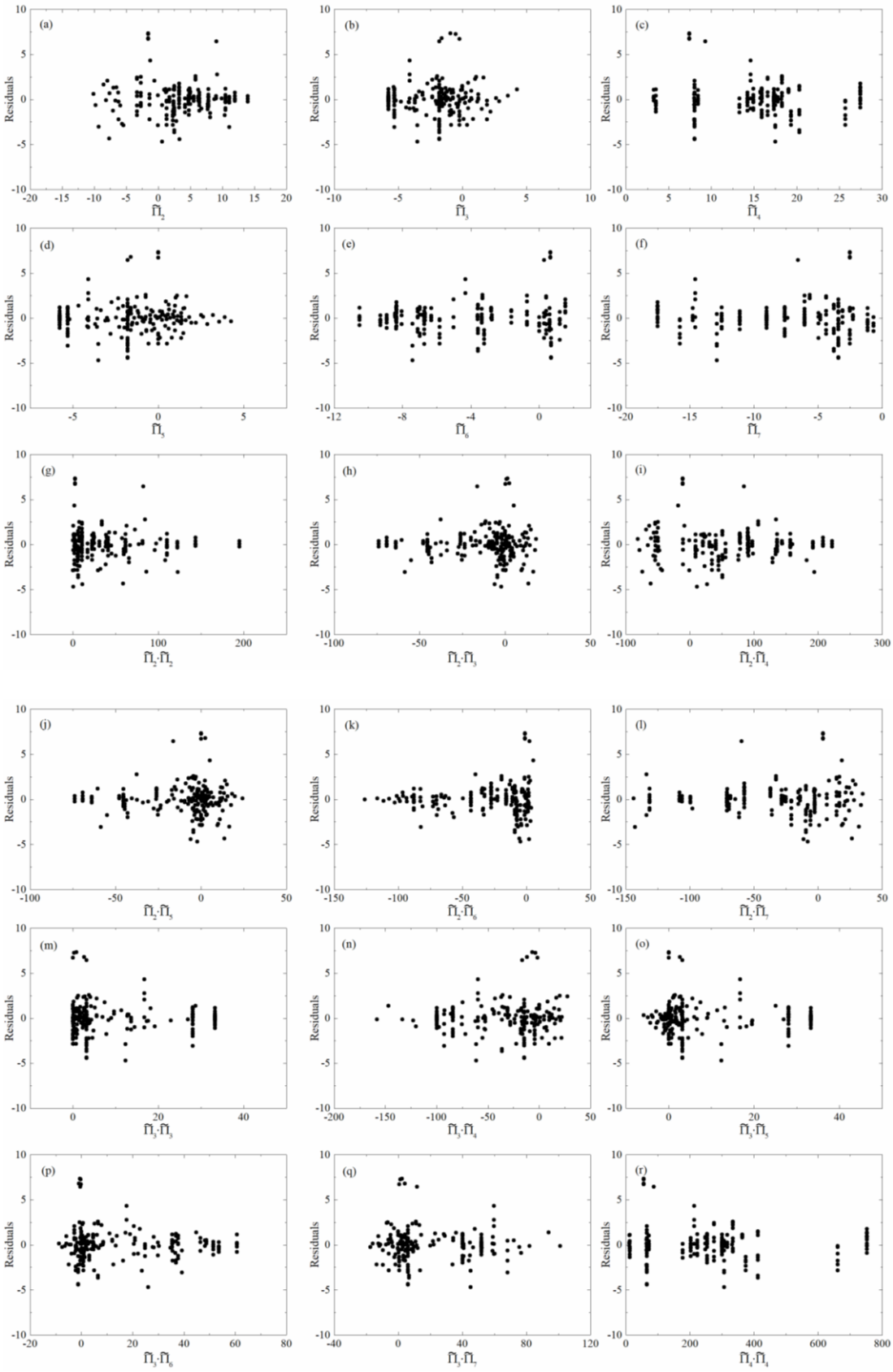
(a)
(b)
(c)
(d)
(e)
(f)
(g)
(h)
(i)
(j)
(k)
(l)
(m)
(n)
(o)
(p)
(q)
(r)
Residuals

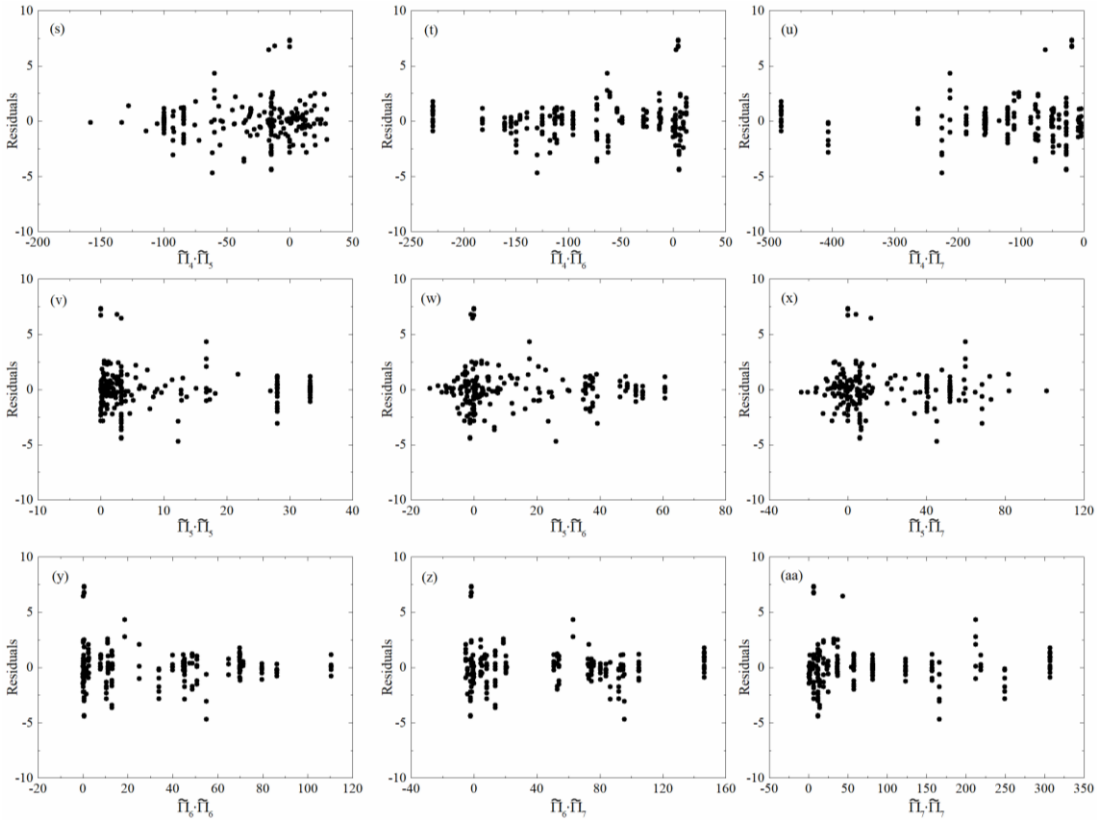

Figure 2.3. Distribution of the residuals in the spaces of different independent variables and their products.

Table 2.4. Quality of regression: coefficient of determination and predicted residual error sum of squares (PRESS).

Quantities	**Definition**	**Value**
Coefficient of determination (R^2)	$1-\frac{\sum_{m=1}^{N}(f_m-\bar{\bar{\tilde{\Pi}}}_{1,m})^2}{\sum_{m=1}^{N}(\tilde{\Pi}_{1,m}-\bar{\bar{\tilde{\Pi}}}_1)^2}$	0.9809
PRESS (Predicted residual error sum of squares) R^2	$1-\frac{\sum_{m=1}^{N}(\tilde{\Pi}_{1,m}-f_{m(m)})^2}{\sum_{m=1}^{N}(\tilde{\Pi}_{1,m}-\bar{\bar{\tilde{\Pi}}}_1)^2}$	0.9486

Here, f_m stands for the m^{th} response value given by the function f which is obtained by regression on the basis of all N datasets; $f_{m(m)}$ stands for the m^{th} response value given by the function f which is obtained by regression on the basis of datasets with the m^{th} one excluded individually.

2.3.3 Effect of variables to the attachment of foulers

The regression results obtained above allows us to predict the dependence of attachment density on different determining factors quantitively for different species with distinct characteristic sizes and contrasting attachment mechanisms. For instance, take the characteristic sizes of four foulers: barnacle *B. neritina*, tubeworm *H. elegans*, algae *C. clavulatum* and *U. linza* as 321 μm, 200 μm, 37 μm and 5 μm, respectively. Figure 2.4a shows the dependence of attachment density on the stiffness of the substrate (E). Here, we assume that the substrate is flat with $h = \lambda = 0$ under laboratory light irradiance (W = 7.95 W·m^{-2}), steady seawater conditions (Q = 0) in a container of 10 mL with an initial larvae concentration of 5 per mL. The total time for attachment was set as t = 48 h. Results in Figure 2.4a indicate the consentaneous effect of low substrate stiffness in reducing the attachment density of all organisms. Therefore, in marine industry, applying soft paint on ship hulls is expected to reduce the attachment of fouling organisms. Figure 2.4b shows the effect of flow rate on the attachment density of different species on a given substrate with stiffness E = 2 MPa and surface topography characterized by $h = \lambda$ = 10 μm. It is assumed that 1000 fouling organisms are added in a container of 100 mL. It is clear to see that flow rates higher than 4 cm·s^{-1} will drastically reduce the attachment density and essentially eradicate it when above 8 cm·s^{-1}, irrespective for all fouling species, implying that marine ships tend to be fouled when they are anchored or voyaging at low speed.

Figure 2.4c displays the effect of surface asperity height (h) of the substrate on the attachment density. Here, we assume that V = 10 mL, ρ = 10 mL^{-1} and surface wavelength λ = 10 μm. It can be seen that the attachment density of barnacles *B. neritina* (D = 321 μm) is insensitive to the asperity height at all. However, for

tubeworms *H. elegans* (D = 200 µm), the attachment density increases as the asperity height increases and saturates when h = 21 µm. In contrast, the attachment density of algae *C. clavulatum* (D = 37 µm) exhibits the maximum value when the asperity height is approximately 50 µm, while the attachment density of *U. linza* (D = 5 µm) drops drastically with the increase of asperity height. In addition, Figure 2.4d presents the impact of surface wavelength while setting asperity height h = 10 µm. Except for tubeworms *H. elegans* (D = 200 µm) that has a peak of attachment density when wavelength λ = 8 µm, the prevailing behavior is to reduce attachment density when increasing surface wavelength.

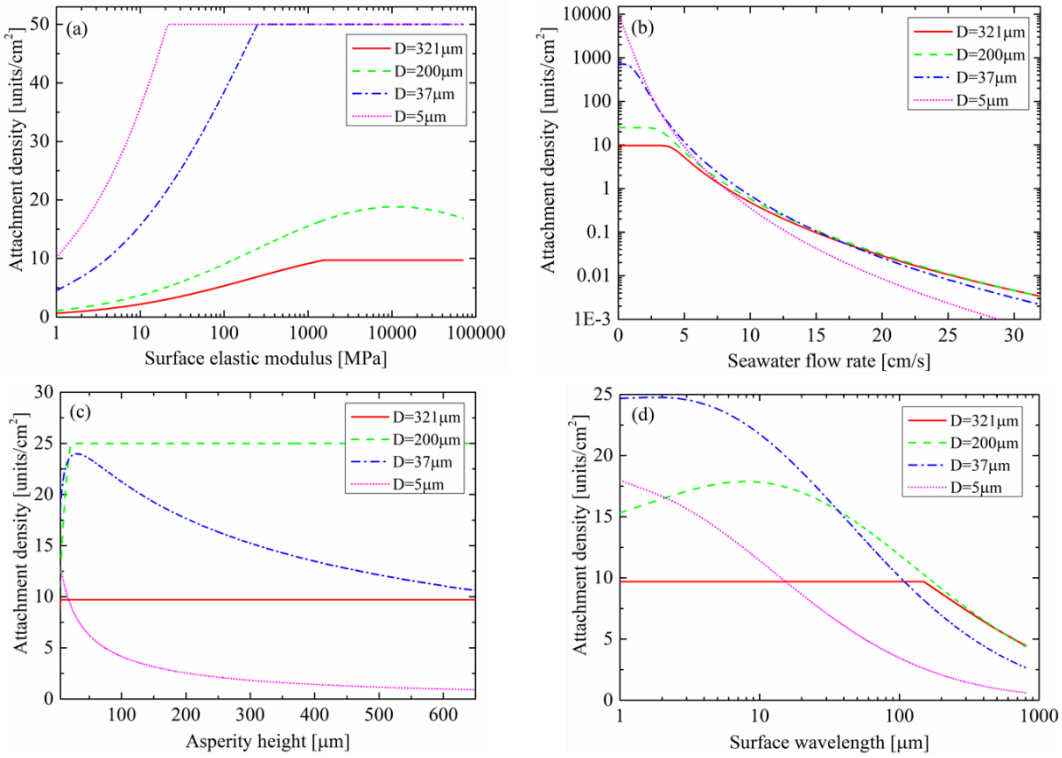

Figure 2.4. Influence of different factors to the attachment density calculated using the prediction model: (a) surface elastic modulus. (b) seawater flow rate. (c) asperity height. (d) surface wavelength. Following parameters are kept constant in each case: (a) $h = \lambda = 0$, W = 7.95 W·m^{-2}, $Q = 0$, V = 10 mL, ρ = 5 mL^{-1}, t = 48 h; (b) E = 2 MPa, $h = \lambda$ = 10 µm, W = 7.95 W·m^{-2}, V = 1000 mL, ρ = 10 mL^{-1}, t = 48 h; (c) E = 2 MPa, λ = 10 µm, W = 7.95 W·m^{-2}, V = 10 mL, ρ = 10 mL^{-1}, t = 48 h; (d) E = 2 MPa, h = 10 µm, W = 7.95 W·m^{-2}, V = 10 mL, ρ = 10 mL^{-1}, t = 48 h.

2.3.4 Validation through experimental test

To verify the capability of the above model in predicting the attachment density of fouling species, an attachment test was carried out by using tubeworms in PDMS surfaces with different stiffness. These surfaces properties were varied by changing the material mix ratio. The nanoindentation results show a lowest modulus of 1.132 MPa, while a higher of 4.335 MPa (see Table 2.5). Figure 2.5 shows the experimental measurement of the attached density of the tubeworms on PDMS substrates with different stiffnesses in comparison to the prediction given by the above regression model. The small difference between them implies the applicability of our model in predicting the effect of substrate stiffness on the attachment efficiency of tubeworms. In summary, we successfully developed an empirical method to reveal the quantitative dependence of attachment density of biofouling species on a series of determining factors. Buckingham π theorem and robust regression were applied to determine the regression expression from the existing published datasets in literature. The obtained empirical expression from such meta-analysis shows a versatile competence in predicting the attachment density of biofoulers irrespective of the fouling species, laboratory conditions and substrate stiffness. Our model not only provides an approach to predict the attachment efficiency of a variety of fouling species on different kinds of substrates but also indicates the directions of antifouling efforts in naval industry.

Table 2.5. Variations on the surfaces' modulus due to different PDMS/hardener ratios.

PDMS/Hardener ratio	Modulus [MPa]
1:20	4.335
1:15	1.867
1:10	1.712
1:5	1.132

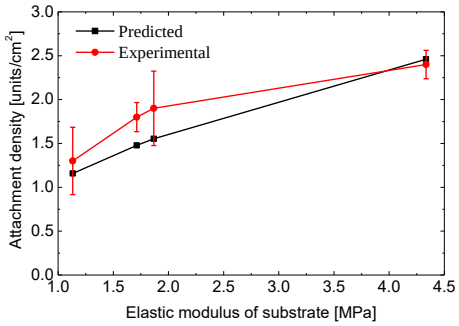

Figure 2.5. Comparison of the predicted attachment density, using the developed model, to the experimental attachment density, varying the substrate elastic modulus.

2.4 Summary

The attachment efficiency of biofouling organisms on a solid surface depends on a variety of factors including species of the fouler, nutrition abundance, salinity, temperature, flow rate, surface morphology and mechanical properties of the solid to be attached and so on. So far, extensive research has been carried out to investigate the effects of these factors on the attachment behavior for various fouling species. However, the obtained results are normally species-dependent and seemly scattering. There is no universal rule that can be applied to predict the attachment efficiency under given conditions. To solve this problem, in this Chapter it is presented a meta-analysis on the effects of 10 selected factors on the attachment efficiency, resulting in a universal quantitative correlation between the attachment density and the selected factors. In data science, it is important to not validate the model using the training data (input used to create the model). In our case, the model is experimentally validated by an attachment test of tubeworms (*Hydroides elegans*) on PDMS surfaces with controllable stiffness. The results provide a practical approach to quantitatively predict the attachment efficiency of fouling organisms and should be of great value to the design of anti-biofouling materials and structures.

Chapter 3 Reconciling the conflict between optical transparency and fouling resistance with nanowrinkled surface inspired by zebrafish's cornea

3.1 Introduction

Optical surfaces applied in harsh environments are prone to the accretion of foreign matters, including organic and inorganic molecules, particles, bacteria and viruses, and even sessile animals, leading to functional and economic detriments in a broad spectrum of applications. For instance, healthcare products [116] such as endoscopic cameras and contact lenses tend to be colonized by bacteria, resulting in high infection risks to patients and users. The attachment and proliferation of sessile animals in the ocean, such as barnacles and tubeworms, on underwater cameras and submarine windows cause material deterioration and loss of vision (Figure 3.1), ruining the optical functionality of the concerned devices [2]. Desert solar farming, an emerging industry for collecting solar energy, suffers from the accumulation of sand, dust, and other inorganic particles on solar panels, drastically reducing energy conversion efficiency [117]. Controlling the accretion and fouling of other matters on these optical surfaces is challenging since the potential solutions to preventing fouling tend to interfere with optical transparency.

Different strategies have been proposed to reconcile the conflict between fouling resistance and optical transparency [118-124]. For example, chemical coatings were applied to reduce fouling attachment with no significant sacrifice of the optical transparency [120, 123]; however, the compositions of these coatings might be chemically active [125] and may bring adverse side effects to the potential users. For

example, some toxic chemical compounds have been shown to cause drastic alterations to ecosystems, such as physiological alterations in mollusks and fishes [16, 126] and broad waterways contaminations [12]. Topographical modifications such as the inclusion of micro- and nano topographical features have been confirmed as an effective and environmentally friendly method to enhance the fouling resistance of surfaces [127, 128], but their influence on the optical properties is not well understood. A film with nanowires deposited on the surface achieved superior resistance to marine fouling and acceptable transmittance of light, but its high degree of haze may affect its visual quality [121]. Nanospikes inspired by moth-eye showed good optical transparency and acceptable fouling resistance, which relied on surface chemical treatments [119, 124]. Liquid-infused porous surfaces (SLIPS) offered promising fouling resistance against marine algae [118], blood, and mucus [122, 129]. Despite their high optical transparency, they require frequent refilling of lubricants [122]. Moreover, their high manufacturing costs are also a barrier to mass production [130]. By far, strategies for compromising the conflict between fouling resistance of surface topographies and the accompanying interference with the optical transparency are still in urgent need.

In this chapter, we cast our attention to Mother Nature with a focus on the corneal tissues of fishes which are believed to encounter a similar challenge as we do and most probably have already found effective solutions through millions of years of evolution. Earlier anatomical studies revealed that the outer surface of the cornea of zebrafish (*Danio rerio*) is covered with nanowrinkles [131]. Similar nano topographies but of different geometries were also observed on the corneal tissue of other vertebrates [132-134], such as mammals [132], including humans [135], fishes [131, 133, 134, 136],

and even invertebrates such as cephalopods [137]. Possible functions of these surface features include tear film stability [132, 135], anti-reflectivity [137], and nutrient and gas interchange [134]. Here, we propose a hypothesis that these nanowrinkles help resist fouling while preserving the optical transparency of the tissue. To testify this hypothesis, we synthesized a series of bioinspired surfaces with wavy wrinkles. An integrated experimental and numerical analysis was carried out to investigate the effects of the wrinkles' geometrical features on the film's optical transparency and fouling resistance, respectively.

Figure 3.1. An underwater camera cover after one-month submersion in the ocean. (a) Front, (b) lateral, and (c) back views.

3.2 Materials and methods

3.2.1 Characterization of corneal tissue of zebrafish

Adult zebrafish (*Danio rerio*) were purchased from a local aquarium fish market. Ocular tissue was extracted from the zebrafish following the guidelines (ARVO Statement for the Use of Animals in Ophthalmic and Vision Research) The fisheyes were fixed overnight in cacodylate buffer (0.1 M) with 2.5% glutaraldehyde and 2% formaldehyde at 4 °C, washed with cacodylate buffer before a 2 h postfixation with 2% osmium tetroxide in the same buffer. Samples were rinsed with deionized water and dehydrated in graded ethanol series (30%, 50%, 70%, 90%, 100%, 100%; 10 min

each step). The cornea exterior surface was observed with a scanning electron microscope (Vega 3, Tescan). Topographical data was acquired with atomic force microscopy (Nanoscope 8, Bruker) and analyzed with imaging software (Gwyddion [138]). The average wavelength of the wrinkles was assessed by the inverse average of peak-to-center radial distance in the 2D FFT pattern.

3.2.2 Fabrication of bioinspired nanowrinkled surfaces

Polydimethylsiloxane (PDMS, Sylgard 184, Dow Corning) base and curing agent were mixed in a mass ratio of 10:1. The uncured PDMS was poured into a glass mold (70 mm × 30 mm × 3 mm), after degassing, curing overnight at 60 °C, and demolding, a flat PDMS strip was obtained. Then, the PDMS strip was mounted on a homemade stretcher (Figure 3.2a), which can controllably apply tensile pre-strain on the strip (Figure 3.2b). The pre-strained PDMS strip was then treated with oxygen plasma (45W, PDC-002 Plasma Cleaner, Harrick) for some time (Figure 3.2c). After releasing the strain on the strip, surface wrinkles were produced on the strip's top surface (Figure 3.2d). The characteristic dimensions (amplitude and wavelength) of the wrinkles were tuned by controlling the pre-strain (up to 70%) and the plasma exposure time in the range of 30-2000 s (Figure 3.2e).

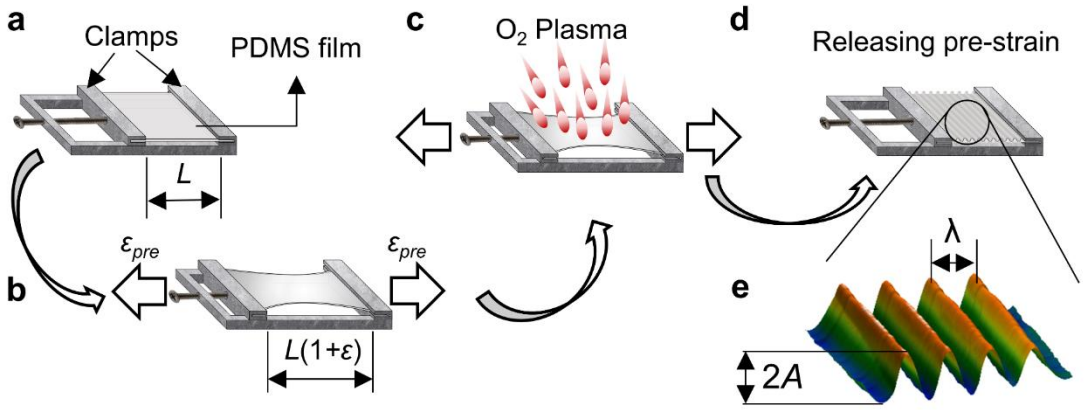

Figure 3.2. Schematics showing the manufacturing procedure of the wrinkled PDMS surfaces. (a) The PDMS film is clamped to a homemade stretcher. (b) The PDMS film is strained. (c) The pre-strained PDMS film is treated with oxygen plasma. (d) The pre-strain is released. (e) Topography of the fabricated wrinkled surface obtained by AFM scanning highlighting the wrinkles dimensional parameters: amplitude (A) and wavelength (λ).

To produce wrinkles on a curved surface, uncured PDMS was poured onto a glass semisphere (diameter: 14 mm) attached to a flat glass slide and quickly placed in an oven (120 °C) for 10 min for curing. This step was repeated two times. After demolding, a PDMS film with a semispherical shell was obtained. Then, this film was pre-strained by pressing a larger glass semisphere (diameter: 16 mm) into the concave pocket and treated with oxygen plasma (45 W, PDC-002 Plasma Cleaner, Harrick) for 250 s. After releasing the strain by removing the glass semisphere, nanowrinkles were produced on the semispherical PDMS shell, as confirmed by atomic force microscopy.

3.2.3 Topographical and modulus characterizations

Atomic force microscopy (Nanoscope 8, Bruker) in tapping mode was applied to characterize the surface topography of the wrinkled surfaces. To measure the effect of plasma treatment on the modulus of PDMS, nanoindentation tests were carried out on

smooth PDMS films treated with plasma using atomic force microscopy (Nanoscope 8, Bruker) in force-volume contact mode.

3.2.4 Wettability measurement

The contact angles of surfaces were measured using an optical tensiometer (Theta, Biolin Scientific) with a deionized water drop of 3 µL. During the experiments, the room temperature was kept constantly at 22°C. Five measurements were performed for each sample. Measurements were made after at least two weeks after the plasma treatment so that the temporary hydrophilicity of PDMS caused by plasma treatment disappeared [139].

3.2.5 Characterization of optical properties

Optical properties, such as total and diffusive transmittance, of the samples were measured with a spectrophotometer (Lambda 1050 with integrating sphere, PerkinElmer). Film samples were positioned with their surfaces perpendicularly to the light source. To measure the underwater properties, samples were placed in a cuvette filled with artificial seawater (DI water, 3.5 wt.% artificial aquarium sea salt). The light source was set to the visible light (wavelength: 380-700 nm). Haze was calculated as a ratio between the diffusive transmittance and the total transmittance.

3.2.6 Computation of optical properties

The optical properties of a film with wrinkled surfaces were also computed with software FDTD Lumerical based on a model schematically shown in Figure 3.3b. A normally incident plane wave (wavelength: 380-700 nm) was set to shoot directly at the surface. Below the wrinkled surface, the light waves are transmitted through the material, and their angles are measured on the assessing plane. If the angle is not perpendicular to the surface by more than 2.5°, the transmittance is deemed as diffusive. Otherwise, the transmittance is specular. Due to the topography periodicity, only one period is considered for the synthetic surface. For the zebrafish's corneal tissue, a larger area (2 μm × 2 μm) is considered as the wrinkles are not well aligned nor distributed. Bloch boundary conditions were applied on the lateral boundaries (BC1, BC3), while Perfectly Matched Layer (PML) boundary conditions were applied on the top and bottom boundaries (BC2, BC4). The intrinsic optical properties of the material were set based on the values experimentally measured from a smooth PDMS surface (Figure 3.3a). The surface topography of the simulated model was acquired from AFM scanning of each sample.

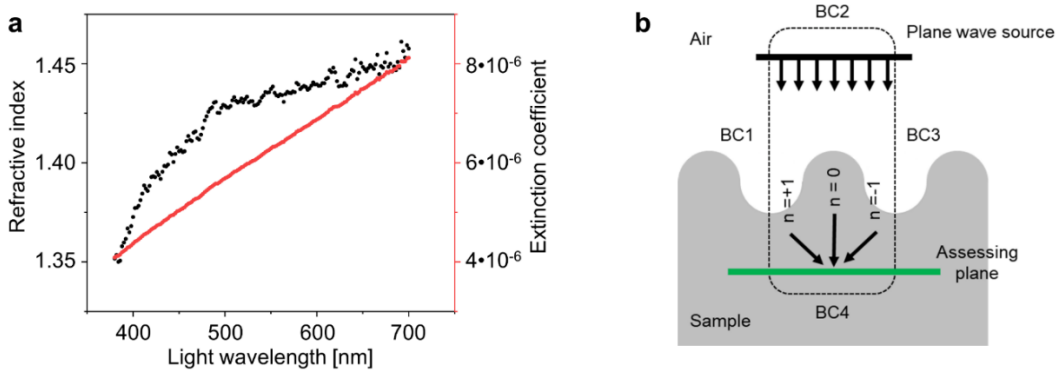

Figure 3.3. (a) Intrinsic optical properties of PDMS measured from smooth samples. (b) Schematic showing the model for calculating the optical properties of PDMS film with wrinkled surface.

3.3 Results and discussions

3.3.1 Surface topography of the corneal tissue of zebrafish

The zebrafish (*Danio rerio*) (Figure 3.4a) does not have eyelids and, therefore, its cornea, as the outmost ocular tissue, is directly subjected to the fouling pressure from the environment (Figure 3.4b). Scanning electron microscopy (SEM) of the corneal tissue displays a surface covered with randomly distributed nanowrinkles (Figure 3.4c). Topographical scanning through atomic force microscopy (AFM) shows that the wrinkles' average amplitude, namely half of the peak-to-valley distance, is around 73.5 nm (Figure 3.4d). The Fast Fourier Transformation (FFT) of the AFM-based topography displays peaks radially symmetrical to the center (inset of Figure 3.4d), from which the average wavelength of the wrinkles (λ_{avg}) is determined to be around 440 nm (Figure 3.4e) (see Experimental Section).

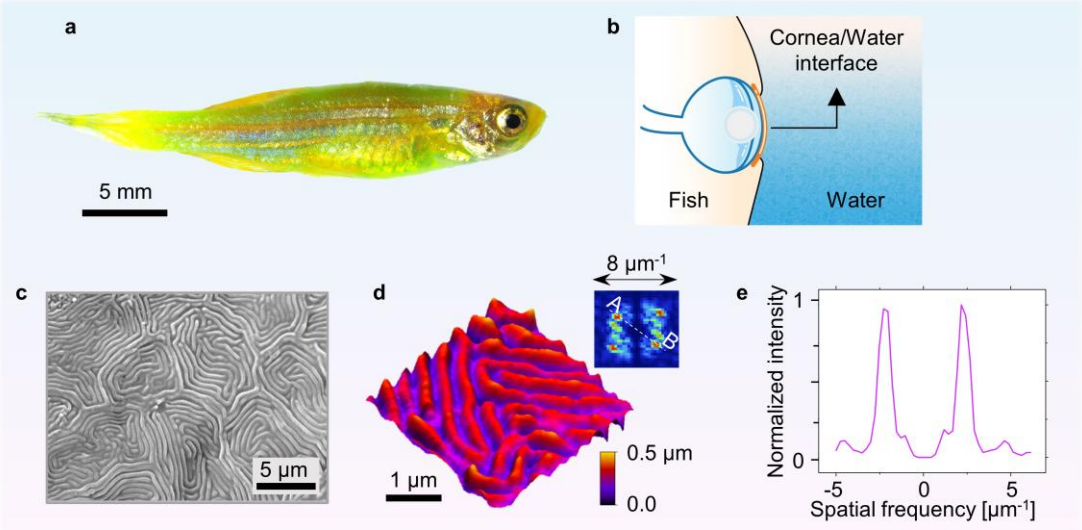

Figure 3.4. (a) Zebrafish (*Danio rerio*). (b) Schematics showing the interface between the fish's eye and the aquatic environment. (c) SEM image of the external surface of the corneal tissue and (d) topography imaging of the external surface using AFM and its 2D FFT pattern. (e) Line profile (A-B in the inset of d) extracted from the 2D FFT pattern.

Numerical simulation based on the topography obtained by AFM scanning indicates that such nanowrinkles would not affect the total transmittance and the haze of the tissue too much in the visible light spectrum (380-700 nm) in air. The optical performance underwater is even better owing to the similar refractive indexes between the corneal tissue (1.30 [140]) and water (1.33 [141]) (Figure 3.5).

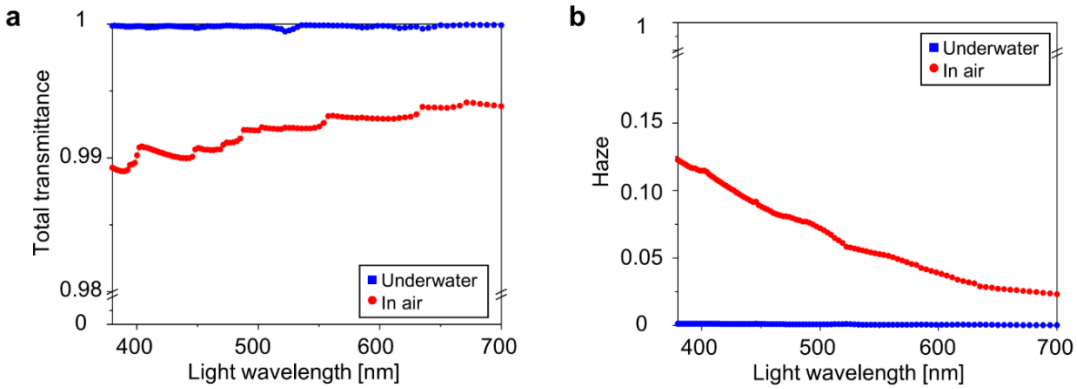

Figure 3.5. Calculated optical properties of corneal tissue of zebrafish. (a) Total transmittance and (b) haze underwater and in air.

3.3.2 Bioinspired nanowrinkled surfaces

Inspired by the nanowrinkles on the surface of zebrafish's cornea, we fabricated wrinkled surfaces by taking advantage of the mechanical instability of thin-film coatings. Typically, when a stiff coating on a thick elastomeric substrate is subjected to in-plane compression strain ε, lateral buckling of the coating happens when the compression reaches a critical level, resulting in wavy wrinkles. Elastic buckling theory predicts that the amplitude and wavelength of the resulting wrinkles are given by [142]:

$$A = h_{\mathrm{f}}\sqrt{4\varepsilon\left(\frac{\bar{E}_{\mathrm{f}}}{3\bar{E}_{\mathrm{s}}}\right)^{2/3} - 1}\,, \quad \lambda = \pi h_{\mathrm{f}}\left(\frac{8\bar{E}_{\mathrm{f}}}{3\bar{E}_{\mathrm{s}}}\right)^{1/3} \qquad (3.1)$$

where h_f is the thickness of the coating and $\bar{E}_f$ and $\bar{E}_s$ stand for the plane strain moduli of the coating and substrate, respectively. The dependence of these two characteristic length scales of the wrinkles on the mechanical properties of the coating substrate, coating thickness as well as the applied compressive strain ε allows us to fabricate wrinkles with controllable amplitudes and wavelengths. Here, we treated a pre-stretched PDMS film with oxygen plasma, which breaks the Si-CH_3 groups, yielding a glass-like stiffer Si-O_x layer [143] (Figure 3.6a).

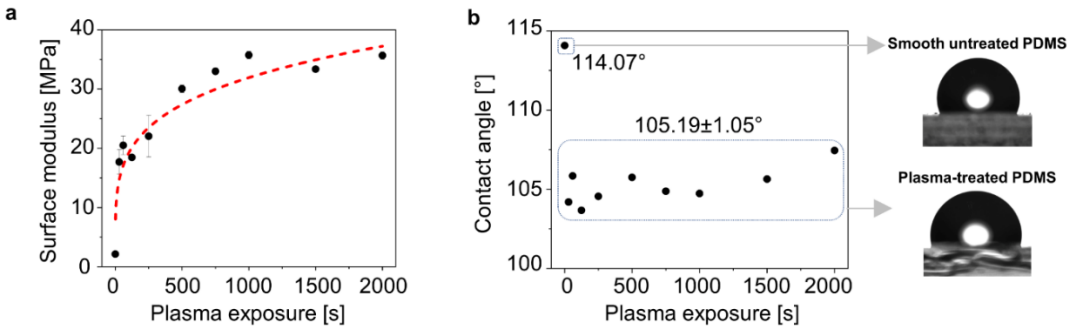

Figure 3.6. Effects of plasma exposure on the (a) modulus and (b) contact angle of PDMS films.

After releasing the pre-strain, denoted by ε_{pre}, wavy wrinkles appear on the surface due to the buckling of the stiffer coating upon the contraction of the elastic substrate (Figure 3.2). By controlling the pre-strain and the plasma exposure time, which affects the modulus of the coating, we fabricated surface wrinkles with amplitude (A) ranging from 1.2 to 685.7 nm and wavelength (λ) spanning from 325.7 to 6741 nm (Figure 3.8a). The wavelength is mainly influenced by plasma exposure time (Figure 3.7a), while the amplitude is determined by both pre-strain and time of plasma exposure (Figure 3.7b). This is consistent with the prediction by the buckling theory as described in Eq. (3.1).

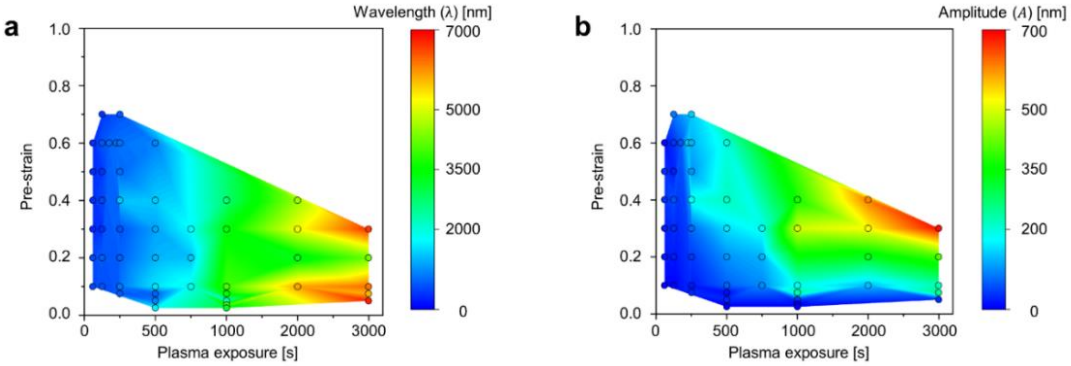

Figure 3.7. The influence of two manufacturing variables, pre-strain and plasma exposure time, on the characteristic dimensions of the produced wrinkles: (a) wavelength (λ) and (b) amplitude (A).

The steepness of the nanowrinkles, characterized by the amplitude to wavelength ratio (A/λ), falls in the range of $4.83 \cdot 10^{-4} < A/\lambda < 0.23$ (Figure 3.8a). The contact angles (with water) of the wrinkled surfaces were measured along the directions parallel and perpendicular to the groove lines, respectively (Figure 3.8b and Figure 3.9a), showing hydrophobicity of the wrinkled surfaces (Figure 3.9b).

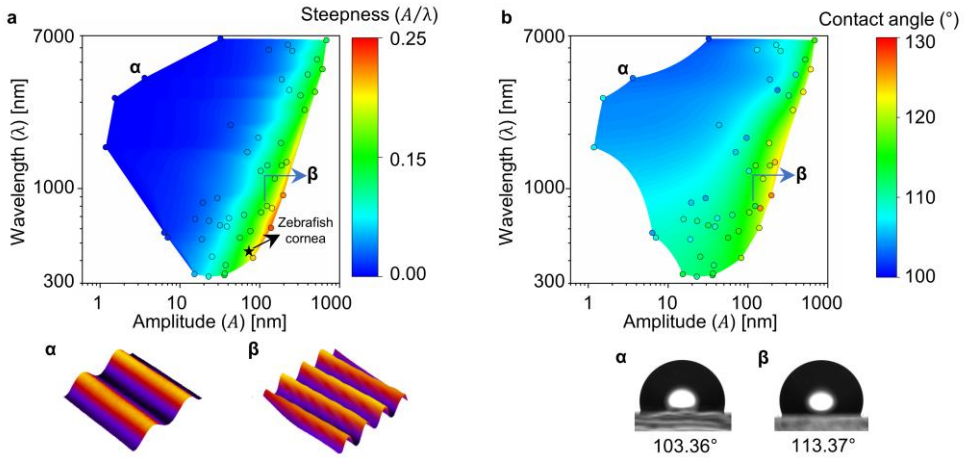

Figure 3.8. (a) The distributions of amplitude (A), wavelength (λ), and steepness (A/λ) of the prepared nanowrinkle. The star symbol indicates the position of the nanowrinkles on the corneal surface of zebrafish ($A = 73.5$ nm, $\lambda_{avg} = 440$ nm). Here, A is calculated from the surface arithmetical mean roughness (R_a) through $A = \frac{\pi}{2} R_a$. The topographies of two representative surfaces (denoted as α and β) measured by AFM are shown with amplitude magnified by 200 and 2 times, respectively, for better visualization. (b) Contact angles of the prepared nanowrinkled surfaces were measured along the direction parallel to the grooves.

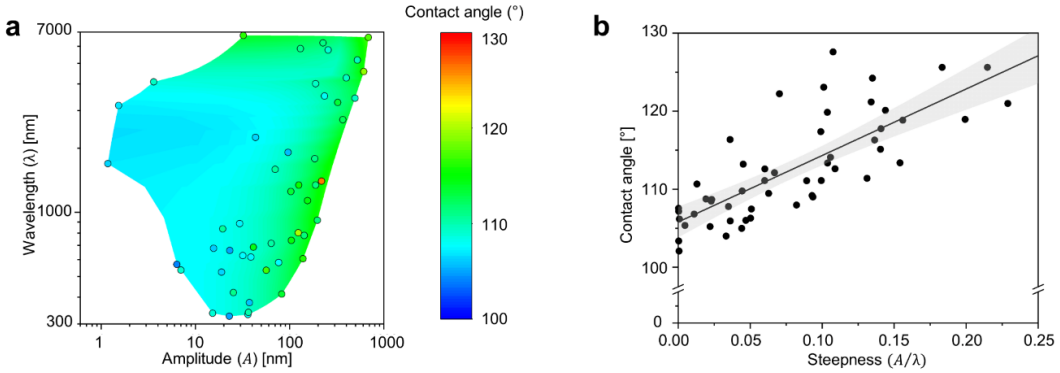

Figure 3.9. (a) Contact angle of wrinkled surfaces measured along the direction perpendicular to the grooves as a function of wavelength (λ) and amplitude (A). (b) The effect of wrinkles' steepness, which is characterized by the ratio of amplitude to wavelength (A/λ), on the contact angle of the surface (measured along the direction parallel to the grooves).

3.3.3 Optical properties of the bioinspired nanowrinkled surfaces

To reveal the dependence of the optical properties, which are characterized by the total transmittance and haze, of the fabricated surfaces on the amplitude and wavelength of the surface nanowrinkles, experimental measurements, and computational simulations were carried out (see Material and Methods). Total transmittance (T_{total}) refers to the ratio of the transmitted light's intensity to the incident light's intensity irrespective of the direction of the light transmitted. Haze (H) is the fraction of the diffused light in the total transmitted light. In practice, any transmitted light that scatters more than 2.5° from the direction predicted through Snell's law is counted as diffused light. For high optical transparency, materials should have not only high total transmittance (*e.g.*, $T_{\text{total}} > 90\%$) but also low haze (*e.g.*, $H < 5\%$). Figure 3.10a and Figure 3.10c show that the amplitude of the wrinkles, compared to their wavelength, plays a more important role in determining the haze of the surface, irrespective underwater or in air. The smaller the amplitude, the lower the haze. For a given wrinkled surface, the haze

underwater is lower than that in air. This is mainly because the refractive index of PDMS (1.35-1.46, Figure 3.3a) is closer to that of seawater (1.34 [144]) than to that of air (1.0 [145]). For the total transmittance, most of the wrinkled surfaces exhibit a value higher than 90% (Figure 3.10b and Figure 3.10d). This is mainly due to the intrinsic high transparency of PDMS material and the small thickness (3 mm) of the samples.

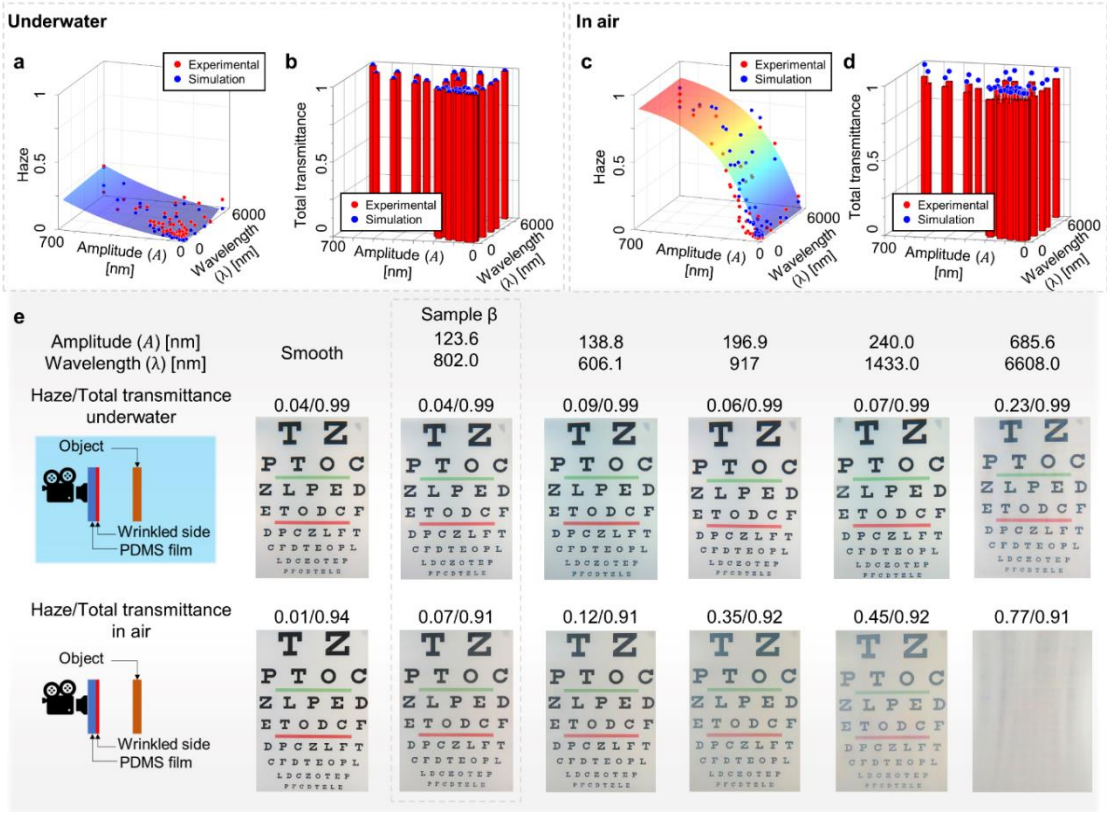

Figure 3.10. Optical properties of the bioinspired nanowrinkled surfaces. Measured and calculated haze and total transmittance (a, b) underwater and (c, d) in air. The continuous surfaces in (a) and (c) are the fitting surfaces of the scattered simulated data. The coefficients of determination (R^2) between the experimental data and the corresponding fitting surface in (a) and (c) are 0.91 and 0.62 respectively, highlighting the capacity of the computational model to predict the experimental results. (e) Digital pictures of a Snellen eye chart taken by a digital camera with the lens covered by different nanowrinkled surfaces underwater and in air.

To examine the visual quality through these wrinkled surfaces, we put the samples in front of a digital camera and took pictures of the same object (a Snellen eye chart) underwater and in air. Figure 3.10e shows the pictures taken in the front of the selected samples. It can be seen that the visual quality becomes worse as the haze of the sample increases even though the total transmittance is kept above 90%. Moreover, for the same sample, the visual quality underwater is better than that in air. This can be attributed to the relatively lower haze of the sample underwater.

3.3.4 Organic fouling resistance of the bioinspired nanowrinkled surfaces

To assess the fouling resistance of the fabricated nanowrinkled surfaces, a laboratory settlement assay was carried out with the bacterium *Pseudoalteromonas* sp., which is a species of marine bacterium often applied in biofouling assessment [146-148]. The dependence of the normalized fouling intensity on the wrinkles' amplitude and wavelength is shown in Figure 3.11a with statistical significance described in Table 3.1. In Figure 3.11a, the fouling intensity is measured by the areal density of the attached bacteria on the tested surface normalized by that on a smooth control (SC) surface without being treated with plasma. It can be seen that surface wrinkles ranging from 600-1000 nm (*e.g.*, sample β) can reduce fouling by 80% as compared to the smooth control. However, surface topography does not always benefit fouling resistance.

Our results show that when the wrinkle wavelength increases to 2 μm and the amplitude exceeds 200 nm (*e.g.*, sample η), the fouling resistance of the wrinkled

surface becomes even worse than that of the smooth control. Since the fouling resistance shown in Figure 3.11a may include the contribution from the plasma treatment, which was found to reduce the contact angle and increase the elastic modulus of PDMS (Figure 3.6), we thereby calculated the topographical contribution through $TC = \frac{(C_{\text{smooth-p}} - C_{\text{wrinkle}})}{C_{\text{smooth-p}}}$, where C_{wrinkle} is the fouling intensity (normalized) of the wrinkled surface (Figure 3.11a), and $C_{\text{smooth-p}}$ the fouling intensity (normalized) of the corresponding smooth PDMS surface treated with the same plasma exposure (Figure 3.12a).

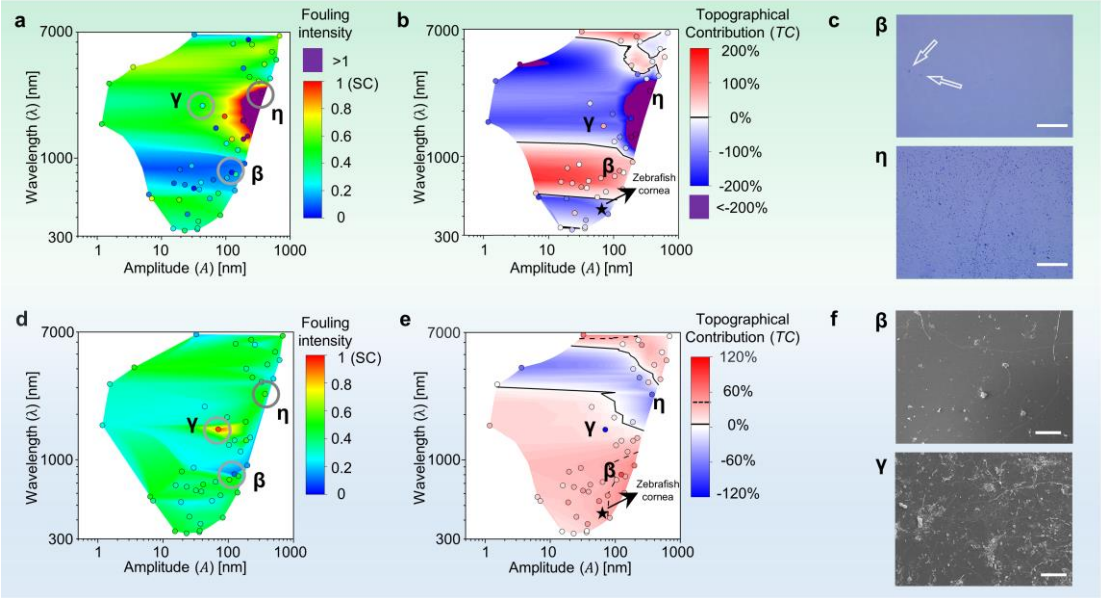

Figure 3.11. Effects of wavelength and amplitude of the surface wrinkles on fouling intensity measured in laboratory assay. Here, fouling intensity is measured by the areal density of the attached bacteria on the tested surfaces normalized by that on the smooth control (SC). (b) The topographical contribution (*TC*) to fouling resistance, where the solid line delineates $TC = 0\%$. (c) Optical microscopy images illustrating the samples with the highest and lowest normalized fouling intensities. (d) Effects of wavelength and amplitude of surface wrinkles on fouling intensity measured in marine field tests. Here, fouling intensity is measured by the fouling percentage cover normalized by the value of the SC. (e) The topographical contribution to fouling resistance, where the solid line delineates $TC = 0\%$ and the dashed line marks the $TC = 40\%$. (f) SEM images of the attachment of marine microorganisms after the field test. Bacterial assay scale bars: 50 μm. Field test scale bars: 200 μm.

Table 3.1. Statistical significance of the laboratory assay results for each sample compared to the smooth control. Notation used: ***, **, *, for alpha levels equal or smaller than 0.01, 0.05, and 0.1, respectively.

Amplitude [nm]	Wavelength [nm]	p-value	Alpha level	Amplitude [nm]	Wavelength [nm]	p-value	Alpha level
138.8	606.1	0.003	***	18.9	524.1	0.235	
82.5	413.8	0.070	*	23.2	662.5	0.003	***
15.2	336.7	0.022	**	41.3	686.0	0.011	**
38.8	616.9	0.007	***	103.0	1252.0	0.014	**
63.8	715.3	0.004	***	124.8	1341.0	0.556	
142.9	779.5	0.008	***	324.1	3269.0	0.355	
123.6	802.0	0.010	***	399.1	4265.0	0.058	*
197.0	917.0	0.006	***	7.0	536.0	0.098	*
36.2	331.9	0.009	***	6.4	570.6	0.005	***
25.3	420.7	0.006	***	19.5	836.8	0.004	***
104.1	738.5	0.006	***	70.2	1588.0	0.010	**
36.5	339.6	0.019	**	96.1	1909.0	0.841	
56.6	534.5	0.005	***	188.5	4011.0	0.008	***
188.6	1342.0	0.565		130.0	5849.0	0.016	**
218.4	1400.0	0.897		225.7	6227.0	0.009	***
366.9	2719.0	0.207		31.9	626.5	0.009	***
612.0	4565.0	0.011	**	15.6	677.8	0.011	**
22.9	325.7	0.013	**	234.8	3508.0	0.016	**
37.5	376.9	0.012	**	256.5	5765.0	0.041	**
76.3	581.5	0.011	**	29.5	885.1	0.004	***
154.7	1134.0	0.007	***	43.5	2245.0	0.009	***
185.2	1786.0	0.665		32.3	6741.0	0.003	***
493.9	3429.0	0.007	***	3.6	4089.0	0.106	
522.9	5168.0	0.037	**	1.2	1690.0	0.048	**
685.7	6608.0	0.120		1.5	3169.0	0.027	**

Based on the calculated TC for all the wrinkled surfaces, we plot the fitted contour of TC as a function of the amplitude and wavelength of the wrinkles (see Figure 3.11b). It can be seen that wrinkles can either enhance ($TC > 0$) or reduce ($TC < 0$) the fouling resistance of the surface, depending on the wavelength and amplitude.

Wrinkles with wavelength below 500 nm were found to reduce the fouling resistance of the concerned surface. Wrinkles with wavelength ranging from 500 nm to 1.1 μm were found to enhance the fouling resistance against *Pseudoalteromonas* sp. Such enhancement seems independent of the amplitude of the wrinkles, at least in the tested range of $3 \text{ nm} < A < 200 \text{ nm}$.

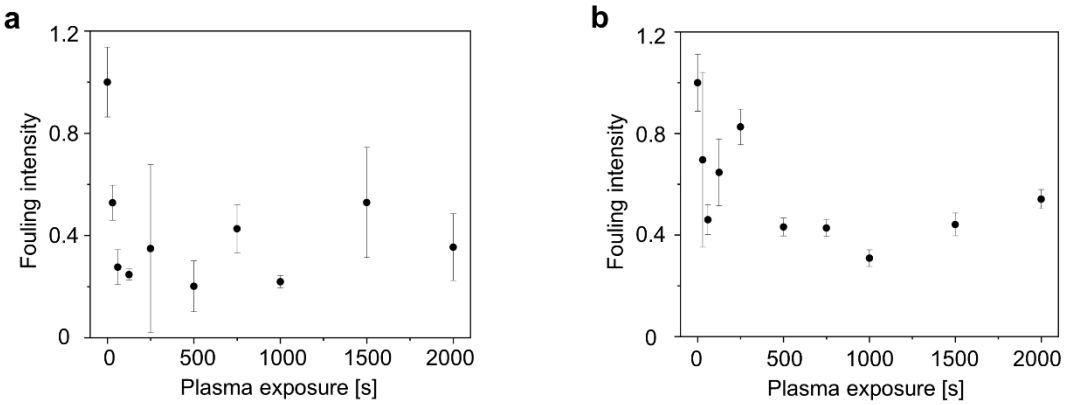

Figure 3.12. Fouling intensity of smooth PDMS surfaces treated with different plasma exposure measured in (a) laboratory assay and (b) field test. Here, the fouling intensity is normalized by the mean value of the smooth control sample without plasma treatment.

In view of the characteristic dimensions of the bacterium *Pseudoalteromonas* sp. (1.27 ± 0.23 μm in width, 1.99 ± 0.34 μm in length), the existence of such optimal wavelength range with superior fouling resistance can be well explained by the least-adhesion-force theory which indicates that surface topography with inter-asperity spacing slightly smaller than the fouler's size gives rise to the least adhesion force with the fouler and therefore best fouling resistance [55]. When the inter-asperity spacing exceeds a threshold, the fouling resistance decreases as the fouler can reach the wrinkle's concave trough, where a higher adhesion force can be achieved [55]. In our case, this situation occurs when the wrinkle wavelength exceeds 1.1 μm especially

when the amplitude A > 200 nm. However, when wavelength exceeds 3 μm, the fouling resistance of the wrinkled surface is getting close to that of a smooth surface with slight fluctuation near the neutral line ($TC = 0$) which might be attributed to experimental error. Optical microscopy images of fouled samples β and η highlight the contrast of fouling resistance between them (Figure 3.11c).

To further assess the fouling resistance of the wrinkled surfaces in the environment with multiple fouling species, a field test was carried out. The fouling intensity on the wrinkled surfaces normalized by that on the smooth control surface is shown in Figure 3.11d with statistical significance in Table 3.2**.** Here, the fouling intensity is measured by the fouling percentage cover on the tested surface normalized by that on a smooth control (SC) surface without being treated with plasma. Among all the tested samples, sample β ($\lambda = 802$ nm, $A = 123.6$ nm) showed the best fouling resistance in the field test with 89% reduction in fouling intensity as compared to the smooth control (p-value < 0.01, see Table 3.2), while the worst sample γ ($\lambda = 1.588$ μm, $A = 70.2$ nm) exhibited only 8% fouling reduction. Similarly, based on the results of the corresponding smooth plasma-treated surfaces (Figure 3.12), the topographical contribution (TC) to the fouling resistance in the field test was calculated and shown in Figure 3.11e. Most of the wrinkled surfaces promoted fouling resistance in the field test, with the best performance exhibited by the sample β ($\lambda = 802$ nm, $A = 123.6$ nm). This is consistent with the results in the laboratory assay above. However, there are wrinkles with $\lambda \approx 3$ μm and $A \approx 200$ nm (*e.g.*, sample η) found to reduce the fouling resistance in the field test. The SEM images of samples β and γ are shown in Figure 3.11f.

To identify the wrinkle which reconciles the conflict between optical transparency and fouling resistance to the best, we integrated the results of optical properties (haze underwater and in air) and fouling intensity in laboratory assay and field test, as shown in Figure 3.13. It can be seen that sample β exhibits the best fouling resistance in both laboratory assay and field test, while its haze is less than 0.04 underwater and 0.07 in air. The optical properties of sample β in the whole visible light spectrum are detailed in Figure 3.14.

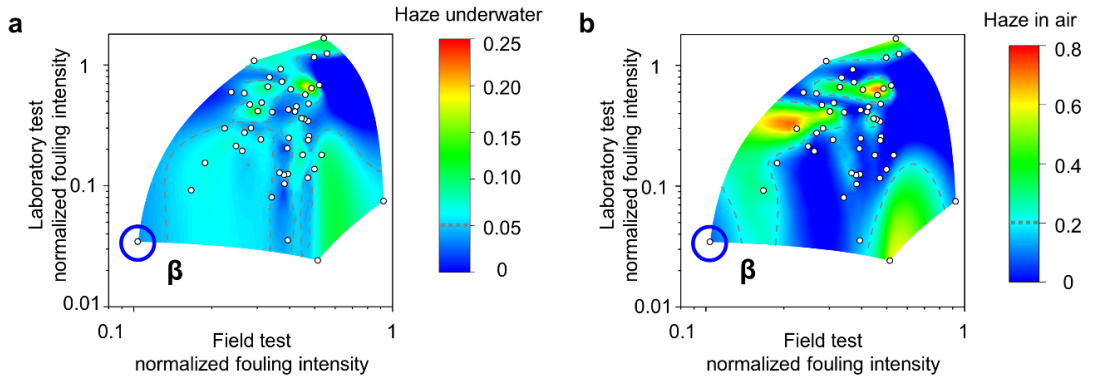

Figure 3.13. (a) Optimization plots show the trade-off between field and laboratory fouling and haze (a) underwater and (b) in air.

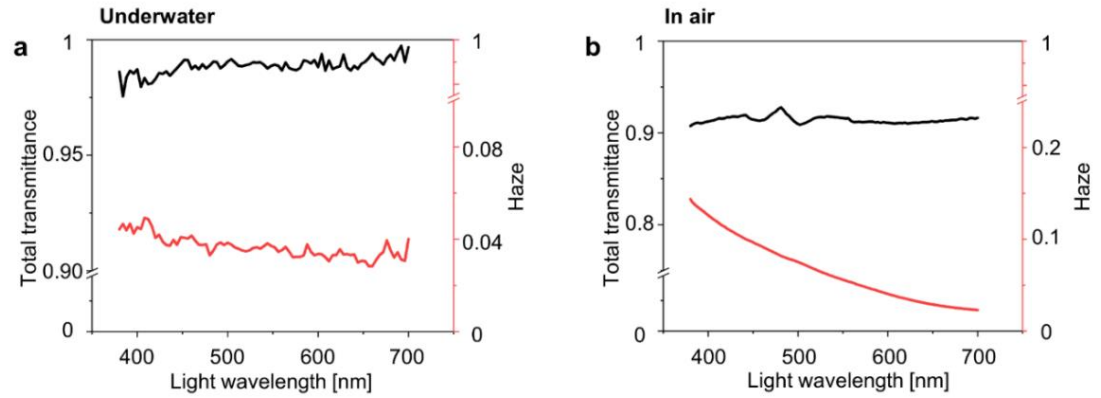

Figure 3.14. Measured optical properties of sample β in the spectrum of visible light. (a) underwater and (b) in air.

Table 3.2. Statistical significance of the field test results for each sample compared to the smooth control. Notation used: ***, **, *, for alpha levels equal or smaller than 0.01, 0.05, and 0.1, respectively.

Amplitude [nm]	Wavelength [nm]	p-value	Alpha level	Amplitude [nm]	Wavelength [nm]	p-value	Alpha level
138.8	606.1	0.003	***	18.9	524.1	0.001	***
82.5	413.8	0.005	***	23.2	662.5	0.016	**
15.2	336.7	0.005	***	41.3	686.0	0.004	***
38.8	616.9	0.008	***	103.0	1252.0	0.003	***
63.8	715.3	0.002	***	124.8	1341.0	0.004	***
142.9	779.5	0.004	***	324.1	3269.0	0.003	***
123.6	802.0	0.003	***	399.1	4265.0	0.005	***
197.0	917.0	0.002	***	7.0	536.0	0.005	***
36.2	331.9	0.003	***	6.4	570.6	0.009	***
25.3	420.7	0.006	***	19.5	836.8	0.006	***
104.1	738.5	0.012	**	70.2	1588.0	0.378	
36.5	339.6	0.004	***	96.1	1909.0	0.002	***
56.6	534.5	0.001	***	188.5	4011.0	0.014	**
188.6	1342.0	0.009	***	130.0	5849.0	0.003	***
218.4	1400.0	0.002	***	225.7	6227.0	0.053	*
366.9	2719.0	0.008	***	31.9	626.5	0.005	***
612.0	4565.0	0.002	***	15.6	677.8	0.002	***
22.9	325.7	0.005	***	234.8	3508.0	0.004	***
37.5	376.9	0.002	***	256.5	5765.0	0.002	***
76.3	581.5	0.004	***	29.5	885.1	0.005	***
154.7	1134.0	0.001	***	43.5	2245.0	0.001	***
185.2	1786.0	0.009	***	32.3	6741.0	0.006	***
493.9	3429.0	0.001	***	3.6	4089.0	0.023	**
522.9	5168.0	0.106		1.2	1690.0	0.004	***
685.7	6608.0	0.004	***	1.5	3169.0	0.002	***

3.3.5 Inorganic fouling resistance of the bioinspired nanowrinkled surfaces

In addition to the fouling resistance against organic molecules and bacteria, our transparent nanowrinkled surfaces also exhibit superior resistance against the attachment of the inorganic particles (Figure 3.15). For example, it is much easier to remove the cement powder on sample β by dropping water or mechanical shaking (Figure 3.15b and Figure 3.15c) as compared to the smooth control (see Figure 3.16 for the surface topographical data), implying the great application potential as the shield for solar panels in the desert. After removing the cement particles by mechanical shaking, sample β exhibits a better transparency ($T_{\text{total}} = 87\%, H = 9\%$) in comparison to the smooth control ($T_{\text{total}} = 56\%,\ H = 46\%$) (Figure 3.17). If rinsed with water drops, the optical transparency of sample β can be recovered fully, while that of the smooth surface cannot be (Figure 3.17).

Moreover, in addition to planar surfaces, nanowrinkles can also be produced on curved surfaces by using a similar pre-straining technique, implying the great application promise of our transparent fouling-resistant surfaces in contact lenses (Figure 3.15d) [149, 150]. For this application, the optimal wrinkle (sample β) we found above may not apply since the micro protrusions on the human cornea, if they are also for resisting biofouling, exhibit similar amplitude (mean height ~129 nm [151]) but much shorter wavelength ($\lambda = 47$ nm) [135]. As the optimal wrinkle dimensions depend on the sizes of the potential bacteria, further investigation is needed to determine the best surface wrinkles for contact lenses.

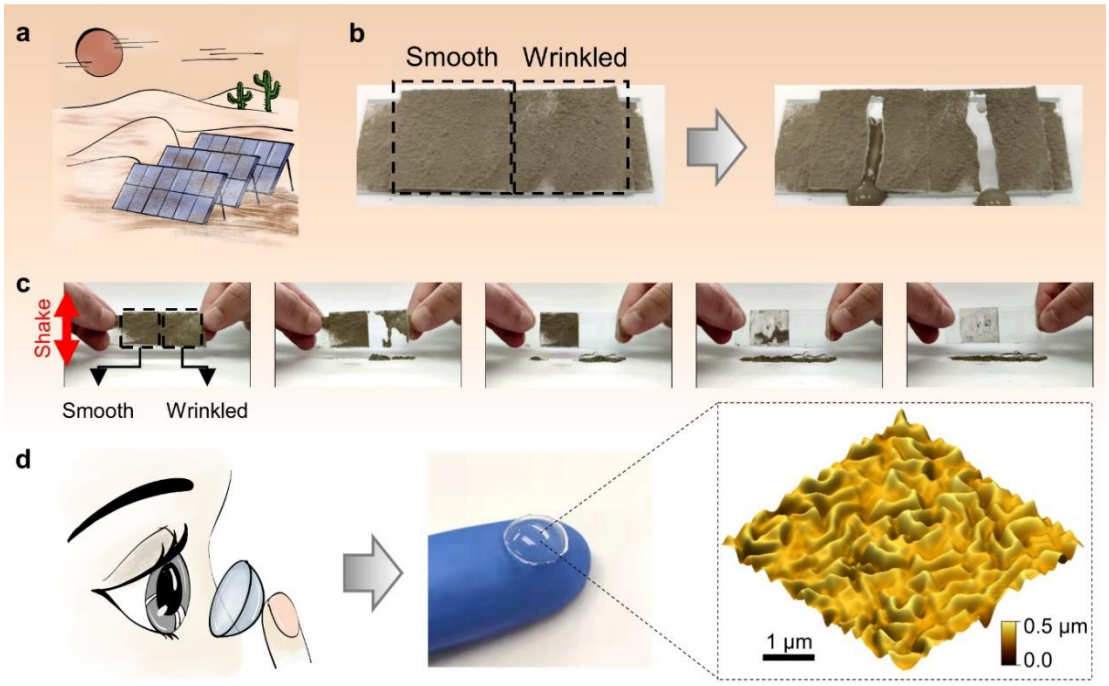

Figure 3.15. (a) Schematic illustration showing the dust-covered solar panels in a desertic environment. (b) Demonstration of the self-cleaning property of the bioinspired nanowrinkled surfaces upon (b) water dropping and (c) mechanical shaking. (d) A curved membrane with nanowrinkled surface implies great application promise in contact lenses. The amplitude in the AFM topography is exaggerated by 30 times for better visualization.

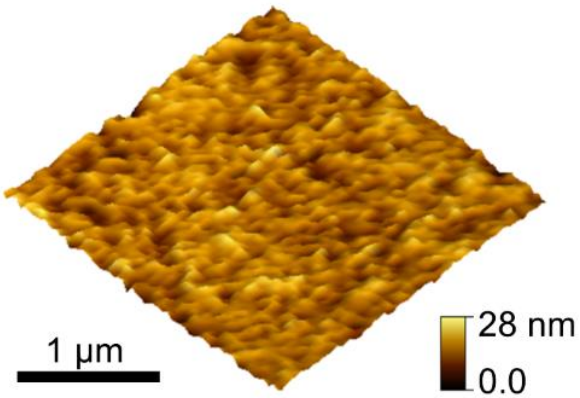

Figure 3.16. Surface topography of the smooth control sample measured by AFM. The arithmetic average roughness is calculated to be $R_a = 2.63$ nm. Here, the height is exaggerated by 5 times for better visualization.

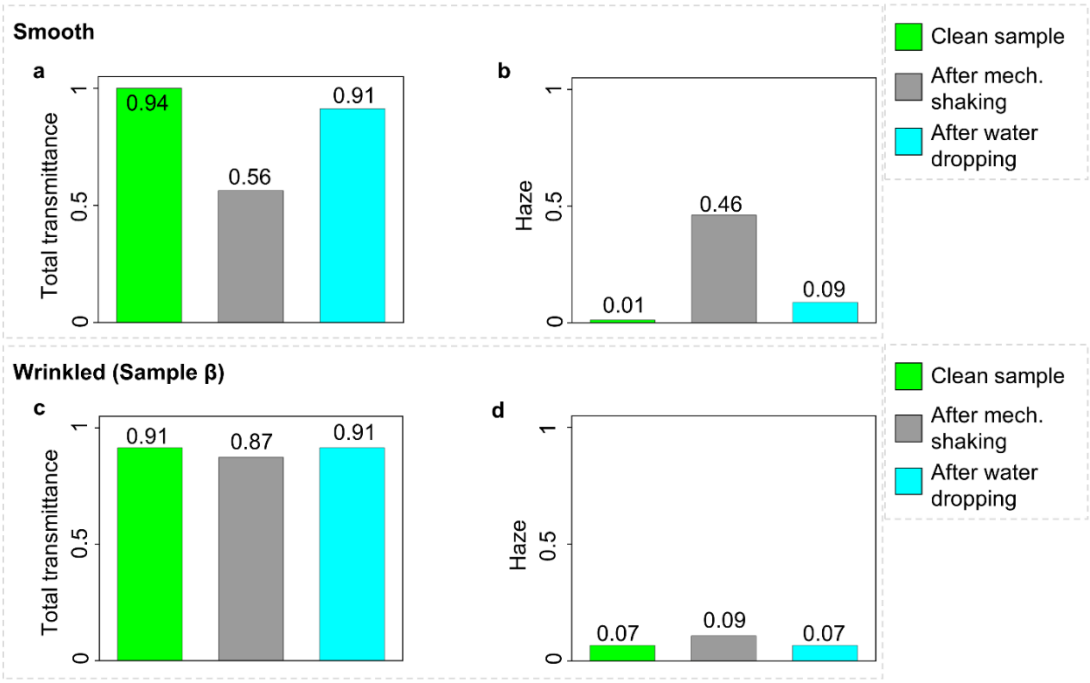

Figure 3.17. Total transmittance and haze of (a, b) smooth and (c, d) wrinkled samples at three different states: (1) clean (uncontaminated), (2) contaminated by cement powder and then cleaned by mechanical shaking, (3) contaminated by cement powder and then rinsed by water drops.

3.4 Summary

Inspired by the surface topography on the cornea of zebrafish, we synthesized polymeric films with controllable surface nanowrinkles by taking advantage of the buckling phenomenon of stiffer coating on a soft foundation under compression. By investigating the effect of the wrinkles' size on the haze and total transmittance of the film, which are two indexes characterizing optical transparency, we found that the wrinkle amplitude plays the dominant role in determining the optical transparency of the film. In particular, our results showed that wrinkles with amplitude ~300 nm or less can achieve satisfactory optical transparency (haze < 10% and total transmittance >90%). On the other hand, the fouling resistance of the films depends more on the wrinkle wavelength than on the amplitude. Our results showed that wrinkles with a

wavelength around 800 nm exhibit the best fouling resistance in both laboratory assay with a bacterium and field tests in the ocean with multiple fouling species. It is essential to highlight that the optimal wrinkle dimensions may vary if different foulers' sizes are considered. In addition, the optimal wrinkled surface with $\lambda \approx 800$ nm, $A \approx 100$ nm was found resistant to the attachment of inorganic particles as well. Our results provide a non-chemical solution to reconciling the conflict between optical transparency and fouling resistance and are of great value to the design of shields for optical instruments working in extreme environments such as solar panels in the desert and deep-sea cameras. Moreover, the fabrication methodology (*e.g.*, plasma exposure and pre-strain) can be easily adapted to obtain wrinkles with different dimensions to focus on an antifouling performance against a specific fouler while using the current optical properties' results to predict surface transparency.

Chapter 4 Large-scale cost-effective solutions to marine biofouling and insights on double strategies for antifouling control

4.1 Introduction

Antifouling topographies tend to be fabricated using polymeric materials. These materials facilitate the fabrication of designed surfaces and have inherently lower elastic modulus, improving antifouling performance [152]. On the other hand, they have inadequate durability compared to stronger materials such as metals. Fabrication of metallic surfaces with features adequate to avoid fouling proliferation requires complex manufacturing methods [128]. Moreover, mass production is a massive challenge due to slow-manufacturing speeds and extremely high costs. New routes have been proposed but are either highly complex or unable to fabricate large-scale surfaces. For instance, nickel-based hierarchical structures showed great antifouling performance during field tests, but they require a multi-step fabrication that involves molding, laser interference lithography, and electroforming [153]; through complex electrochemical deposition of nanoporous tungstite films on steel, a metallic surface was able to reduce marine algae adhesion [154]. The first case study presented in this Chapter presents a new facile method to fabricate large-scale antifouling metallic surfaces with micrometer-sized features. The method is explained in detail, and the obtained surfaces are evaluated against fouling in a marine field test and a barnacle laboratory assay. The influence of the surface features dimensions on the antifouling performance is shown. Fabrication costs and the scale-up possibility are discussed.

Surface topography and the usage of natural products antifoulants (NPAs) are known strategies against biofouling [21, 55, 128, 155], and it is suggested that natural

materials do combine both strategies [156]. The addition of NPA to a modified PDMS compound in a nanotextured surface showed promising antifouling results [157]. However, the coating preparation is extremely complicated to expand to a large-scale, and the antifouling performance was only evaluated in a laboratory bacterium assay. In the second case study, an NPA is incorporated into the paint, aiming to better understand the combination of chemical and topographical strategies, using a similar fabrication methodology to the first case study. The selected NPA was camptothecin. This NPA is known for its high antifouling capacity and low environmental risk [158]. The samples' antifouling performances are assessed by field test and discussed.

4.2 Materials and methods

4.2.1 Fabrication of samples

Fabrication starts by positioning the mesh on top of a substrate. According to their dimensions, the meshes are denominated by their commercial names (Table 4.1). A lower denomination number (e.g., M100) means larger fiber diameter and lateral spacing. The substrate and meshes are both made of stainless steel 304 except for M400 and M500, made by SS316. Following, a layer of paint covers the surfaces (Figure 4.2). The coating functions as a glue to guarantee the adhesion of the meshed fibers to the substrate while being a coating to fibers reducing their outer elastic modulus. In case study 1, the paint is aluminum-based and does not contain any NPA. The control samples, SNP and SP, are used for comparison. For case study 2, paints with and without NPA were used. The paint components are described in Table 4.2. The first fabrication step is to mix xylene, rosin, and organic bentonite at 2000 rpm for

20 min. Then, the VC-Copolymer is added and mix for another 10 min at the same speed. The third step is to add titanium oxide (TiO_2), zinc oxide (ZnO), and calcium carbonate ($CaCO_3$) with 100-150g of glass beads. For the paint with NPA, the NPA is added in this step. After mixing for 2 h at 1400 rpm, the paint is filtered to remove the glass beads and stored in a container. Besides the samples SNP and SP, another control was introduced: smooth-painted with NPA (SP+NPA). To evaluate the inclusion of NPA in meshed samples, three meshed configurations were coated without NPA: M20, M300, and M500.

Table 4.1. Characteristics of the metallic specimens: dimensions and materials.

Denomination	**Material**	**Fiber diameter [µm]**	**Lateral spacing [µm]**
Smooth Not-Painted (SNP)	SS 304	-	-
Smooth Painted (SP)	SS 304	-	-
Mesh 20	SS 304	270	1270
Mesh 50	SS 304	150	500
Mesh 100	SS 304	100	250
Mesh 150	SS 304	63	173
Mesh 300	SS 304	40	84
Mesh 325	SS 304	35	78
Mesh 350	SS 304	30	72
Mesh 400	SS 316	30	63
Mesh 500	SS 316	25	50

4.2.2 Biofouling marine field test

The field test was carried out for twelve weeks at the Hebe Haven Yacht Club, Sai Kung, Hong Kong (22°21'53.0"N 114°15'34.4"E). To avoid corrosion, the metallic samples (two for each specimen) were fixed in a polymeric structure with polymeric fixators. The structure was tied to a pier and submerged by *circa* two meters of seawater. The pier is highly prone to biofouling due to the presence of natural waste released by anchored yachts. Fouling was assessed at weeks 1, 2, 3, and 12. The fouling

did not fully cover the metallic samples in the short term (weeks 1, 2, 3). Thus, for the first case study, measurements were made by acquiring photographs of the surfaces (under controlled light) and processed with a clustering algorithm to identify biofouling. The methodology is illustrated in Figure 4.1b. The K-mean cluster algorithm divides the initial photograph into several clusters, 6 in our case, based on color and brightness. We then identify the cluster that well segmented the fouling coverage from the background substrate. With the aid of the software ImageJ, the image has its colors inverted, and the percentage of black pixels over the total area measured, which represents the biofouling coverage.

Table 4.2. Paints compositions in the case study 2, weight calculated to obtain a final 500 grams of paint with or without NPA.

Compound description	**Weight to fabricate the paint with NPA (g)**	**Weight to fabricate the paint without NPA (g)**
Xylene	150	174.4
Rosin	60	69
Organic bentonite	5	5.8
VC-Copolymer	65	75.5
TiO_2	40	46.5
ZnO	60	69
$CaCO_3$	50	58
NPA: Camptothecin	70	-

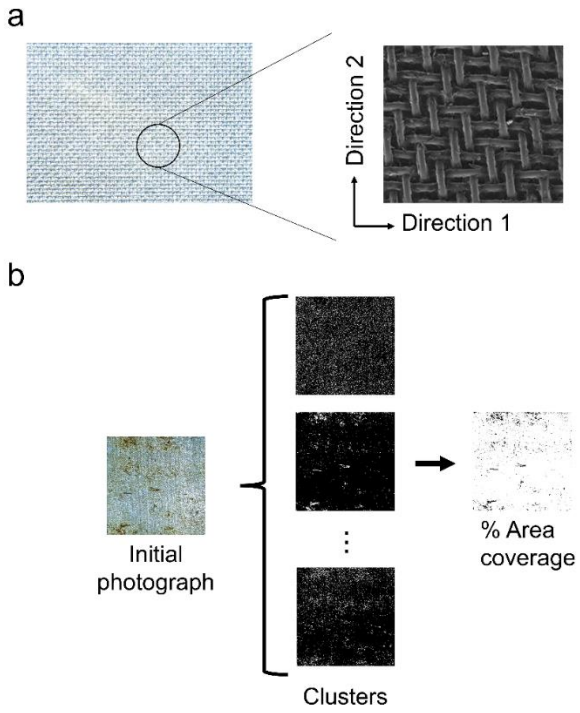

Figure 4.1. (a) Example of a final surface. Top view showing directions 1 and 2. (b). Clustering algorithm adopted: k-mean. It segments the initial image into clusters, like the observed fouling coverage without the background surface. Then, the percentage of area coverage is assessed by measuring the proportion of black pixels over the total image size.

4.2.3 Barnacle laboratory assay

The case study 1 was also assessed by a barnacle laboratory assay. Barnacles (*Balanus amphitrite*) were collected from mangroves stems at Ha Pak Nai, Hong Kong (22°26'20.4"N 113°56'55.5"E). Their attachment to stems facilitated their extraction without damaging the animals, which often occurs when collected from rocks with scraping. Adult organisms were transported in the air to our laboratory and placed in filtered seawater (100 µL). Within hours, phototactic nauplii were released, attracted to a light source, and sieved into another container. Culture tanks were kept at 20°C with aerated seawater (0.22 µL). Larvae were fed daily with diatom *Chaetoceros gracilis*, maintaining a quasi-steady concentration of $1.02 \cdot 10^6$ mL^{-1}. After four days,

cyprids were developed. Before the attachment test, they were aged in a dark environment at 6°C. Finally, each studied surface was fit in a petri dish (polystyrene, 100mm diameter), and 35 mL of filtered seawater and 25 cyprids were added. After 48h under similar laboratory conditions to the tubeworms test, attached cyprids were counted after light touching to confirm their adhesion with the aid of an optical microscope.

4.3 Results and discussions

4.3.1 Surface fabrication and characterization

Contact-based mechanics highlight the influence of surface topography on the pull-off force of a fouler, as discussed in Chapter 1. Inspired by it, a fabrication route is proposed to obtain large-scale, cost-effective metallic antifouling surfaces. First, meshed metallic fibers are positioned on top of a smooth metallic substrate, creating a ridge-like topography (Figure 4.2a). Towards easy reproducibility, only commercially available materials are used, and both the substrate and mesh are made of stainless steel. By varying the mesh dimensions (fiber diameter and lateral spacing), the influence of scale on antifouling can be monitored. Second, a coating is applied to serve as the bonding agent between the fibers and the substrate. In the first case study, the selected coating is waterproof and aluminum-based to enhance its durability. The second case study proposes a coating with and without an NPA. The proposed fabrication method can be applied to create antifouling surfaces on flat and curved substrates (Figure 4.2b), emphasizing their application capabilities on curved naval structured such as boat hulls. For case study 1, the fabricated samples were compared

to two controls: smooth non-painted (SNP) and smooth painted (SP). SP and SNP represent only the metallic substrate with and without the paint, respectively. For case study 2, an additional control was included: smooth-painted with NPA (SP+NPA).

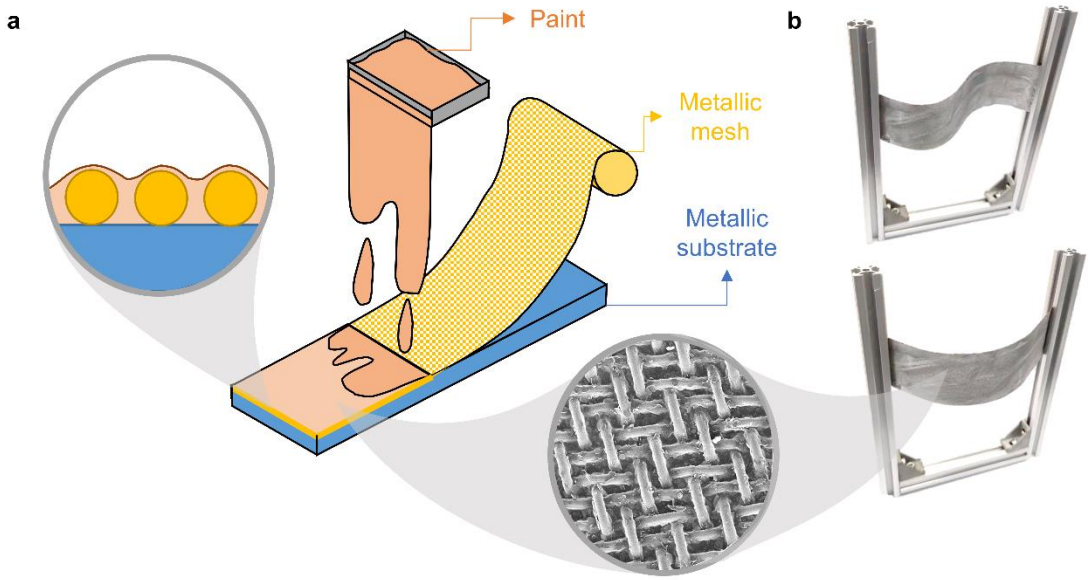

Figure 4.2. (a) Fabrication schematics showing the multi-constituents and electron microscopy of an obtained surface, which can be mounted on (b) curved substrates.

4.3.2 Antifouling performance of proposed surfaces

In the first case study, two biofouling tests were performed to test the proposed surfaces' antifouling capacity. Initially, the specimens were submitted to a barnacle attachment test under laboratory conditions. Comparing the control samples, the results showed a 32% fouling decrease due to the coating of a smooth sample (Figure 4.3a). The smooth painted control (SP) still had more organisms attached than any meshed surface. Normalizing by the M100, all ridged surfaces reduced at least 65% of attachment compared to the SNP and 48% to the SP. By decreasing the dimensions of the fibers, the trend described a further decrease in barnacle adhesion. The best result is for Mesh 400, with 91% less barnacle attachment density than the control SNP. Predictive

statistical models (see Chapter 2) demonstrated good agreement using the experimental results for the bioinspired surfaces but not for the smooth surface. The applied model was developed based on meta-analysis, where results from multiple groups are combined and input into multiple regression analysis. Thus, the slight discrepancy shows that the model can still be improved, as expected for a meta-analysis study.

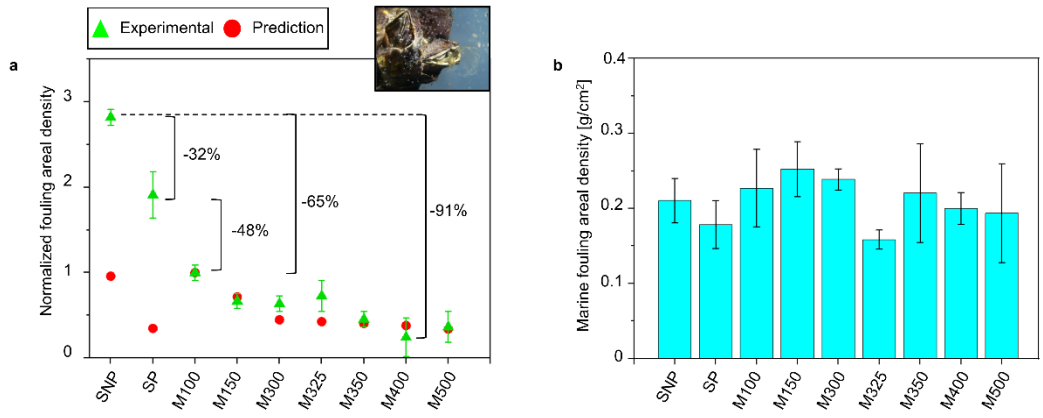

Figure 4.3. Biofouling assessment results. (a) Barnacle attachment assay. (b) Long-term field tests.

A laboratory assay determines the antifouling performance of specimens against single fouler species but does not consider complex foulers' interactions that naturally occur in real-world conditions. In this direction, the metallic surfaces are evaluated in a static oceanic submersion test by measuring the fouling coverage area after 1, 2, 3, and 12 weeks (Figure 4.4b and Figure 4.3b). After one week, a slight variance between the samples is seen. After two weeks, surfaces M300, M325, M350, and M400 had the lowest fouling, reconfirmed after the third week. These samples are made with fibers diameters from 30 µm to 40 µm and lateral spacing from 63 µm to 84 µm. Sample M325 showed a fouling coverage decrease of up to 78% compared to the SNP. A continuous reduction in the topographies dimensions does not necessarily mean less

biofouling. The sample M500, with the smallest dimensions (fibers diameter and spacing), had biofouling coverage comparable to the SP control for all time frames. This result suggests that biofilm and microfouling formation could cover the meshed fibers' topography, reducing the ridges' capacity to reduce biofoulers adhesion force. In addition, during real-life conditions, there are interactions between foulers, substrate, and inorganic particles, which can or not benefit their adhesion [159]. To evaluate long-term antifouling performance, the same samples were submerged for 12 weeks. After the period, all samples were fully covered by biofouling, and the fouling coverage area was not a reasonable method to evaluate the surfaces; thus, the biofouling weight per area was measured. Despite the lower value for M325, the results show no statistical difference between the samples and the controls (Figure 4.3b). It suggests that biofouling builds up on top of the surfaces' morphologies in the long term, transforming the topography to an apparent smooth topography over time.

Comparing the smooth controls, the surface without coating (SNP) showed the highest fouling coverage (Figure 4.4c), as expected. The smooth sample with NPA (SP+NPA) had 88% less fouling than the one without NPA (SP). The addition of NPA in meshed surfaces is observable but less significant. The sample M300 showed 4.4% more fouling than the M300+NPA. Meanwhile, the lack of NPA for M20 and M500 was 10.6% and 19.6%, respectively. These results show that the NPA contribution is higher for smooth samples and much lower for meshed surfaces. The seawater flow behavior directly influences the release of NPA. Samples with rougher surfaces tend to disturb more the flow rate, creating zones that might facilitate the removal of NPA from the layer close to the surface, reducing its antifouling performance. This is a hypothesis and should yet be validated.

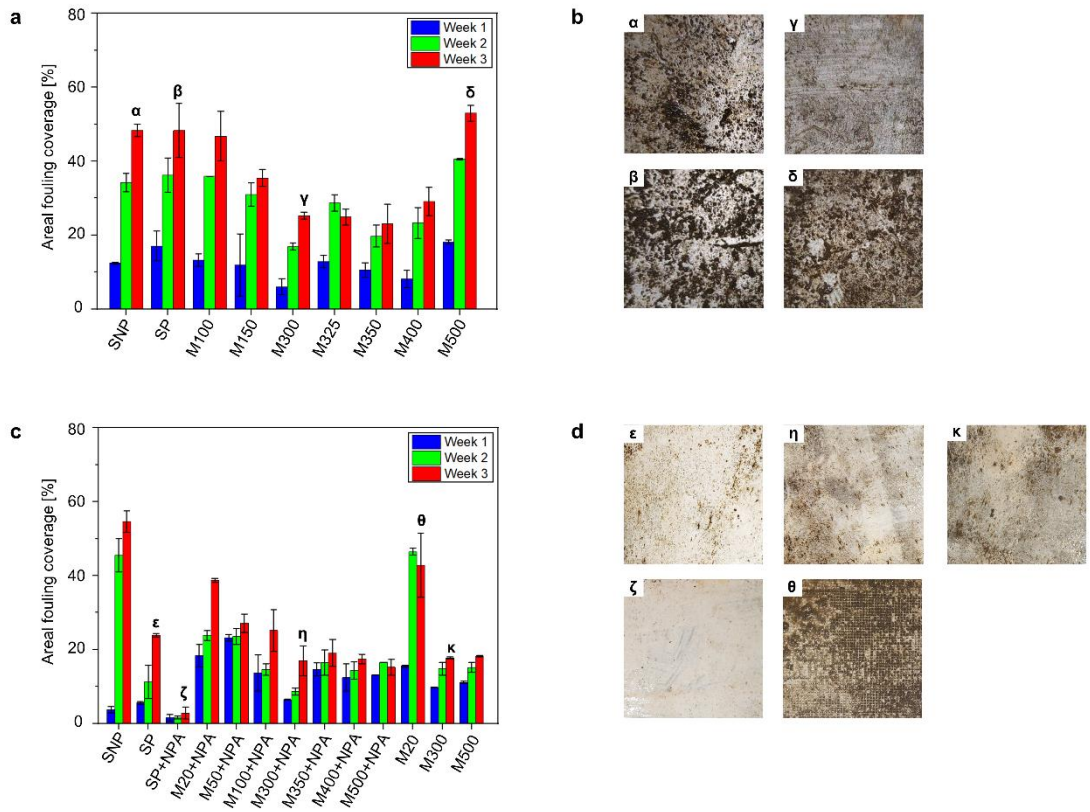

Figure 4.4. Short-term field test for (b, c) case study 1 and (c, d) case study 2. (a, c) Measured areal fouling coverage. (b, d) Examples of samples.

Comparing the meshed samples with NPA shows a similar trend to case study 1, where surfaces M300 to M400 showed the lowest fouling coverage. The exception was M500. In case study 1, the observed trend highlighted an increase in fouling for M500 compared to M300, for example. However, in case study 2, both surfaces have similar performance. An additional study to understand the influence of surface roughness to NPA release might be needed.

4.3.3 Fabrication cost analysis

Metallic antifouling surfaces tend to have extremely high fabrication costs due to the use of complex methods to obtain microstructured features. Here, the costs of the

proposed method are assed. They are divided into equipment costs, including any specific machine necessary to fabricate the surface, and material costs, including materials used during the method. The proposed method's costs for the first square meter and the tenth, or any future manufacturing cycle, are always the same. Plus, equipment costs are zero: there is no need for a specific machine for manufacturing, and the material costs enclose the mesh and the coating. Per square meter, the method costs USD 10.60, USD 2.44 for the coating, and USD 8.16 for the meshed fibers. The latter has different costs based on its dimensions (Table 4.3).

Table 4.3. Description of the costs for the commercial mesh and the total average.

Mesh denomination	**Costs per m^2 (USD)**
20	4.05
50	4.50
100	4.72
150	4.87
300	7.50
325	8.25
350	9.00
400	13.50
500	19.50
Average	8.16

4.4 Summary

Surface topography can reduce fouling colonization by decreasing the contact force between fouler and surface. To be effective, the topographical features require dimensions as small as the foulers' larvae. Manufacturing micrometer-sized structures pose an incredible challenge, which is enhanced if there is the need for large-scale and low costs. Current techniques capable of addressing this problem utilize polymeric

materials. However, these are not durable when subjected to mechanical stresses found in marine structures. Using the intrinsic properties of metallic materials, capable of withstanding long-term stresses, this Chapter suggests a facile route to fabricate metallic-based surfaces to reduce marine biofouling. The results evidence the success of fabricating large-scale, cost-effective metallic antifouling surfaces, currently greatly needed in the naval industry. Moreover, the optimal mesh is proposed based on field tests and laboratory assays. In addition, the influence of NPA is discussed, and the results presented that NPA has a lower efficacy on meshed surfaces than on smooth samples.

Chapter 5 Conclusions and future work

This thesis systematically studied biomimetic surface engineering to biofouling control through data analysis, computational models and experimental assays, and can be translated into guidelines and strategies. These are pointed out in this chapter, including suggestions for future works.

5.1 Conclusions

Biofouling control can be obtained through many methods. However, as it is a complex biological process that can be affected by various factors such as environmental parameters, surface topography, and fouler dimensions, there is still a lack of analytical models covering all the multidisciplinary factors. One of the most recent studied antifouling methods is surface topography, which can reduce the fouler contact force to the substrate. This methodology has many open questions, such as what the influence of surface topography to is a material optical property, or how to fabricate large-scaled surfaces with micrometer-sized features. Here, these topics have been addressed, and the major conclusions are summarized below:

- We carried out a meta-analysis to understand the effect of ten factors on the attachment efficiency of marine foulers. These factors comprehend multidisciplinary variables such as water flow rate, surface morphology and stiffness, and fouler species. Despite being individually studied by recent research, there is no universal rule to predict the attachment of a fouler. In Chapter 3, using a combination of Buckingham theorem and multilinear regression, a universal correlation to predict attachment efficiency of foulers

onto surfaces is proposed. The model is validated by tubeworms' attachment tests on PDMS surfaces. These findings are of great importance in understanding the factors that affect biofouling and are of great value in designing new antifouling surfaces.

- To understand the influence of changing the surface topography to the optical properties and antifouling performance of PDMS membranes, we synthesized many PDMS films with controlled surface nanowrinkles. The design is inspired by the zebrafish external corneal topography, which highlights an abundance of nanowrinkles with an average amplitude of 73.5 nm and wavelength of 440 nm. The bioinspired wrinkles are obtained by taking advantage of the buckling , due to compression, of a stiffer layer onto a softer substrate. Computational and experimental results show that the wrinkles' amplitude plays a more important role than the wrinkles' wavelength in the membranes' optical properties. Specifically, nanowrinkles with an amplitude below 300 nm have remarkably similar transparency to the smooth PDMS membrane. Unlike the optical properties, membranes' antifouling performance is more dependent on the wrinkles' wavelength. In Chapter 4, it is shown that the wrinkles with wavelength and amplitude around 800 nm and 100 nm, respectively, have optimal resistance against fouling and excellent optical properties. Moreover, results evidence that nanowrinkles may also promote fouling instead of repealing. The same methodology is applied to obtain wrinkling on curved surfaces, demonstrating the possibility of further applications such as contact lenses and other optical systems.
- The fabrication of large-scaled metallic surfaces with antifouling topographies

is extremely challenging due to manufacturing costs. However, many real-life applications require the usage of strong materials, such as metals, and large-scale coverage, such as commercial boat hulls. In Chapter 4, a facile method to fabricate a large-scale, cost-effective solution aimed at avoiding marine fouling is proposed and evaluated. For case study 1, results evidenced the surfaces' antifouling ability to reduce fouling colonization for up to 3 weeks. Nevertheless, the long-term assay showed that the proposed surfaces do not have long-term antifouling capacity. For case study 2, including natural antifouling products (NPA) enhanced the surfaces' antifouling performance, especially for smooth control. The NPA also reduced the fouling coverage for the meshed surfaces but was below expectations.

5.2 Outlook to future work

5.2.1 *De novo* meta-analysis

Data analysis, such as regressions and machine learning, have been widely spread to many fields, but it is still moving slowly in the biofouling community [160]. Literature is constantly being updated, and with the biofouling community, it is not different. The meta-analysis described in Chapter 2 was published in 2019, and to our knowledge, up until now, there has not been a similar study published. In this direction, a *de novo* meta-analysis could be performed. A suggestion is to also consider bacterial fouling, to enlarge the data-driven analysis input, and other factors.

5.2.2 Wrinkling morphologies

In Chapter 3, PDMS unidirectional wrinkling was proposed as a method to fabricate wrinkled topographies that resembled the fisheye topography. However, the obtained wrinkles are aligned and not randomly orientated like those found in the fisheye. In a future study, it is suggested to attempt fabricating wrinkles using bidirectional pre-strain. Literature highlights that for bidirectional straining, another factor plays an important role: the order of strain release [161]. The latter can influence the wrinkle pattern formation from ripple with bifurcation, to a mix of ripple and herringbone to fully ordered herringbone topography. From a similar point of view, hierarchical wrinkling, where there is more than one apparent wrinkling wavelength, could be performed. The fabrication required an extra step like the one proposed in Chapter 3. The nanowrinkled surfaces presented in this thesis have a top layer with different properties from the base PDMS substrate. This layer cannot be easily altered using plasma treatment. Thus, using a mold of the first wrinkled surface, a second plasma treatment can be applied to reintroduce the bending instability and create a second-order wrinkling. Nevertheless, the influence of these surfaces on the optical properties and antifouling performance is yet to be studied.

5.2.3 Plasma-treated surface properties

Plasma treatment of PDMS is known to modify the material affected region, creating a glass-like layer with increased mechanical properties and other characteristics different than the untreated PDMS. Nevertheless, there are many contradictions regarding the thickness of the affected layer and the mechanical properties, especially

the elastic modulus [143, 162-164]. A deep experimental analysis is suggested, using transmission electron microscopy and atomic force microscopy to enhance the literature.

5.2.4 Combination of chemical and topographical strategies

Chapter 4 described a study to evaluate the combination of NPA with meshed surfaces. The effect of NPA on non-smooth surfaces was significantly lower than the effect on smooth surfaces. This conflict highlighted that the fouling behavior is still far from fully understood. Additional studies are needed to expand the knowledge on how chemical strategies may have reduced efficacy on surfaces with topographical antifouling features.

References

1. M.L. Hakim, B. Nugroho, M.N. Nurrohman, I.K. Suastika, I.K.A.P. Utama, 2019. Investigation of fuel consumption on an operating ship due to biofouling growth and quality of anti-fouling coating, IOP Conf. Ser. Earth Environ. Sci. 339, 012037.
2. M.P. Schultz, J.A. Bendick, E.R. Holm, W.M. Hertel, 2011. Economic impact of biofouling on a naval surface ship, Biofouling 27(1), 87-98.
3. B. Bharti, J. Meissner, S.H.L. Klapp, G.H. Findenegg, 2014. Bridging interactions of proteins with silica nanoparticles: The influence of pH, ionic strength and protein concentration, Soft Matter 10(5), 718-728.
4. J. Meissner, A. Prause, B. Bharti, G.H. Findenegg, 2015. Characterization of protein adsorption onto silica nanoparticles: influence of pH and ionic strength, Colloid Polym. Sci. 293(11), 3381-3391.
5. M. Hermansson, 1999. The DLVO theory in microbial adhesion, Colloids Surf. B 14(1), 105-119.
6. L.D. Renner, D.B. Weibel, 2011. Physicochemical regulation of biofilm formation, MRS Bull. 36(5), 347-355.
7. I.W. Sutherland, 2001. Microbial polysaccharides from Gram-negative bacteria, Int. Dairy J. 11(9), 663-674.
8. H. Flemming. Why microorganisms live in biofilms and the problem of biofouling. Marine and Industrial Biofouling. Berlin: Springer; 2008. p. 3-12.
9. M.T. Davis, P.F. Newell, N.J. Quinn, 1999. TBT contamination of an artisanal subsistence fishery in Suva harbour, Fiji, Ocean Coast. Manag. 42(6), 591-601.
10. M.M. Santos, C.C. Ten Hallers-Tjabbes, A.M. Santos, N. Vieira, 2002. Imposex in Nucella lapillus, a bioindicator for TBT contamination: re-survey along the Portuguese coast to monitor the effectiveness of EU regulation, J. Sea Res. 48(3), 217-223.
11. J.G. Wilson, D. Minchin, B. McHugh, E. McGovern, C.J. Tanner, M. Giltrap, 2015. Declines in TBT contamination in Irish coastal waters 1987–2011, using the dogwhelk (Nucella lapillus) as a biological indicator, Mar. Pollut. Bull. 100(1), 289-296.
12. X. Wang, L. Kong, J. Cheng, D. Zhao, H. Chen, R. Sun, et al., 2019. Distribution of butyltins at dredged material dumping sites around the coast of China and the potential ecological risk, Mar. Pollut. Bull. 138, 491-500.
13. A.P. Negri, L.T. Hales, C. Battershill, C. Wolff, N.S. Webster, 2004. TBT contamination identified in Antarctic marine sediments, Mar. Pollut. Bull. 48(11), 1142-1144.
14. S.J.M. Blaber, 1970. The occurrence of a penis-like outgrowth behind the right tentacle in spent females of Nucella Lapillus, J. Molluscan Stud. 39(2-3), 231-233.
15. M. Schøyen, N.W. Green, D.Ø. Hjermann, L. Tveiten, B. Beylich, S. Øxnevad, et al., 2019. Levels and trends of tributyltin (TBT) and imposex in dogwhelk (Nucella lapillus) along the Norwegian coastline from 1991 to 2017, Mar. Environ. Res. 144, 1-8.
16. C.-S. Zhao, D.-A. Fang, D.-P. Xu, 2020. Toll-like receptors (TLRs) respond to tributyltin chloride (TBT-Cl) exposure in the river pufferfish (Takifugu obscurus): Evidences for its toxic injury function, Fish Shellfish Immunol. 99, 526-534.
17. P. Li, Z.-H. Li, 2020. Environmental co-exposure to TBT and Cd caused

neurotoxicity and thyroid endocrine disruption in zebrafish, a three-generation study in a simulated environment, Environ. Pollut. 259, 113868.
18. A.S. Clare, 1998. Towards nontoxic antifouling, J. Mar. Biotech. 6, 3-6.
19. P.-Y. Qian, Y. Xu, N. Fusetani, 2009. Natural products as antifouling compounds: recent progress and future perspectives, Biofouling 26(2), 223-234.
20. R. Ramasubburayan, S. Prakash, S. Venkatesan, A. Palavesam, G. Immanuel, 2017. Environmentally benign antifouling activity and toxic properties of bioactive metabolites from mangrove Excoecaria agallocha L, Environ. Sci. Pollut. Res. 24(35), 27490-27501.
21. D. Feng, W. Wang, X. Wang, Y. Qiu, C. Ke, 2016. Low barnacle fouling on leaves of the mangrove plant Sonneratia apetala and possible anti-barnacle defense strategies, Mar. Ecol. Prog. Ser. 544, 169-182.
22. I. Sánchez-Lozano, C.J. Hernández-Guerrero, M. Muñoz-Ochoa, C. Hellio, 2019. Biomimetic Approaches for the Development of New Antifouling Solutions: Study of Incorporation of Macroalgae and Sponge Extracts for the Development of New Environmentally-Friendly Coatings, Int. J. Mol. Sci. 20(19), 4863.
23. E. Armstrong, K.G. Boyd, A. Pisacane, C.J. Peppiatt, J.G. Burgess, 2000. Marine microbial natural products in antifouling coatings, Biofouling 16(2-4), 215-224.
24. S. Nakasono, J.G. Burgess, K. Takahashi, M. Koike, C. Murayama, S. Nakamura, et al., 1993. Electrochemical prevention of marine biofouling with a carbon-chloroprene sheet, Appl. Environ. Microbiol. 59(11), 3757-3762.
25. T. Matsunaga, T.-K. Lim, 2000. Electrochemical Prevention of Biofouling, Electrochemistry 68(11), 847-852.
26. S.L. Gaw, S. Sarkar, S. Nir, Y. Schnell, D. Mandler, Z.J. Xu, et al., 2017. Electrochemical approach for effective antifouling and antimicrobial surfaces, ACS Appl. Mater. Interfaces 9(31), 26503-26509.
27. S. Cao, J. Wang, H. Chen, D. Chen, 2011. Progress of marine biofouling and antifouling technologies, Sci. Bull. 56(7), 598-612.
28. C.H. Choi, A.J. Scardino, P.G. Dylejko, L.E. Fletcher, R. Juniper, 2013. The effect of vibration frequency and amplitude on biofouling deterrence, Biofouling 29(2), 195-202.
29. J.S. McQuillan, D.J. Hopper, I. Magiopoulos, M. Arundell, R. Brown, S. Shorter, et al., 2016. Buzz off! An evaluation of ultrasonic acoustic vibration for the disruption of marine micro-organisms on sensor-housing materials, Lett. Appl. Microbiol. 63(6), 393-399.
30. D. Smith, 2012. Culture collections, Adv. Appl. Microbiol. 79, 73-118.
31. D.F. Bray, J. Bagu, P. Koegler, 1993. Comparison of hexamethyldisilazane (HMDS), Peldri II, and critical-point drying methods for scanning electron microscopy of biological specimens, Microsc. Res. Tech. 26(6), 489-495.
32. S. Nikara, E. Ahmadi, A.A. Nia, 2020. Effects of different preparation techniques on the microstructural features of biological materials for scanning electron microscopy, J. Sci. Food Agric. 2, 100036.
33. J. Chapman, C. Hellio, T. Sullivan, R. Brown, S. Russell, E. Kiterringham, et al., 2014. Bioinspired synthetic macroalgae: Examples from nature for antifouling applications, Int. Biodeterior. Biodegradation 86, 6-13.
34. L. Zhao, R. Chen, L. Lou, X. Jing, Q. Liu, J. Liu, et al., 2020. Layer-by-Layer-Assembled antifouling films with surface microtopography inspired by Laminaria

japonica, Appl. Surf. Sci. 511, 145564.
35. A.V. Bers, M. Wahl, 2004. The Influence of Natural Surface Microtopographies on Fouling, Biofouling 20(1), 43-51.
36. A. Clasen, A.B. Kesel, 2019. Microstructural surface properties of drifting seeds-a model for non-toxic antifouling solutions, Biomimetics 4(2), 37.
37. X. Liang, R. Dong, J.C. Ho, 2019. Self-assembly of colloidal spheres toward fabrication of hierarchical and periodic nanostructures for technological applications, Adv. Mater. Technol. 4(3), 1800541.
38. K.-S. Kang, 2014. Fabrication of large area nanostructures with surface modified silica spheres, Superlattices Microstruct. 67, 17-24.
39. D.R. Hines, N.P. Siwak, L.A. Mosher, R. Ghodssi. MEMS Lithography and Micromachining Techniques. In: Ghodssi R, Lin P, editors. MEMS Materials and Processes Handbook. Boston, MA: Springer US; 2011. p. 667-753.
40. C.-Y. Wu, H. Hsieh, Y.-C. Lee, 2019. Contact Photolithography at Sub-Micrometer Scale Using a Soft Photomask, Micromachines (Basel) 10(8), 547.
41. R. Menon, A. Patel, D. Gil, H.I. Smith, 2005. Maskless lithography, Mater. Today 8(2), 26-33.
42. J.T. Hastings, F. Zhang, H.I. Smith, 2003. Nanometer-level stitching in raster-scanning electron-beam lithography using spatial-phase locking, J. Vac. Sci. Technol. B Microelectron. Nanometer. Struct. Process. Meas. Phenom. 21(6), 2650-2656.
43. M.E. Walsh, F. Zhang, R. Menon, H.I. Smith. Maskless photolithography. In: Feldman M, editor. Nanolithography: Woodhead Publishing; 2014. p. 179-193.
44. E.P. Ivanova, J. Hasan, H.K. Webb, G. Gervinskas, S. Juodkazis, V.K. Truong, et al., 2013. Bactericidal activity of black silicon, Nat. Commun. 4(1), 2838.
45. X. Cheng, L. Miao, Z. Su, H. Chen, Y. Song, X. Chen, et al., 2017. Controlled fabrication of nanoscale wrinkle structure by fluorocarbon plasma for highly transparent triboelectric nanogenerator, Microsyst. Nanoeng. 3(1), 16074.
46. K. Efimenko, J. Finlay, M.E. Callow, J.A. Callow, J. Genzer, 2009. Development and testing of hierarchically wrinkled coatings for marine antifouling, ACS Appl. Mater. Interfaces 1, 1031–1040.
47. P. Kim, Y. Hu, J. Alvarenga, M. Kolle, Z. Suo, J. Aizenberg, 2013. Rational Design of Mechano-Responsive Optical Materials by Fine Tuning the Evolution of Strain-Dependent Wrinkling Patterns, Adv. Opt. Mater. 1(5), 381-388.
48. S. Lee, E. Byeon, S. Jung, D.-G. Kim, 2018. Heterogeneity of hard skin layer in wrinkled PDMS surface fabricated by Ar ion-beam irradiation, Sci. Rep. 8(1), 14063.
49. A.E. Özçam, K. Efimenko, J. Genzer, 2014. Effect of ultraviolet/ozone treatment on the surface and bulk properties of poly(dimethyl siloxane) and poly(vinylmethyl siloxane) networks, Polymer 55(14), 3107-3119.
50. U. Gill, T. Sutherland, S. Himbert, Y. Zhu, M.C. Rheinstädter, E.D. Cranston, et al., 2017. Beyond buckling: humidity-independent measurement of the mechanical properties of green nanobiocomposite films, Nanoscale 9(23), 7781-7790.
51. S. Zeng, R. Li, S.G. Freire, V.M.M. Garbellotto, E.Y. Huang, A.T. Smith, et al., 2017. Moisture-responsive wrinkling surfaces with tunable dynamics, Adv. Mater. 29(24), 1700828.
52. H. Izawa, Y. Miyazaki, T. Yonemura, N. Ito, Y. Okamoto, S. Ifuku, et al., 2019. Polysaccharide-based wrinkled surfaces induced by polyion complex skin layers upon drying, Polym. J. 51(7), 675-683.
53. H. Hou, J. Yin, X. Jiang, 2016. Reversible Diels–Alder reaction to control

wrinkle patterns: from dynamic chemistry to dynamic patterns, Adv. Mater. 28(41), 9126-9132.
54. H. Hu, V.S. Siu, S.M. Gifford, S. Kim, M. Lu, P. Meyer, et al., 2017. Bio-inspired silicon nanospikes fabricated by metal-assisted chemical etching for antibacterial surfaces, Appl. Phys. Lett. 111(25), 253701.
55. J. Fu, H. Zhang, Z. Guo, D. Feng, V. Thiyagarajan, H. Yao, 2018. Combat biofouling with microscopic ridge-like surface morphology: a bioinspired study, J. R. Soc. Interface 15(140), 20170823.
56. G. Zhang, X.W. Lou, 2013. Controlled growth of NiCo2O4 nanorods and ultrathin nanosheets on carbon nanofibers for high-performance supercapacitors, Sci. Rep. 3(1), 1470.
57. G. Zhang, X.W. Lou, 2013. General solution growth of mesoporous NiCo2O4 nanosheets on various conductive substrates as high-performance electrodes for supercapacitors, Adv. Mater. 25(7), 976-979.
58. R. Piola, M. Leary, R. Santander, J. Shimeta, 2021. Antifouling performance of copper-containing fused filament fabrication (FFF) 3-D printing polymer filaments for marine applications, Biofouling 37(2), 206-221.
59. A. Vyatskikh, S. Delalande, A. Kudo, X. Zhang, C.M. Portela, J.R. Greer, 2018. Additive manufacturing of 3D nano-architected metals, Nat. Commun. 9(1), 593.
60. R. Jafari, C. Cloutier, A. Allahdini, G. Momen, 2019. Recent progress and challenges with 3D printing of patterned hydrophobic and superhydrophobic surfaces, Int. J. Adv. Manuf. Technol. 103(1), 1225-1238.
61. R.P. Singh, M.K. Shukla, A. Mishra, C.R.K. Reddy, B. Jha, 2013. Bacterial extracellular polymeric substances and their effect on settlement of zoospore of Ulva fasciata, Colloids Surf. B 103, 223-230.
62. J. Tan, J. Xu, D. Wang, J. Yang, S. Zhou, 2020. Seawater-responsive SiO2 nanoparticles for in situ generation of zwitterionic polydimethylsiloxane antifouling coatings with underwater superoleophobicity, J. Mater. Chem. A 8(45), 24086-24097.
63. H.W. Ducklow. Bacterioplankton. In: Steele JH, editor. Encyclopedia of Ocean Sciences. Oxford: Academic Press; 2001. p. 269-275.
64. S. Dobretsov, Abed, R.M., Sharp, K., Skalli, O., Boykins, L.G. and Coons, L. Microscopy of biofilms. In: S. Dobretsov JCTaDNW, editor. Biofouling Methods. Biofouling Methods2014. p. 1-43.
65. S.W. Hell, M. Dyba, S. Jakobs, 2004. Concepts for nanoscale resolution in fluorescence microscopy, Curr. Opin. Neurobiol. 14(5), 599-609.
66. M. Heydt, M.E. Pettitt, X. Cao, M.E. Callow, J.A. Callow, M. Grunze, et al., 2012. Settlement Behavior of Zoospores of Ulva linza During Surface Selection Studied by Digital Holographic Microscopy, Biointerphases 7(1), 33.
67. C.A. Schneider, W.S. Rasband, K.W. Eliceiri, 2012. NIH Image to ImageJ: 25 years of image analysis, Nat. Methods 9(7), 671-675.
68. P.P. Pednekar, S.C. Godiyal, K.R. Jadhav, V.J. Kadam. Mesoporous silica nanoparticles: a promising multifunctional drug delivery system. In: Ficai A, Grumezescu AM, editors. Nanostructures for Cancer Therapy. Amsterdam: Elsevier; 2017. p. 593-621.
69. M. Klinger-Strobel, H. Suesse, D. Fischer, M.W. Pletz, O. Makarewicz, 2016. A Novel Computerized Cell Count Algorithm for Biofilm Analysis, PLoS One 11(5), e0154937.
70. R. Bakke, R. Kommedal, S. Kalvenes, 2001. Quantification of biofilm

accumulation by an optical approach, J. Microbiol. Methods 44(1), 13-26.
71. K.D. Esmeryan, C.E. Castano, T.A. Chaushev, R. Mohammadi, T.G. Vladkova, 2019. Silver-doped superhydrophobic carbon soot coatings with enhanced wear resistance and anti-microbial performance, Colloids Surf. A Physicochem. Eng. Asp. 582, 123880.
72. A.L.J. Olsson, M.R. Mitzel, N. Tufenkji, 2015. QCM-D for non-destructive real-time assessment of Pseudomonas aeruginosa biofilm attachment to the substratum during biofilm growth, Colloids Surf. B: Biointerfaces 136, 928-934.
73. T.E. Alexander, L.D. Lozeau, T.A. Camesano, 2019. QCM-D characterization of time-dependence of bacterial adhesion, The Cell Surface 5, 100024.
74. K.D. Esmeryan, C.E. Castano, M. Abolghasemibizaki, R. Mohammadi, 2017. An artful method for in-situ assessment of the anti-biofouling potential of various functional coatings using a quartz crystal microbalance, Sens. Actuators B Chem. 243, 910-918.
75. P.J. Molino, O.M. Hodson, J.F. Quinn, R. Wetherbee, 2008. The quartz crystal microbalance: a new tool for the investigation of the bioadhesion of diatoms to surfaces of differing surface energies, Langmuir 24(13), 6730-6737.
76. G. Sauerbrey, 1959. The use of quartz oscillators for weighing thin layers and for microweighing, Z. Phys. 155, 206-222.
77. R. Van Der Westen, P.K. Sharma, H. De Raedt, I. Vermue, H.C. Van Der Mei, H.J. Busscher, 2017. Elastic and viscous bond components in the adhesion of colloidal particles and fibrillated streptococci to QCM-D crystal surfaces with different hydrophobicities using Kelvin-Voigt and Maxwell models, Phys. Chem. Chem. Phys. 19(37), 25391-25400.
78. P.J. Molino, O.M. Hodson, J.F. Quinn, R. Wetherbee, 2006. utilizing QCM-D to characterize the adhesive mucilage secreted by two marine diatom species in-situ and in real-time, Biomacromolecules 7(11), 3276-3282.
79. C. Sousa, C. Compère, C. Dreanno, M.-P. Crassous, F. Gas, B. Baus, et al., 2014. Direct and fast detection of Alexandrium minutum algae by using high frequency microbalance, J. Microbiol. Methods 104, 49-54.
80. A.J. Scardino, E. Harvey, R.D. Nys, 2006. Testing attachment point theory: diatom attachment on microtextured polyimide biomimics, Biofouling 22(1), 55-60.
81. A.V. Bers, G.S. Prendergast, C.M. Zürn, L. Hansson, R.M. Head, J.C. Thomason, 2006. A comparative study of the anti-settlement properties of mytilid shells, Biol. Lett. 2(1), 88-91.
82. M.L. Carman, T.G. Estes, A.W. Feinberg, J.F. Schumacher, W. Wilkerson, L.H. Wilson, et al., 2006. Engineered antifouling microtopographies – correlating wettability with cell attachment, Biofouling 22(1), 11-21.
83. A.M. Brzozowska, F.J. Parra-Velandia, R. Quintana, Z. Xiaoying, S.S.C. Lee, L. Chin-Sing, et al., 2014. Biomimicking Micropatterned Surfaces and Their Effect on Marine Biofouling, Langmuir 30(30), 9165-9175.
84. T. Sullivan, F. Regan, 2011. The characterization, replication and testing of dermal denticles of Scyliorhinus canicula for physical mechanisms of biofouling prevention, Bioinspir. Biomim. 6(4), 046001.
85. J.L. Wortham, S. Pascual, 2017. Grooming behaviors and gill fouling in the commercially important blue crab (Callinectes sapidus) and stone crab (Menippe mercenaria), Nauplius 25, e2017028.
86. K.N. Mouritsen, T. Jensen, 2006. The effect of Sacculina carcini infections on

the fouling, burying behaviour and condition of the shore crab, Carcinus maenas, Mar. Biol. Res. 2(4), 270-275.
87. P. O'Neill, A. Barrett, T. Sullivan, F. Regan, D. Brabazon, 2016. Rapid prototyped biomimetic antifouling surfaces for marine applications, Mater. Today 3(2), 527-532.
88. M.E. Callow, A.R. Jennings, A.B. Brennan, C.E. Seegert, A. Gibson, L. Wilson, et al., 2002. Microtopographic Cues for Settlement of Zoospores of the Green Fouling Alga Enteromorpha, Biofouling 18(3), 229-236.
89. J. Verran, R.D. Boyd, 2001. The relationship between substratum surface roughness and microbiological and organic soiling: A review, Biofouling 17(1), 59-71.
90. J.F. Schumacher, M.L. Carman, T.G. Estes, A.W. Feinberg, L.H. Wilson, M.E. Callow, et al., 2007. Engineered antifouling microtopographies – effect of feature size, geometry, and roughness on settlement of zoospores of the green alga Ulva, Biofouling 23(1), 55-62.
91. R.N. Wenzel, 1936. Resistance of solid surfaces to wetting by water, Ind. Eng. Chem. Res. 28(8), 988-994.
92. C.J. Long, J.F. Schumacher, P.A.C. Robinson, J.A. Finlay, M.E. Callow, J.A. Callow, et al., 2010. A model that predicts the attachment behavior of Ulva linza zoospores on surface topography, Biofouling 26(4), 411-419.
93. J.F. Schumacher, C.J. Long, M.E. Callow, J.A. Finlay, J.A. Callow, A.B. Brennan, 2008. Engineered Nanoforce Gradients for Inhibition of Settlement (Attachment) of Swimming Algal Spores, Langmuir 24(9), 4931-4937.
94. N.J. Shirtcliffe, G. McHale, S. Atherton, M.I. Newton, 2010. An introduction to superhydrophobicity, Adv. Colloid Interface Sci. 161(1), 124-138.
95. P. Qian, D. Rittschof, B. Sreedhar, 2000. Macrofouling in unidirectional flow: miniature pipes as experimental models for studying the interaction of flow and surface characteristics on the attachment of barnacle, bryozoan and polychaete larvae, Mar. Ecol. Prog. Ser. 207, 109-121.
96. G. Thorson, 1964. Light as an ecological factor in the dispersal and settlement of larvae of marine bottom invertebrates, Ophelia 1(1), 167-208.
97. S. Howes, C.M. Herbinger, P. Darnell, B. Vercaemer, 2007. Spatial and temporal patterns of recruitment of the tunicate Ciona intestinalis on a mussel farm in Nova Scotia, Canada, J. Exp. Mar. Biol. Ecol. 342(1), 85-92.
98. M. Lehaitre, Delauney, L., Compere, C. Biofouling and underwater measurements. Commission IO, editor. Paris, France: United Nations Educational, Scientific and Cultural Organization; 2008.
99. A.J. Scardino, J. Guenther, R.d. Nys, 2008. Attachment point theory revisited: the fouling response to a microtextured matrix, Biofouling 24(1), 45-53.
100. N. Ahmed, T. Murosaki, A. Kakugo, T. Kurokawa, J.P. Gong, Y. Nogata, 2011. Long-term in situ observation of barnacle growth on soft substrates with different elasticity and wettability, Soft Matter 7(16), 7281.
101. R. Gabilondo, H. Graham, G.S. Caldwell, A.S. Clare, 2013. Laboratory culture and evaluation of the tubeworm Ficopomatus enigmaticus for biofouling studies, Biofouling 29(7), 869-878.
102. A.E. Vellwock. Biofouling studies dataset. 2 ed. Mendeley Data2019.
103. P.J. Huber, 1964. Robust Estimation of a Location Parameter, Ann. Math. Statist. 35(1), 73-101.
104. J.F. Schumacher, N. Aldred, M.E. Callow, J.A. Finlay, J.A. Callow, A.S. Clare,

et al., 2007. Species-specific engineered antifouling topographies: correlations between the settlement of algal zoospores and barnacle cyprids, Biofouling 23(5), 307-317.
105. M.J. Vucko, A.J. Poole, C. Carl, B.A. Sexton, F.L. Glenn, S. Whalan, et al., 2014. Using textured PDMS to prevent settlement and enhance release of marine fouling organisms, Biofouling 30(1), 1-16.
106. R. Mincheva, A. Beigbeder, M.E. Pettitt, M.E. Callow, J.A. Callow, P. Dubois, 2016. Metal-free anti-biofouling coatings: the preparation of silicone-based nanostructured coatings via purely organic catalysis, Nanocomposites 2(2), 51-57.
107. Z. Wang, A.A. Volinsky, N.D. Gallant, 2015. Nanoindentation study of polydimethylsiloxane elastic modulus using Berkovich and flat punch tips, J. Appl. Polym. Sci. 132(5), 41384.
108. W.D. Callister. Fundamentals of materials science and engineering : an integrated approach. 2nd ed. Hoboken, N.J.: Wiley; 2005.
109. M. Davidson, Steve Bastian, and Finley Markley., 1992. Measurement of the Elastic Modulus of Kapton Perpendicular to the Plane of the Film at Room and Cryogenic Temperatures, Supercollider 4, 1039-1045.
110. E. Baur, T.A. Osswald, N. Rudolph. Material Properties. In: Baur E, Osswald TA, Rudolph N, editors. Plastics Handbook: Hanser; 2019. p. 625-663.
111. G. Wypych. PVC Properties. In: Wypych G, editor. PVC Formulary. 2nd ed. San Diego: ChemTec Publishing; 2015. p. 5-44.
112. L.W. McKeen. Thermoplastic Elastomers. In: McKeen LW, editor. The Effect of Temperature and other Factors on Plastics and Elastomers. 3rd ed. Oxford, UK: William Andrew Publishing; 2014. p. 371-398.
113. E. Buckingham, 1914. On Physically Similar Systems; Illustrations of the Use of Dimensional Equations, Phys. Rev. 4(4), 345-376.
114. A. Bagheri, H. Midi, 2009. Robust Estimations as a Remedy for Multicollinearity Caused by Multiple High Leverage Points, J. Math. Stat. 5(4), 311-321.
115. S. Lambert-Lacroix, L. Zwald, 2011. Robust regression through the Huber's criterion and adaptive lasso penalty, Electronic Journal of Statistics 5(0), 1015-1053.
116. H.-C. Flemming. Microbial Biofouling: Unsolved Problems, Insufficient Approaches, and Possible Solutions. In: Flemming H-C, Wingender J, Szewzyk U, editors. Biofilm Highlights. 5. Berlin, Heidelberg: Springer Berlin Heidelberg; 2011. p. 81-109.
117. A.K. Mondal, K. Bansal, 2015. A brief history and future aspects in automatic cleaning systems for solar photovoltaic panels, Adv. Robot. 29(8), 515-524.
118. T.-L. Chen, Y.-P. Lin, C.-H. Chien, Y.-C. Chen, Y.-J. Yang, W.-L. Wang, et al., 2021. Fabrication of Frog-Skin-Inspired Slippery Antibiofouling Coatings Through Degradable Block Copolymer Wrinkling, Adv. Funct. Mater. 31(42), 2104173.
119. C. Feng, T. Gou, J. Li, Y. Cai, P. He, J. Huang, et al., 2019. A highly transparent polymer coating on the glass with broadband antireflection, antifogging and antifouling properties, Mater. Res. Express 6(7), 075319.
120. R. Chen, Y. Zhang, Q. Xie, Z. Chen, C. Ma, G. Zhang, 2021. Transparent Polymer-Ceramic Hybrid Antifouling Coating with Superior Mechanical Properties, Adv. Funct. Mater. 31(19), 2011145.
121. J. Wang, S. Lee, A.R. Bielinski, K.A. Meyer, A. Dhyani, A.M. Ortiz-Ortiz, et al., 2020. Rational Design of Transparent Nanowire Architectures with Tunable

Geometries for Preventing Marine Fouling, Adv. Mater. Interfaces 7(17), 2000672.
122. S. Sunny, G. Cheng, D. Daniel, P. Lo, S. Ochoa, C. Howell, et al., 2016. Transparent antifouling material for improved operative field visibility in endoscopy, Proc. Natl. Acad. Sci. U.S.A. 113(42), 11676.
123. W. Wang, Y. Lu, H. Zhu, Z. Cao, 2017. Superdurable Coating Fabricated from a Double-Sided Tape with Long Term "Zero" Bacterial Adhesion, Adv. Mater. 29(34), 1606506.
124. C. Feng, Z. Zhang, J. Li, Y. Qu, D. Xing, X. Gao, et al., 2019. A Bioinspired, Highly Transparent Surface with Dry-Style Antifogging, Antifrosting, Antifouling, and Moisture Self-Cleaning Properties, Macromol. Rapid Commun. 40(6), 1800708.
125. M. Liu, S. Li, H. Wang, R. Jiang, X. Zhou, 2021. Research progress of environmentally friendly marine antifouling coatings, Polym. Chem. 12(26), 3702-3720.
126. S.J.M. Blaber, 1970. The Ocurrance of a Penis-like Outgrowth Behind the Right Tentacle in Spent Females of Nucella Lapillus, J. Molluscan Stud. 39(2-3), 231-233.
127. A.E. Vellwock, J. Fu, Y. Meng, V. Thiyagarajan, H. Yao, 2019. A data-driven approach to predicting the attachment density of biofouling organisms, Biofouling, 1-8.
128. A.E. Vellwock, H. Yao, 2021. Biomimetic and bioinspired surface topographies as a green strategy for combating biofouling: a review, Bioinspir. Biomim. 16(4), 041003.
129. Y. Lee, Y.-W. Chung, J. Park, K. Park, Y. Seo, S.-N. Hong, et al., 2020. Lubricant-infused directly engraved nano-microstructures for mechanically durable endoscope lens with anti-biofouling and anti-fogging properties, Sci. Rep. 10(1), 17454.
130. S. Heydarian, R. Jafari, G. Momen, 2021. Recent progress in the anti-icing performance of slippery liquid-infused surfaces, Prog. Org. Coat. 151, 106096.
131. X.C. Zhao, R.W. Yee, E. Norcom, H. Burgess, A.S. Avanesov, J.P. Barrish, et al., 2006. The Zebrafish Cornea: Structure and Development, Investig. Ophthalmol. Vis. Sci. 47(10), 4341-4348.
132. S.P. Collin, H.B. Collin, 2000. A Comparative SEM Study of the Vertebrate Corneal Epithelium, Cornea 19(2), 218-230.
133. S.P. Collin, H.B. Collin, 2006. The corneal epithelial surface in the eyes of vertebrates: Environmental and evolutionary influences on structure and function, J. Morphol. 267(3), 273-291.
134. S.P. Collin, N.J. Marshall, H.B. Collin, S.P. Collin, 2000. The corneal surface of aquatic vertebrates: microstructures with optical and nutritional function?, Philos. Trans. R. Soc. Lond., B, Biol. Sci. 355(1401), 1171-1176.
135. R.R. Pfister, N.L. Burstein, 1977. The normal and abnormal human corneal epithelial surface: a scanning electron microscope study, Investig. Ophthalmol. Vis. Sci. 16(7), 614-622.
136. P.-y. Lam, S. Mangos, J.M. Green, J. Reiser, A. Huttenlocher, 2015. In Vivo Imaging and Characterization of Actin Microridges, PLoS One 10(1), e0115639.
137. C. Talbot, T.M. Jordan, N.W. Roberts, S.P. Collin, N.J. Marshall, S.E. Temple, 2012. Corneal microprojections in coleoid cephalopods, J. Comp. Physiol. A 198(12), 849-856.
138. D. Nečas, P. Klapetek, 2012. Gwyddion: an open-source software for SPM data

analysis, Open Phys. 10(1), 181-188.
139. J. Bacharouche, H. Haidara, P. Kunemann, M.-F. Vallat, V. Roucoules, 2013. Singularities in Hydrophobic Recovery of Plasma Treated Polydimethylsiloxane Surfaces Under Non-Contaminant Atmosphere, Sens. Actuator A Phys. 197, 25-29.
140. R.F. Collery, K.N. Veth, A.M. Dubis, J. Carroll, B.A. Link, 2014. Rapid, Accurate, and Non-Invasive Measurement of Zebrafish Axial Length and Other Eye Dimensions Using SD-OCT Allows Longitudinal Analysis of Myopia and Emmetropization, PLoS One 9(10), e110699.
141. G.M. Hale, M.R. Querry, 1973. Optical Constants of Water in the 200-nm to 200-μm Wavelength Region, Appl. Opt. 12(3), 555-563.
142. L.B. Freund, S. Suresh. Thin Film Materials: Stress, Defect Formation and Surface Evolution. Cambridge: Cambridge University Press; 2004.
143. M. Nania, O.K. Matar, J.T. Cabral, 2015. Frontal vitrification of PDMS using air plasma and consequences for surface wrinkling, Soft Matter 11(15), 3067-3075.
144. R.C. Millard, G. Seaver, 1990. An index of refraction algorithm for seawater over temperature, pressure, salinity, density, and wavelength, Deep Sea Res. Part I Oceanogr. Res. Pap. 37(12), 1909-1926.
145. A. Börzsönyi, Z. Heiner, M.P. Kalashnikov, A.P. Kovács, K. Osvay, 2008. Dispersion measurement of inert gases and gas mixtures at 800 nm, Appl. Opt. 47(27), 4856-4863.
146. C.-X. Shuai, Y. He, P. Su, Q. Huang, D. Pan, Q. Xu, et al., 2020. Integration of PEGylated Polyaniline Nanocoatings with Multiple Plastic Substrates Generates Comparable Antifouling Performance, Langmuir 36(31), 9114-9123.
147. S.I. Faria, L.C. Gomes, R. Teixeira-Santos, J. Morais, V. Vasconcelos, F.J.M. Mergulhão, 2021. Developing New Marine Antifouling Surfaces: Learning from Single-Strain Laboratory Tests, Coatings 11(1), 90.
148. Lim, K. Everuss, A. Goodman, K. Benkendorff, 2007. Comparison of surface microfouling and bacterial attachment on the egg capsules of two molluscan species representing Cephalopoda and Neogastropoda, Aquat. Microb. Ecol. 47, 275-287.
149. M.M. Slusher, Q.N. Myrvik, J.C. Lewis, A.G. Gristina, 1987. Extended-Wear Lenses, Biofilm, and Bacterial Adhesion, Arch. Ophthalmol. 105(1), 110-115.
150. F. Stapleton, N. Carnt, 2012. Contact lens-related microbial keratitis: how have epidemiology and genetics helped us with pathogenesis and prophylaxis, Eye 26(2), 185-193.
151. P.E. King-Smith, S.H. Kimball, J.J. Nichols, 2014. Tear film interferometry and corneal surface roughness, Investig. Ophthalmol. Vis. Sci. 55(4), 2614-2618.
152. H. Jin, W. Bing, L. Tian, P. Wang, J. Zhao, 2019. Combined Effects of Color and Elastic Modulus on Antifouling Performance: A Study of Graphene Oxide/Silicone Rubber Composite Membranes, Materials 12(16), 2608.
153. T. Kim, S. Kwon, J. Lee, J.S. Lee, S. Kang, 2022. A metallic anti-biofouling surface with a hierarchical topography containing nanostructures on curved micro-riblets, Microsyst. Nanoeng. 8(1), 6.
154. A.B. Tesler, P. Kim, S. Kolle, C. Howell, O. Ahanotu, J. Aizenberg, 2015. Extremely durable biofouling-resistant metallic surfaces based on electrodeposited nanoporous tungstite films on steel, Nat. Commun. 6, 8649.
155. D.Q. Feng, J. He, S.Y. Chen, P. Su, C.H. Ke, W. Wang, 2018. The Plant Alkaloid Camptothecin as a Novel Antifouling Compound for Marine Paints: Laboratory Bioassays and Field Trials, Mar. Biotechnol. 20(5), 623-638.

156. C.M. Magin, S.P. Cooper, A.B. Brennan, 2010. Non-toxic antifouling strategies, Mater. Today 13(4), 36-44.
157. Z. Lu, Z. Chen, Y. Guo, Y. Ju, Y. Liu, R. Feng, et al., 2018. Flexible Hydrophobic Antifouling Coating with Oriented Nanotopography and Nonleaking Capsaicin, ACS Appl. Mater. Interfaces. 10(11), 9718-9726.
158. H. Hao, S. Chen, Z. Wu, P. Su, C. Ke, D. Feng, 2022. The degradation and environmental risk of camptothecin, a promising marine antifoulant, Sci. Total Environ. 821, 153384.
159. R.P. Singh, M.K. Shukla, A. Mishra, C.R.K. Reddy, B. Jha, 2013. Bacterial extracellular polymeric substances and their effect on settlement of zoospore of Ulva fasciata, Colloids Surf. B Biointerfaces 103, 223-230.
160. H. Jin, L. Tian, W. Bing, J. Zhao, L. Ren, 2022. Bioinspired marine antifouling coatings: Status, prospects, and future, Prog. Mater. Sci. 124, 100889.
161. P.-C. Lin, S. Yang, 2007. Spontaneous formation of one-dimensional ripples in transit to highly ordered two-dimensional herringbone structures through sequential and unequal biaxial mechanical stretching, Appl. Phys. Lett. 90(24), 241903.
162. S. Béfahy, P. Lipnik, T. Pardoen, C. Nascimento, B. Patris, P. Bertrand, et al., 2010. Thickness and Elastic Modulus of Plasma Treated PDMS Silica-like Surface Layer, Langmuir 26(5), 3372-3375.
163. F.A. Bayley, J.L. Liao, P.N. Stavrinou, A. Chiche, J.T. Cabral, 2014. Wavefront kinetics of plasma oxidation of polydimethylsiloxane: limits for sub-μm wrinkling, Soft Matter 10(8), 1155-1166.
164. B.A. Glatz, A. Fery, 2019. The influence of plasma treatment on the elasticity of the in situ oxidized gradient layer in PDMS: towards crack-free wrinkling, Soft Matter 15(1), 65-72.